2018

Single Molecule Imaging Reveals Tau Structure And Function On The Microtubule Surface

Jamie Stern
University of Vermont

SINGLE MOLECULE IMAGING REVEALS TAU STRUCTURE AND FUNCTION ON THE MICROTUBULE SURFACE

A Dissertation Presented

by

Jamie Stern

to

The Faculty of the Graduate College

of

The University of Vermont

In Partial Fulfillment of the Requirements
for the Degree of Doctor of Philosophy
Specializing in Cellular, Molecular and Biomedical Sciences

May, 2018

Defense Date: March 21, 2018
Dissertation Examination Committee:

Christopher L. Berger, Ph.D., Advisor
Bryan Ballif, Ph.D., Chairperson
Anthony Morielli, Ph.D.
Jason Stumpff, Ph.D.
Cynthia J. Forehand, Ph.D., Dean of the Graduate College

ABSTRACT

Neurons are among the most highly polarized cells in the human body. This polarization allows the neuron to participate in the transfer of chemical and electrical signals which are crucial to the survival of the organism. As part of polarization, each neuron develops a dendritic arbor and an axon. To ensure the survival of the cell, materials synthesized in the cell body must be trafficked through the axon for delivery throughout ultimately ending at the synaptic termini. The bulk of this cargo transport is microtubule-based fast axonal transport which is molecular motor mediated and tightly regulated though many pathways. Motor based transport is established early in development and maintained for the life of the cell. The kinesin motor protein family plays an integral role in fast axonal transport and the regulation of these motors is essential to proper cargo delivery. Regulation occurs through auto-inhibition, motor interactions with microtubule associated proteins (MAPs) and complex signaling pathways which control the post-translational modification of MAPs, the microtubule track and the motors.

The disruption of cargo transport is linked to neurodegeneration and disease state development. Of particular interest in this process is the MAP Tau which has been implicated in a number of neurodegenerative diseases including Alzheimer's Disease. Tau is expressed at all stages of neural development and has been shown to participate in signaling cascades, modulate microtubule dynamics and preferentially inhibit kinesin-1 motility. Though Tau is involved in these processes, the non-disease state regulation of this MAP and it's inhibition of kinesin-1 is not well understood. Tau has been shown to bind the microtubule surface in a static-diffusive state equilibrium which differs with isoform and lattice. Previous work demonstrates that the static state is more inhibitory to kinesin-1 than the diffusive state. These different binding behaviors with their different effects on kinesin-1 motility, suggest that cellular regulation of Tau's static-diffusive binding equilibrium may control inhibition of kinesin-1 and that structural changes may underlie Tau binding to the microtubule surface. Cellular regulation of Tau's structure and therefore its behavior on the microtubule surface points to a means by which Tau is regulated in the non-disease state. Additionally, this would highlight how early changes lead to disease state development.

Using a combination of molecular biology, biochemical techniques and imaging strategies including Total Internal Reflection Fluorescence, single molecule Fluorescence Resonance Energy Transfer (smFRET) and Alternating Laser Excitation, we show that Tau's static-diffusive state equilibrium is regulated by non-disease state phosphorylation at tyrosine 18. Phospho-mimetics are shifted towards diffusive binding and have decreased affinity for the microtubule surface which in turn reduces inhibition of kinesin-1 motility. These results further demonstrate that Tau undergoes long range structural change while bound to the microtubule surface. We performed smFRET assays and found that Tau binds the microtubule surface in distinct conformations which underlie static and diffusive binding. This work ties the regulation of Tau's structure and binding behavior to its function and paves the way for our understanding of how cellular regulation acts on multiple levels to fine tune axonal transport.

CITATIONS

Material from this dissertation has been published in the following form:

Stern, J.L., Lessard, D.V., Hoeprich, G.J., Morfini, G.A., and Berger, C.L.. (2017). Phospho-regulation of tau modulates inhibition of kinesin-1 motility. Mol. Biol. Cell.

ACKNOWLEDGEMENTS

First and foremost I would like to thank my family Jerome, Barbara and Brittany for their support and understanding throughout this process. Without them, this would not have been possible. I would like to thank my mentor, Dr. Christopher Berger for his guidance and support over the last six years. His training and advice have helped me become the scientist I am. It has been a privilege to work with the members of the Berger lab past and present, Dr. Gregory Hoeprich, Dominic Lessard and Alisa Cario. I would especially like to thank Lynn Chrin for her help. Dr. Stephen Everse has been a tremendous source of support. My committee members Dr. Bryan Ballif, Dr. Anthony Morielli, Dr. Jason Stumpff have offered invaluable advice and guidance throughout my time in graduate school. The Warshaw lab, especially Dr. David Warshaw and Guy Kennedy, have been instrumental in my microscope training. My CMB program classmates especially Dr. Joyce Thompson, Victoria DeVault and Haein Kim have been a second family. The Stumpff lab members especially, Dr. Heidi Malaby and Cindy Fonseca have always been supportive. Lastly, I would like to thank the members of the MPBP department and the CMB/NGP administrators for their help and support along the way.

TABLE OF CONTENTS

Page

LIST OF TABLES

Table Page

LIST OF FIGURES

Figure Page

CHAPTER 1: LITERATURE REVIEW

1.1 Neuronal Development and Degeneration

1.1.1 The Neuron Theory

The Nobel Prize in Physiology and Medicine was awarded to Camillo Golgi and Santiago Ramón y Cajal in 1906 (Golgi, 1906; Ramón y Cajal, 1906). In his acceptance speech, Ramón y Cajal described data generated using staining methods developed by Golgi in support of the idea that discrete cellular units called neurons compose the nervous system (Ramón y Cajal, 1906).

During the early years of the development of neurology, work by Ramón y Cajal, Van Gehuchten and others revealed that neurons are electrically excitable cells that develop a uniquely polarized structure consisting of a cell body from which multiple dendrites branch and a single axon extends (Figure 1.1) (Ramón y Cajal, 1906; Pasik *et al.*, 1999; Ling *et al.*, 2012; Levitan and Kaczmarek, 2015). The interaction of a dendrite with an axon terminal creates a cell-cell junction known as the synapse (Levitan and Kaczmarek, 2015). At the synapse, electrical impulses propagated down the axon are either directly transmitted to the other neuron or converted to chemical signals which bridge the gap between the axon and the dendrite (Levitan and Kaczmarek, 2015).

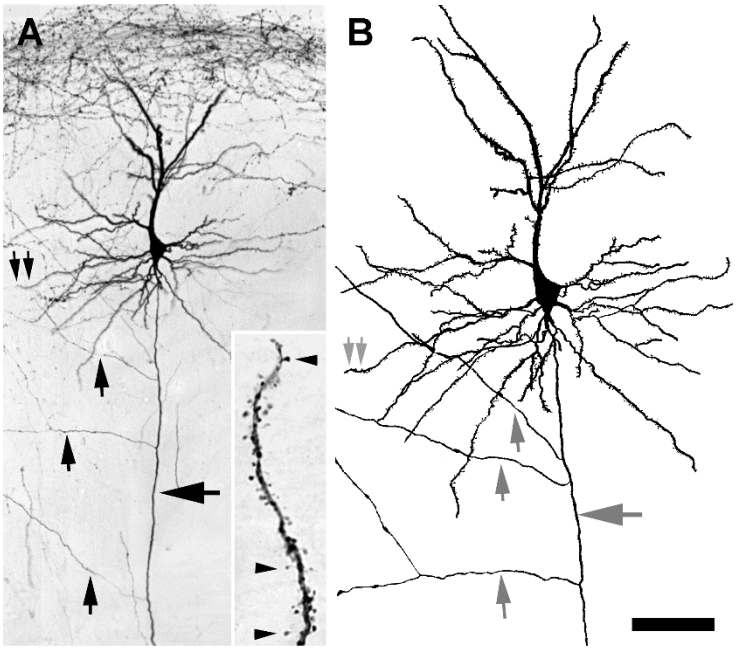

Figure 1.1: Pyramidal neuron

A) The axon of the pyramidal neuron (horizontal arrow) descends to the white matter, but also sends branches (vertical arrows) horizontally. Double arrows indicate the region shown in the inset, rotated 90° clockwise, that illustrates spiny appendages (arrowheads) distributed along a segment of a labeled dendrite. **B**) Camera lucida drawing of the labeled neuron shown in **A** to illustrate the entire dendritic arbor of the neuron. Scale bar: 75 µm in **A**, 50 µm in **B**, and 10 µm for the inset in **A**. Figure and legend adapted from Ling *et al.,* (2012) in accordance with the Creative Commons Attribution license.

1.1.2 Neural Development

The nervous system begins to develop within the first gestational month (Stiles and Jernigan, 2010). In humans on embryonic day 13 (E13), complex signaling pathways facilitate gastrulation – the development of three layers of stem cells including the neuralectodermal (neural progenitor) cells (Stiles and Jernigan, 2010). These cells will eventually give rise to all the components of the brain and central nervous system. Neural progenitor cells undergo successive rounds of symmetric cell division between E25 and E42 to provide a pool from which neurons can develop (Stiles and Jernigan, 2010). After E42 symmetric cell division gives way to asymmetric division which produces one progenitor cell and one neuron (Wodarz and Huttner, 2003).

1.1.3 Axonal Development

Each neuron must develop a dendritic arbor and an axon. Axonal development is dependent on growth cone formation (Kalil and Dent, 2014). The growth cone is a mobile leading edge which upon development, grows outwards from the cell in response to guidance cues such as nerve growth factor (NGF), brain derived neurotrophic factor (BDNF), netrins, ephrins and semaphorins (Gibney and Zheng, 2003; Kalil and Dent, 2014). Netrins ephrins and semaphorins can act as both attractive and repulsive factors depending on the receptor present (Moore *et al.*, 2007; Kalil and Dent, 2014). The combination of attractive and repulsive cues shapes the trajectory of the growth cone, regulates axon branching and prevents axon crossing (Kalil and Dent, 2014). The mobility of the growth cone is due to the organization of a complex cytoskeletal structure

consisting of both actin and microtubule based components (Kalil and Dent, 2014). The growth cone can be divided into a peripheral region of dynamic actin cytoskeleton which produces lamellipodia- and filopodia-like structures and a central region with a dense microtubule cytoskeleton (Kalil and Dent, 2014). Both actin and microtubules are polymers which grow and shrink dynamically (Kalil and Dent, 2014). Actin is a globular protein that forms filaments through the binding and hydrolysis of ATP while microtubules are comprised of globular tubulin heterodimers that form tubules through the binding and hydrolysis of GTP (Korn *et al.*, 1987; Desai and Mitchison, 1997; Kalil and Dent, 2014).

The microtubules in the central region are essential for stabilizing the axon as it develops (Kalil and Dent, 2014). These microtubules are organized with their plus ends oriented away from the neuronal cell body (Kalil and Dent, 2014). This orientation allows the microtubule bundles to act as highways for the retrograde/anterograde transport of cargo critical to the development and maintenance of the axon (Kalil and Dent, 2014). Cargo transport is largely a molecular motor based process which is tightly regulated by the cell (Stenoien and Brady, 1999) .

Neurons establish polarity once they exit the cell cycle (Barnes and Polleux, 2009). In some cases, polarity is the result of the apico-basal arrangement of the cell as is the case for mouse retinal ganglion cells (Figure 1.2) (Barnes and Polleux, 2009). Upon cell cycle exit, the cell body migrates from the apical to the basal membrane forming a trailing and leading process (Polleux and Snider, 2010). Dendrites develop from the apical process while the axon is formed from the basal process (Figure 1.2) (Barnes and Polleux, 2009). Not all neuronal cell types immediately form a single trailing and leading

edge. Mouse pyramidal neurons for example, through the action of cyclin dependent kinase 5 (Cdk5), produce many processes or neurites before a trailing (axon) and leading (dendrites) process form (Figure 1.3) (Barnes and Polleux, 2009; Liu *et al.*, 2016). Polarization is therefore the result of cross-talk between extracellular cues, intracellular signaling and extensive cytoskeletal rearrangements.

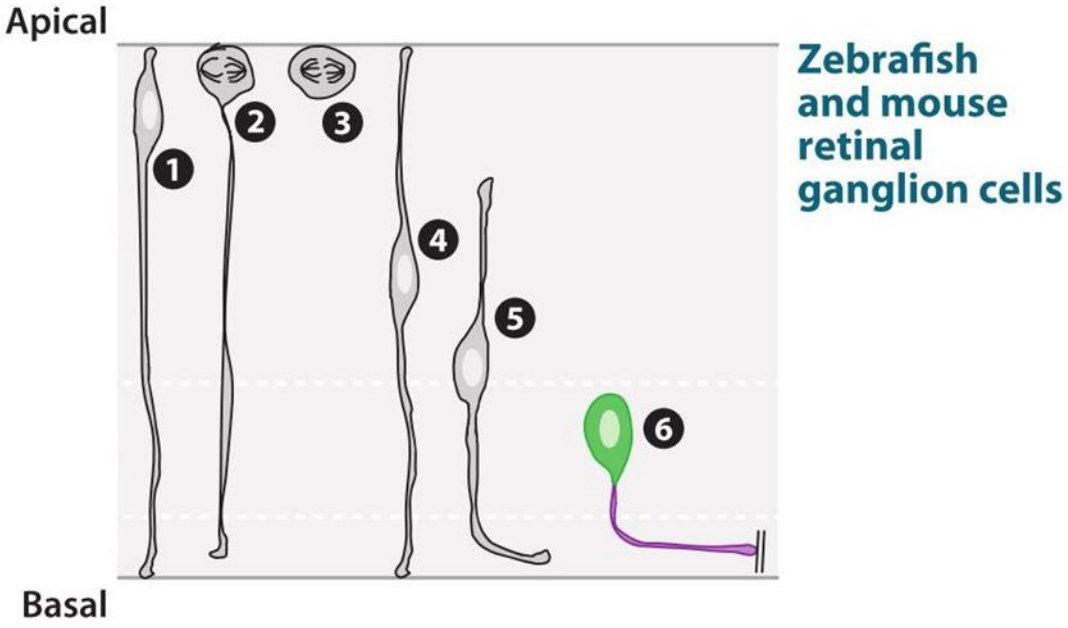

Figure 1.2: In vivo polarization of retinal ganglion cells in zebrafish (*Danio rerio*) and mouse (*Mus musculus*).

Neuroepithelial progenitors characterized by an apical and a basal attachment undergo asymmetrical cell division at the apical surface (1–3). Upon cell cycle exit, the nucleus undergoes basal translocation (4) and specifically loses its apical attachment while its basal process starts growing along the basal membrane (5). The axon (purple) develops from the basal process and the dendrite from the apical process (6; green). Figure and legend adapted from Barnes and Polleux, (2009). Republished with permission of Annual Review of Neuroscience from Barnes, A.P., and Polleux F. (2009). Establishment of axon-dendrite polarity in developing neurons. 32, 347-381 permission conveyed through Copyright Clearance Center, Inc.

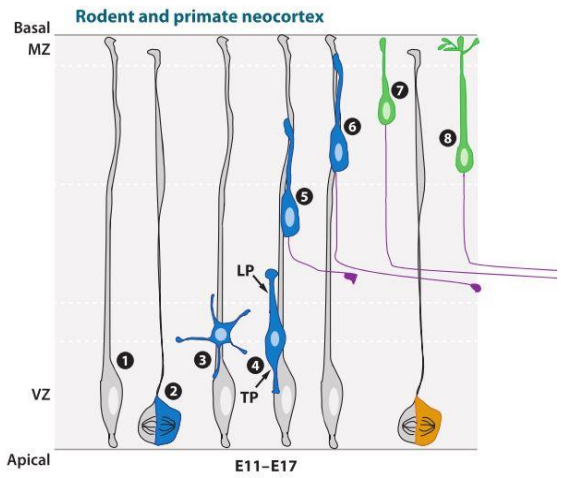

Figure 1.3: Polarization of radially migrating pyramidal neurons in the mammalian neocortex.

Neurons are generated between E11 and E17 by radial glial progenitors in the ventricular zone (VZ) of the mouse neocortex. These cells have a long basal process attached to the basal membrane and a short apical process on the ventricle side (1). Upon cell cycle exit through asymmetric cell division (2), the postmitotic neuron (blue) goes through a multipolar transition where multiple neurites emerge rapidly from the cell body (3) before two major processes form (4) and become the leading process (LP) and trailing process (TP). The cell body continues to translocate toward its final destination while the axon rapidly elongates (6). The leading process gives rise to the apical dendrite (green in 7), which initiates local branching in the marginal zone (MZ) while over the first postnatal week (until radial migration ends) the cell body will translocate ventrally (8). Figure and legend adapted from Barnes and Polleux, (2009). Republished with permission of Annual Review of Neuroscience from Barnes, A.P., and Polleux F. (2009). Establishment of axon-dendrite polarity in developing neurons. 32, 347-381 permission conveyed through Copyright Clearance Center, Inc.

In mammals, axons have been shown to develop in response to external growth cues such as BDNF (Polleux and Snider, 2010). In *in vitro* experiments with hippocampal neurons plated on stripes of adhesion molecules, the neurite which encounters BDNF first becomes the axon (Shelly *et al.*, 2007). BDNF acts through Ras mediated activation of cyclic adenosine monophosphate (cAMP) dependent protein kinase (PKA) (Figure 1.4) (Shelly *et al.*, 2007). Repulsive cues such as semaphorin 3A play a role in directing axon development in cortical neurons where axons develop ventrally (Polleux *et al.*, 1998; Chen *et al.*, 2008). In *Caenorhabditis elegans*, axonal development is regulated by netrin and its receptors deleted in colorectal cancer (DCC) and Uncoordinated 5 (unc-5) (Adler *et al.*, 2006). Soluble netrin gradients act as attractive cues in the presence of DCC (Adler *et al.*, 2006). With repulsive cues directing growth away from an undesirable area and gradients of attractive cues promoting growth in another direction, the growth cone can be steered to its final destination. Downstream effectors of netrin/DCC signaling include phosphatidylinositol 3 kinase (PI3K), phosphatase and tensin homolog deleted on chromosome 10 (PTEN) and the Ena/VASP (enabled/Vasodilator-stimulated phosphoprotein) homolog unc-34 which binds actin promoting filament formation and therefore filopodia formation (Fleming *et al.*, 2010; Polleux and Snider, 2010).

In response to external cues (such as BDNF or netrin), the serine/threonine kinase, liver kinase B1 (LKB1; in *C. elegans* Par-3) is translocated from the nucleus upon dimerization with sterile20-related kinase adaptor (STRAD) α/β (Dorfman and Macara, 2008) (Figure 1.4). In the cytoplasm, LKB1/STRAD is activated by PKA

phosphorylation (Collins *et al.*, 2000). LKB1/STRAD in turn propagates this signal by phosphorylating and activating the microtubule affinity regulating kinases (MARK) 1-4 which regulate microtubule dynamics by phosphorylating microtubule associated proteins (Figure 1.4) (Polleux and Snider, 2010).

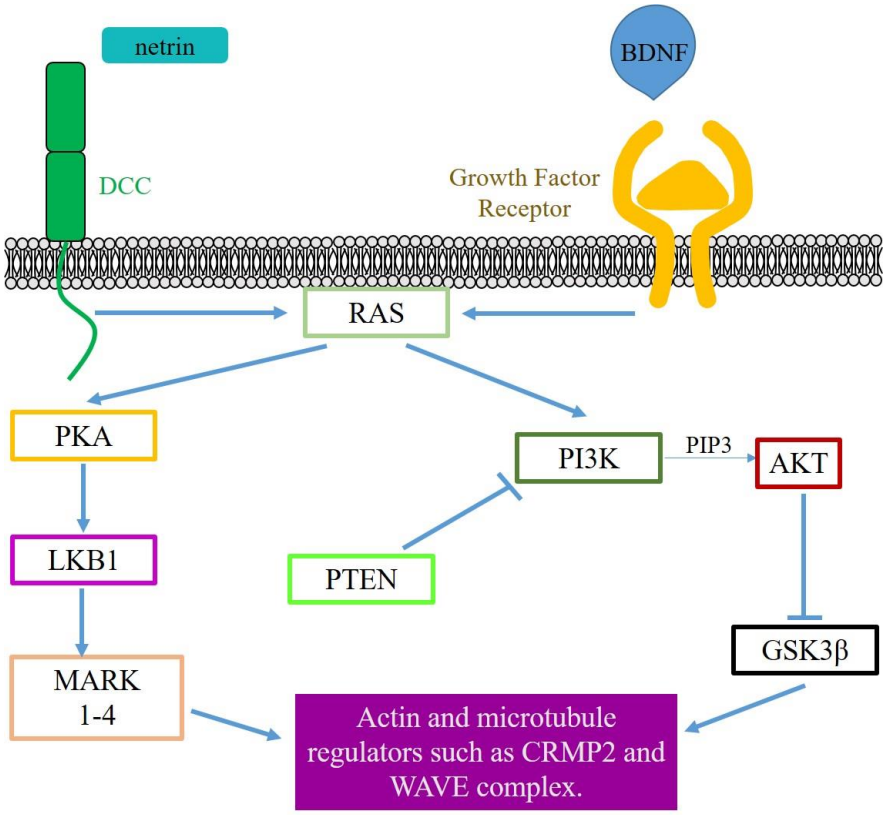

Figure 1.4: Signaling pathways governing axonal development.

External signaling cues such as netrins and BNDF, once bound to their receptors, activate signaling pathways that ultimately converge on the cytoskeleton. Gradients of these signaling cues direct axonal growth during development. Figure and legend created based on Barnes and Polleux, (2009) and Polleux and Snider, (2010).

Ras activation also leads to PI3K activity (Polleux and Snider, 2010; Zhong, 2016). PI3K has been shown to accumulate in the neurite destined to become the axon (Barnes and Polleux, 2009). Constitutively active PI3K overexpression leads to the development of multiple axonal processes while inhibition prevents axon formation (Barnes and Polleux, 2009). PI3K activity is antagonized by PTEN (Barnes and Polleux, 2009). PTEN dephosphorylation of phosphatidylinositol triphosphate (PIP3), the product of PI3K activation, limits PI3K signaling (Barnes and Polleux, 2009). Spatial regulation of PI3K signaling by PTEN allows for single axon development (Barnes and Polleux, 2009). Overexpression of PTEN leads to the loss of axonal development while PTEN knockdown allows multiple axons to develop (Barnes and Polleux, 2009).

PI3K downstream effectors include protein kinase B (AKT) which is recruited to the membrane via PIP3 binding to its plextrin homology domain (Zhong, 2016). Once at the membrane, AKT is phosphorylated and activated by other membrane targeted kinases (Barnes and Polleux, 2009). Active AKT has been shown to localize to polarized growth cones and constitutively active AKT gives rise to multi-axon neurons (Barnes and Polleux, 2009). This mimics the effect of PI3K overexpression and places AKT in the PI3K pathway governing polarization.

Given the dynamicity of the growth cone, it is not surprising that the signaling cascades dictating axonal development converge on the cytoskeleton. In some instances, the action of the cytoskeleton controls signaling forming a type of feedback loop. PI3K for example, interacts with Shootin1 (Toriyama *et al.*, 2006) and Singar 1/2 (Mori *et al.*, 2007). Of these two proteins, Shootin1 overexpression is sufficient to cause multi-axon

development (Barnes and Polleux, 2009). Interestingly, Shootin1 is transported to the growth cone in a myosin dependent manner where is co-localizes with active PI3K (Barnes and Polleux, 2009). Additionally, evidence suggests there are two pools of PIP3 at the growth cone, one produced by locally active PI3K and another transported pool (Barnes and Polleux, 2009). The transportation of PIP3 vesicles to the forming axon is dependent on guanylate kinase associated kinesin (GAKIN) (Barnes and Polleux, 2009). GAKIN mediated transport of extra PIP3 may help maintain axon integrity through maintenance of a high PIP3 concentration.

At the heart of polarity regulation lies glycogen synthase kinase 3 β (GSK3β). GSK3β is constitutively active in its unphosphorylated form (Barnes and Polleux, 2009; Polleux and Snider, 2010). GSK3β sits at the crossroads between signal cascades and direct regulation of cytoskeletal elements. GSK3β is phosphorylated and deactivated by AKT in the forming axon (Barnes and Polleux, 2009). Global inhibition of GSK3β activity leads to multi-axon formation indicating that GSK3β activation must be maintained in neurites destined to become dendrites while GSK3β must be inhibited by AKT during axonal development (Barnes and Polleux, 2009).

The cytoskeleton then must support the transport of factors needed for axonal development while rapid rearrangement occurs. This rearrangement occurs through the action of multiple regulating proteins in addition to Ena/VASP such as collapsing response mediator protein-2 (CRMP-2) (Barnes and Polleux, 2009). CRMP-2 is regulated by GSK3β and binds directly to tubulin and the WASP-family verprolin homologous (WAVE) protein complex to regulate both microtubule and actin dynamics (Barnes and Polleux, 2009). Adenomatous polyposis coli another microtubule binding protein

regulated by GSK3β, is enriched in the forming axon at early time points (Barnes and Polleux, 2009). GSK3β has also been shown to alter the phosphorylation state and behavior of the microtubule associated proteins (MAPs) Tau and MAP1b (Barnes and Polleux, 2009).

1.1.4 Neurodegeneration

The pathways that govern neural development and maintain cell function are susceptible to myriad insults which eventually lead to disease state development. These insults include environmental factors, traumatic injury, inherited and spontaneous mutations, and disrupted/misregulated signaling (Brady and Morfini, 2017; Prior *et al.*, 2017; Wilson *et al.*, 2017). Whether the insult is intra- or extracellular, the end result is synapse loss and the eventual death of the neuron (Liu *et al.*, 2011; Brady and Morfini, 2017; Prior *et al.*, 2017).

One of the hallmarks of disease state development and neurodegeneration is the disruption of cargo transport through the axon (Brady and Morfini, 2017; Prior *et al.*, 2017). The molecular motor mediated movement of cargo is established during development and is maintained throughout the life of the cell (Brady and Morfini, 2017). In the disease state aberrant signaling by misregulated kinases leads to inhibition of motors and regulatory elements (Kanaan *et al.*, 2013; Martin *et al.*, 2013b).

Though many kinases contribute to disease state development (Martin *et al.*, 2013b; Brady and Morfini, 2017), for the sake of brevity only the action of GSK3β and Cdk5 will be covered. GSK3β activity is regulated through inhibitory phosphorylation at serine 9 (Kirouac *et al.*, 2017). The tight control of this site allows for normal axonal

development and neuronal signaling (Llorens-Martin *et al.*, 2014; Kirouac *et al.*, 2017). Disruption of signaling pathways (such as AKT activity) that inhibit GSK3β are common to the development of neurodegenerative disease (Llorens-Martin *et al.*, 2014).

In the development of Alzheimer's Disease (AD), aberrant signaling through amyloid precursor protein (APP) has been shown to upregulate GSK3β activity (Kirouac *et al.*, 2017). Disease state processing of APP by β- and γ-secretase generates the extracellular fragment amyloid β (Aβ) and the APP intracellular fragment (AICD) (Kirouac *et al.*, 2017). AICD has been shown to bind and upregulate GSK3β which in turn phosphorylates APP at threonine 688 increasing disease state cleavage (Kirouac *et al.*, 2017). This creates a positive feedback loop which keeps GSK3β active in the disease state. As part of its non-disease state roles, GSK3β regulates cytoskeletal elements (Barnes and Polleux, 2009; Polleux and Snider, 2010). Increased GSK3β activity leads to increased phosphorylation and misregulation of these elements including molecular motors such as kinesin-1 and MAPs such as Tau (Llorens-Martin *et al.*, 2014; Brady and Morfini, 2017). GSK3β is also upregulated independently of AICD in diseases such as Progressive Supranuclear Palsy, Pick's Disease and other forms of dementia (Ferrer *et al.*, 2002; Ferrer *et al.*, 2003).

Unlike other members of the cyclin dependent kinase family, Cdk5 is not regulated by cyclin expression but is active in post-mitotic neurons because of its activators p35/p39 (Liu *et al.*, 2016). These membrane bound activators are prone to ubiquitination and degradation leading to short bursts of Cdk5 activity (Liu *et al.*, 2016). While active, Cdk5 has been shown to regulate the activity of other kinases including GSK3β (Liu *et al.*, 2016). In addition to controlling neurite formation, Cdk5 plays a role

in synaptic formation, myelination and maintenance of mitochondrial function (Liu *et al.*, 2016). In the disease state, prolonged calcium influx leads to calpain mediated cleavage of p35 and p39 into their more stable forms p25 and p29 (Lee *et al.*, 2000; Kurbatskaya *et al.*, 2016; Liu *et al.*, 2016). The Cdk5/p25 interaction leads to the upregulation of Cdk5 activity and disease state phosphorylation of APP at threonine 688 (Liu *et al.*, 2016). Cdk5/p25 has also been shown to directly affect the cytoskeleton through phosphorylation of the WAVE complex, CRMP-2 and MAPs such as Tau (Liu *et al.*, 2016). In addition to its association with Cdk5, p25 has been shown to bind and upregulate GSK3β activity (Chow *et al.*, 2014).

The disease state misregulation of signaling as demonstrated by GSK3β and Cdk5, does not occur without extracellular cues or other perturbation. For example, neurodegenerative diseases such as Alzheimer's Disease share disease state conditions with Diabetes including insulin resistance as the result of chronic metabolic stress and inflammation (Liu *et al.*, 2011). It is not clear whether these factors are the cause or result of disease state development (Liu *et al.*, 2011). More obvious cause-and-effect examples are mutations in proteins such as APP, Presinilin (1 and 2) and Tau (Bull *et al.*, 2012; Multhaup *et al.*, 2015; Moustafa *et al.*, 2018). APP is a single pass transmembrane protein enriched at synapses (Multhaup *et al.*, 2015). Many functions have been proposed for APP including participation in synapse formation, long range signaling and axonal transport (Multhaup *et al.*, 2015). As part of its function APP is cleaved by α-, β- and γ-secretases (Multhaup *et al.*, 2015). In the non-disease state, cleavage by α- and β-secretase allows for normal function (Multhaup *et al.*, 2015). APP mutations in secretase

recognition sites leaves it more vulnerable to disease state γ-secretase cleavage (Multhaup *et al.*, 2015).

The Presinilin genes encode components of the γ-secretase complex which participates in the disease state cleavage of APP into the pathogenic peptide Aβ (Hutton and Hardy, 1997). Mutations in Presinilin-1 have been proposed to increase γ-secretase activity and the generation of Aβ (Hutton and Hardy, 1997; Sun *et al.*, 2017). Tau missense mutations can impair microtubule binding and silent mutations affect alternate splicing of Tau thereby shifting isoform expression (Yen *et al.*, 1999). Tau plays an important role in the regulation of axonal transport and disruption of its functions leads to impaired cargo transport (Heins *et al.*, 1991; LaPointe *et al.*, 2009; Kanaan *et al.*, 2012).

1.2 Axonal Transport

1.2.1 Fast Axonal Transport

The first observation of axonal transport was made four decades after Ramón y Cajal received his Nobel Prize (Stenoien and Brady, 1999). Experiments by Weiss and Hiscoe showed that materials manufactured in the neuronal cell body were essential to the maintenance of the axon (Weiss and Hiscoe, 1948). When bulk flow was first described, it was found to move at 1-2 mm/day (Stenoien and Brady, 1999). While this movement fulfilled some of the requirements for axonal maintenance, it quickly became apparent that the slow flow of material could not keep up with the fast signals that were known to travel down the axon (Stenoien and Brady, 1999). Twenty years of further study showed that a component of this bulk flow moved at much faster rates (up to 400 mm/day) in both the anterograde and retrograde directions (Stenoien and Brady, 1999).

Fast axonal transport is associated with membrane bound proteins and organelles. The size of the transported proteins/organelles has been shown to dictate the rate of transport with larger organelles such as mitochondria moving as slow as 50 mm/day (Stenoien and Brady, 1999). Not even the slowest form of fast axonal transport could be explained by the flow of material which governs slow axonal transport. As evidence for some directed transport mechanism, it was found that disruption of the microtubule network inhibited fast axonal transport (Stenoien and Brady, 1999).

By the mid 1980s the idea of motor mediated movement was not new though it had yet to be linked to fast axonal transport (Stenoien and Brady, 1999). Muscle myosin was first described in 1864 by Wilhelm Kühne (Hartman and Spudich, 2012) and, Gibbons and Rowe showed that dynein isolated from cilia had ATPase activity (Gibbons and Rowe, 1965). It was known that myosin interacted with actin and dynein with microtubules (Stenoien and Brady, 1999). Therefore, in light of the microtubule dependence of fast axonal transport it was hypothesized that dynein was involved (Stenoien and Brady, 1999). Attempts were made to identify dynein in the brain (Murphy *et al.*, 1983) but ATP analog studies showed that a third motor was required for cargo transport (Stenoien and Brady, 1999). The inhibitory analog, 5'-adenylyl-imidodiphosphate (AMP-PNP) has a mild effect on both myosin and dynein but, once perfused into squid axoplasm, AMP-PNP completely stopped fast axonal transport (Vale *et al.*, 1985; Stenoien and Brady, 1999). This high affinity for the microtubule in the presence of AMP-PNP was used to purify the motor now called kinesin (Vale *et al.*, 1985).

1.2.2 Kinesin Motors

Experiments in the early 1980s pointed to an as yet unknown 'translocator' which moved microtubule associated cargo in the axon, specifically squid axoplasm (Brady *et al.*, 1982; Allen *et al.*, 1985). Vale purified a novel ATPase from axoplasm and bovine brain which was able to slide microtubules in gliding filament assays and move beads along microtubules in motility assays (Vale *et al.*, 1985). The word kinesin was derived from the Greek kinein (to move) (Vale *et al.*, 1985) and this first kinesin became the founding member of a large class of proteins (Hirokawa *et al.*, 2009).

There are fourteen kinesin families, kinesin-1 through kinesin-14, designated based on shared features determined by sequence alignment and phylogenetic analysis (Figure 1.5) (Hirokawa *et al.*, 2009). Regardless of family, all kinesins have ATP hydrolyzing motor domains and coiled-coil domains which facilitate dimerization (Figure 1.5) (Vale, 2003; Hirokawa *et al.*, 2009).

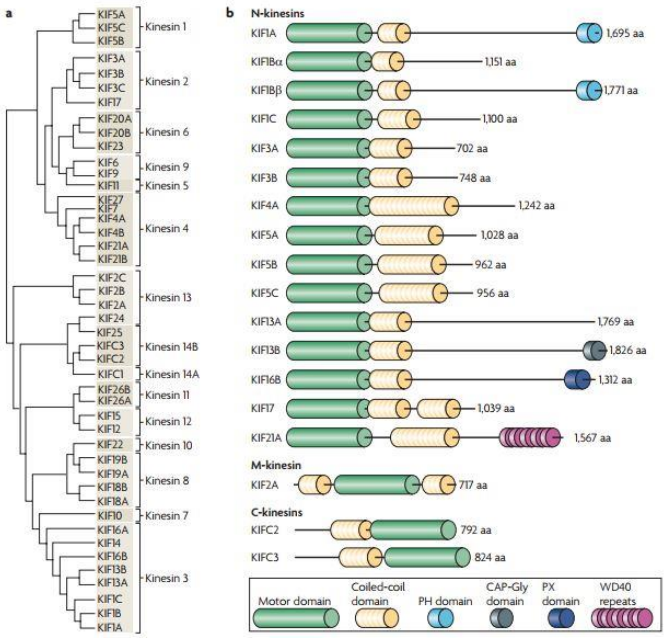

Figure 1.5: Families and structures of mammalian kinesins.

a) A phylogenetic tree of all 45 kinesins (KIFs) grouped into 14 families (kinesin-1 to -14). **b)** Domain structures of the major kinesins. In general, kinesins comprise a kinesin motor domain and a coiled-coil domain. There are also gene specific domains, such as the pleckstrin homology (PH), the CAP-Gly domain (a conserved, Gly-rich domain of ~42 residues found in some cytoskeleton-associated proteins) and WD40 repeats. The fourteen families of kinesins can be grouped into N-kinesins, M-kinesins and C-kinesins, which contain their motor domain at the amino terminus, in the middle or at the carboxyl terminus, respectively. N-kinesins are plus end-directed, C-kinesins are minus end-directed and M-kinesins depolymerize microtubules. The three types of kinesin are grouped as indicated. Figure and legend adapted from Hirokawa *et al.* (2009). Reprinted by permission from Copyright Clearance Center: Springer Nature, Nature Reviews Molecular Cell Biology, Kinesin superfamily motor proteins and intracellular transport. Hirokawa, N., Noda, Y., Tanaka, Y., and Niwa, S. (2009).

The motor domain position of a kinesin can give some insight into its function. Kinesins with N-terminal motor domains are plus end directed, C-terminal motor domains are minus end directed and kinesins with motor domains in the middle of their sequence act to depolymerize microtubules (Hirokawa *et al.*, 2009). Of the fourteen families, there are three major players involved in axonal cargo transport: kinesin-1, -2 and -3 though kinesin-4 has been found to associate with cargo as well (Hirokawa *et al.*, 2009).

In vertebrates, kinesin-1 is a heterotetramer comprised of two heavy chains (kinesin heavy chain, KHC) containing the motor and coiled-coil domains, and two light chains (kinesin light chains, KLC) which bind to the C-termini of the KHCs and facilitate cargo binding (Vale, 2003). Vertebrates have three KHC genes, two are ubiquitously expressed while the third is neuronally expressed (Brady and Morfini, 2017). Two KLCs (KLC1 and 2) are neuronally expressed (Brady and Morfini, 2017). Combinations of heavy and light chains allow for at least six different kinesin-1 holoenzymes (Brady and Morfini, 2017). In addition to different KLCs, a number of adaptor proteins have been identified for kinesin-1. They include: Milton and Miro which appear to facilitate mitochondrial binding (Wang and Schwarz, 2009), unc-76 from *C. elegans* (Fasiculation and elongation protein zeta 1 (FEZ1) in humans) which allows binding to presynaptic vesicles (Toda *et al.*, 2008) and Jun N-terminal kinase (JNK) interacting protein 1 (JIP1) which binds to APP transporting vesicles (Inomata *et al.*, 2003).

Given the importance of kinesin-1, the motor must be carefully regulated to ensure the most efficient delivery of cargo. In addition to autoinhibition, the motor can be

regulated by phosphorylation, MAPs and the microtubule track on which it walks (Verhey and Hammond, 2009).

In the absence of cargo, kinesin-1 is autoinhibited by interactions between the motor domain, KHC tail domains and the KLC (Figure 1.6) (Verhey and Hammond, 2009). The tail domain contains the conserved sequence QIAKPIRP which has been shown to interact with the motor domain preventing nucleotide exchange (Figure 1.6) (Verhey and Hammond, 2009). Autoinhibition is further regulated by phosphorylation. Analytical ultracentrifugation experiments show that JNK3 mediated phosphorylation of serine 175 stabilizes kinesin-1's autoinhibited state (Figure 1.6) (DeBerg *et al.*, 2013). Both cargo binding and motor-adaptor protein interactions (FEZ1 and JIP1) have been shown to relieve autoinhibition (Figure 1.6) (Verhey and Hammond, 2009).

Phosphorylation of KLC has also been shown to regulate motor-cargo interactions and therefore cargo delivery. There are a number of kinases that act on KLC including extracellular-signal regulated kinase (ERK) and GSK3β (Morfini *et al.*, 2002; Vagnoni *et al.*, 2011). ERK phosphorylates KLC serine 460 (Figure 6) (Vagnoni *et al.*, 2011). Phosphorylation of this site selectively prevents KLC interactions with calsyntenin 1 but not other adaptors such as JIP1 (Vagnoni *et al.*, 2011). Calsyntenin 1 is a cadherin-like protein which facilitates kinesin-1 interactions with cargo and regulates microtubule polarity during axonal development (Lee *et al.*, 2017). Interestingly, adaptor protein phosphorylation also regulates interactions with the motor (Figure 1.6) (Chua *et al.*, 2012). GSK3β is thought to have multiple recognition sites on KLC (Figure 1.6) (Morfini *et al.*, 2002). When perfused into the axoplasm, active GSK3β slows anterograde

transport (Morfini *et al.*, 2002). Spatial control of kinesin-1 holoenzyme phosphorylation regulates both the activation of the motor and its interaction with cargo.

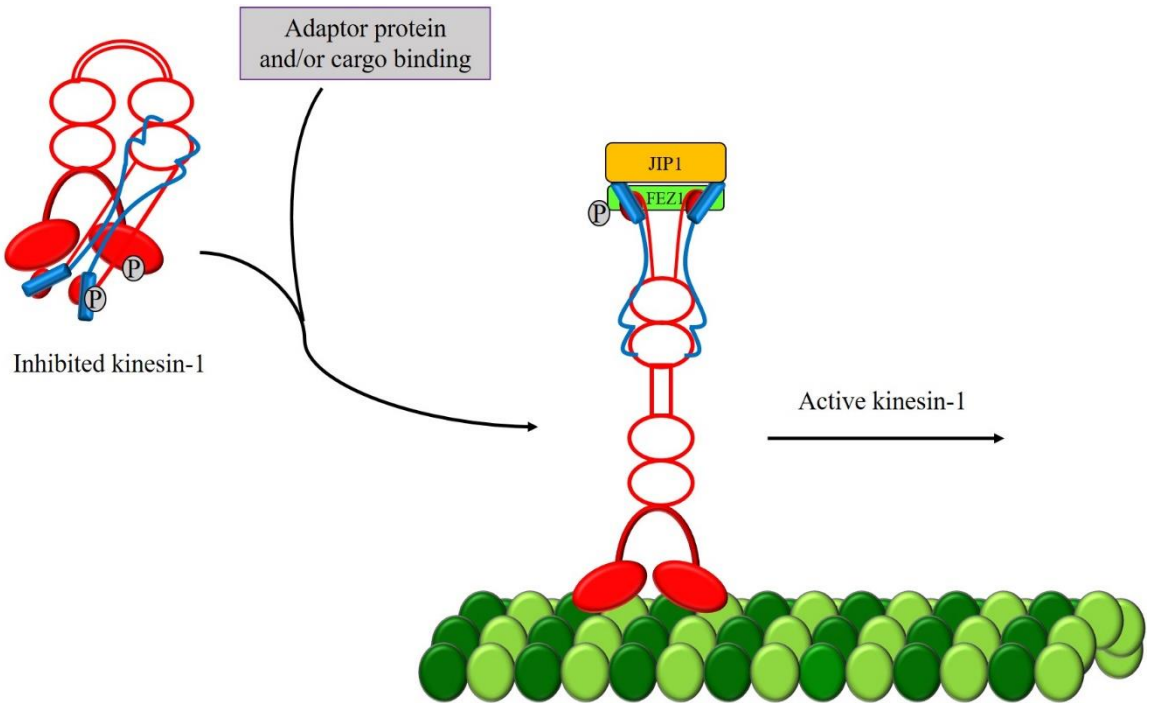

Figure 1.6: Kinesin-1 activity is regulated by autoinhibition, phosphorylation and adaptor proteins/cargo.

Kinesin-1 (red/blue) is autoinhibited in a folded conformation though interactions between the KHC (red) tail conserved sequence QIAKPIRP and the KLC (blue) with the motor domains. Phosphorylation (gray) of the motor domain at serine 175 stabilizes this autoinhibited conformation. Phosphorylation of the KLC disrupts interactions with specific adaptors. Kinesin-1 autoinhibition can be relieved by dephosphorylation of serine 175 and the KLC, cargo binding and/or binding of adaptor proteins (FEZ1 and JIP1) to the KLC and KHC respectively. Phosphorylation of adaptor proteins (FEZ1) has been shown to facilitate motor-adaptor interactions. Figure and legend created based on Morfini *et al.* (2002), Verhey and Hammond, (2009), Vagnoni *et al.* (2011), Chua *et al.* (2012) and DeBerg *et al.* (2013).

1.2.3 Neuronal Tubulin

Though evidence for microtubules was first found in early electron micrographs, it was not till 1963 that they were recognized as distinct structural elements (van de Willige *et al.*, 2016). Microtubules are polymers of αβ-tubulin heterodimers that assemble to form a hollow tube of on average 13 protofilaments (Yu *et al.*, 2015; van de Willige *et al.*, 2016). Both α- and β-tubulin are globular with disorganized, negatively charged C-terminal tails (CTT) (Yu *et al.*, 2015). Microtubule polymerization is facilitated by β-tubulin GTP binding (Desai and Mitchison, 1997). Tubulin dimers polymerize with a fixed α-β polarity and new dimers are added to the β-tubulin end (plus end) of the growing microtubule (Figure 1.7) (Geyer *et al.*, 2015; van de Willige *et al.*, 2016). Microtubules are considered to have dynamic instability because of their ability to undergo rapid rounds of growth and shortening (van de Willige *et al.*, 2016). A growing microtubule generally has a lattice of predominantly GDP bound dimers and a cap of predominantly GTP dimers (Figure 1.7) (Geyer *et al.*, 2015; van de Willige *et al.*, 2016). This GTP cap contributes to the stability of the microtubule and GTP hydrolysis in the cap is one of the factors that contributes to depolymerization (Desai and Mitchison, 1997). It has been shown that the nucleotide bound state affects the structure of the dimers in the lattice (Geyer *et al.*, 2015). GTP bound tubulin has a compacted α-tubulin subunit and GTP hydrolysis relieves this compaction (Geyer *et al.*, 2015). Interestingly, some microtubule bound proteins track the GTP cap by recognizing these conformational changes (Geyer *et al.*, 2015).

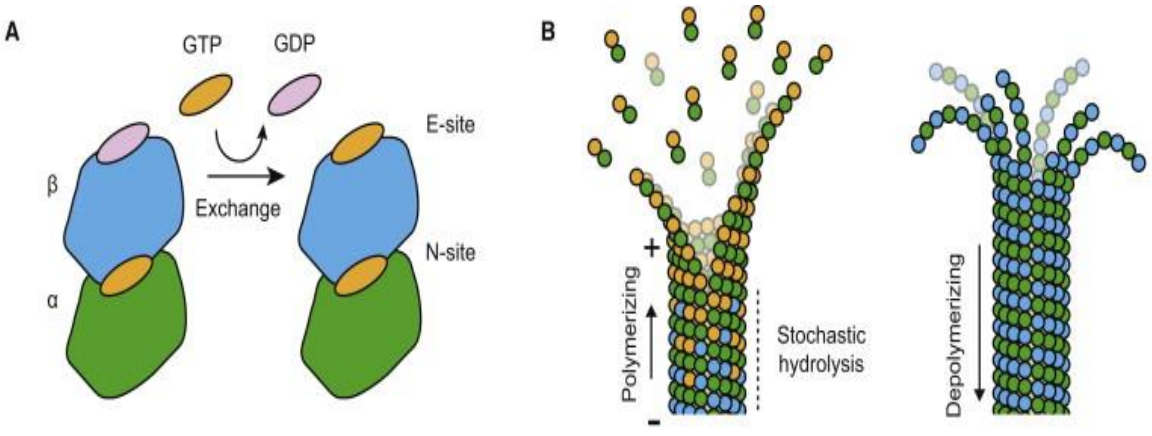

Figure 1.7: Tubulin dimer nucleotide exchange and microtubule polymerization.

A) Both α- and β-tubulin bind GTP however, nucleotide exchange by β-tubulin (in the E site) drives microtubule dynamics. **B)** While GTP is bound to the E site (yellow β-tubulin), polymerization occurs and as long as the growing microtubule maintains a GTP cap growth will continue. GTP hydrolysis (blue β-tubulin) within the lattice is not sufficient to lead to catastrophe though this hydrolysis does increase the likelihood of lattice defects and once hydrolysis occurs in the GTP cap, catastrophe is inevitable (Alushin *et al.*, 2014). Figure and legend adapted from Alushin *et al.* (2014). Reprinted from Cell, 157/5, Alushin, G.M., Lander, G.C., Kellogg, E.H., Zhang, R., Baker, D., and Nogales, E., High-resolution microtubule structures reveal the structural transitions in alphabeta-tubulin upon GTP hydrolysis, Pages No. 1117-1129, Copyright (2014) with permission from Elsevier.

As previously discussed, kinesin-1 is regulated by autoinhibition, phosphorylation and adaptor protein/cargo binding. However, the microtubule track is itself a major point at which regulation of axonal transport takes place. Microtubule polarity ensures that kinesin-1 and other major kinesins move cargo towards the synapse (anterograde) while the minus end directed motor cytoplasmic dynein moves cargo towards the cell body (retrograde) (Stenoien and Brady, 1999).

In humans, nine α-tubulin and ten β-tubulin genes have been identified (Aiken *et al.*, 2017). In the brain, βIVa is the predominant β tubulin isoform expressed though βIII, βIIa and βIIb are also expressed (Leandro-Garcia *et al.*, 2010). βI tubulin is found in all tissues (Leandro-Garcia *et al.*, 2010). Of the nine α-tubulin isoforms, α1 and α8 are of great importance in neural development and axon growth (Romaniello *et al.*, 2015).

In addition to heterodimer diversity, tubulin is subject to a plethora of post translational modifications including tyrosination, detyrosination, glutamylation, phosphorylation, and glyclation (Figure 1.8) (Yu *et al.*, 2015). These modifications are often enriched in different cell types and cell cycle time points (Yu *et al.*, 2015). In the growth cone, dynamic microtubules are enriched in tyrosination but the stable microtubules of the axon are detyrosinated, acetylated and glutamylated (Yu *et al.*, 2015). Tyrosination/detyrosination takes place on α-tubulin CTT (Figure 1.8) (Yu *et al.*, 2015). α-Tubulin is initially expressed with a C-terminal tyrosine which can be removed and reattached as needed (Yu *et al.*, 2015). Detyrosination exposes a glutamic acid (E-hook) and can be made permanent by removal of this E-hook (Yu *et al.*, 2015).

In vivo, kinesin-1 has been shown to prefer binding detyrosinated microtubules (Dunn *et al.,* 2008). *In vitro* experiments confirmed this increased affinity along with a slightly increased velocity though no change in run length was observed (Kaul *et al.*, 2014).

α-Tubulin is also acetylated on its lumenal surface at lysine 40 while β tubulin is acetylated at lysine 252 (Figure 1.8) (Yu *et al.,* 2015). *In vitro* experiments show that compared to deactylated microtubules, lysine 40 acetylation does not affect kinesin-1 run length, velocity or affinity for the microtubule (Kaul *et al.*, 2014). It is to be noted that kinesin-1 does have a longer run length on acetylated versus detyrosinated microtubules (Kaul *et al.*, 2014). On acetylated and detyrosinated microtubules as found in the axon, kinesin-1 has both increased affinity and run length compared to tyrosinated, deacetylated microtubules (Kaul *et al.*, 2014). More recent work suggests that this increased run length observed for kinesin-1 on acetylated microtubules is due to increased microtubule bundling and therefore kinesin-1 binding site availability (Balabanian *et al.*, 2017). The acetylated, detyrosinated microtubules found in the axon enhance kinesin-1 motility which in turn allows for more efficient cargo transport. Interestingly, detyrosination has been shown to act as an axonal targeting cue for kinesin-1 (Konishi and Setou, 2009).

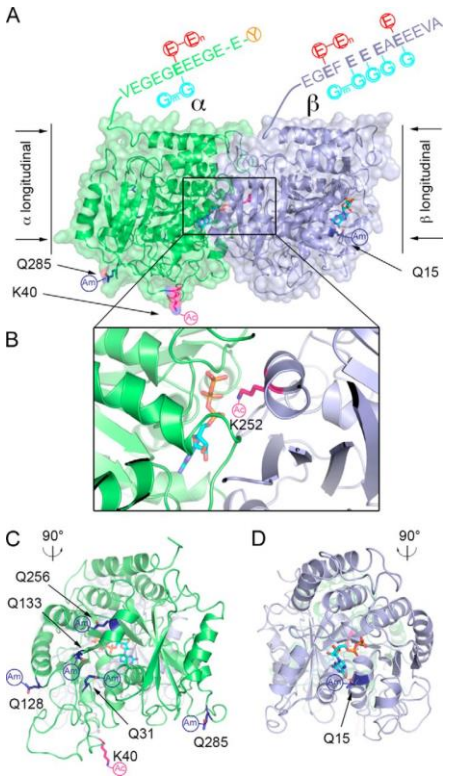

Figure 1.8: Posttranslational modifications of the αβ tubulin heterodimer.

A. ribbon representation of the tubulin heterodimer (green, α-tubulin; blue, β-tubulin) with CTT shown using sequences for the α1A and βIVb tubulin isoforms. Sites of acetylation (magenta) and polyamination (dark blue) are shown in stick representation. The α-tubulin C-terminal tyrosine (orange) is subject to enzymatic removal (detyrosination/tyrosination). Tail glutamates are subject to glutamylation and glycylation. B. Zoomed-in view showing the acetylated β-tubulin lysine 252. C. and D. view of the α-tubulin (C) and β-tubulin (D) longitudinal interfaces showing the position of mapped polyamination sites as dark blue sticks. α-Tubulin lysine 40 is shown in stick representation (magenta). Am, amination. Ac, acetylation. Figure and legend adapted from Yu *et al.,* (2015) in accordance with the Creative Commons Attribution license.

1.2.4 Neuronal MAPs

Microtubule associated proteins (MAPs) as their name suggests, bind to the microtubule cytoskeleton. These proteins include the microtubule tip tracking proteins (+TIPs), MAP1, MAP7, MAP2 and MAPT (Tau).

+TIPs track the growing end of the microtubule. They include the end binding proteins (EB 1-3), EB-dependent +TIPs and EB-independent +TIPs (van de Willige *et al.*, 2016). EBs track the GTP cap by recognizing structural changes in the tubulin dimer upon GTP binding (van de Willige *et al.*, 2016). EB3 is upregulated during neurogenesis however, neurite growth and axon formation have been shown to depend on both EB1 and 3 in neuroblastoma cells and *Drosophila* (van de Willige *et al.*, 2016). Depletion of EB1 in axonal development leads to microtubule splaying and disorganization (van de Willige *et al.*, 2016). While tracking the plus end, EBs serve as scaffolds for other +TIPs. The higher affinity of EB1/3 for the microtubule has been hypothesized to facilitate scaffold maintenance in the growing axon (van de Willige *et al.*, 2016). Proteins that scaffold with EB1/3 have conserved binding motifs such as an SxIP (serine/threonine-x-isoleucine/leucine-proline) or CAP-gly (cytoskeletal-associated protein glycine rich) (van de Willige *et al.*, 2016). Proteins with SxIP and CAP-gly sequences participate in the maintenance of the axonal cytoskeleton facilitating both anterograde and retrograde transport (van de Willige *et al.*, 2016).

MAP1 A and B were initially characterized as microtubule stabilizers. Early reports suggested that MAP1B localizes to the tips of growing axons (Black *et al.*, 1994).

In mouse dorsal root ganglion cells, knock out of MAP1B led to axon turning defects and the complete deletion of MAP1B has been shown to prevent development of the corpus callosum (Halpain and Dehmelt, 2006). MAP1B is therefore involved in the cytoskeletal regulation and axonal development.

As with the other MAPs above, MAP7 (ensconsin) was first described as a microtubule stabilizing protein (Bulinski and Bossler, 1994). Since its characterization, it has been demonstrated that MAP7 plays a role in activating kinesin-1 in neurons through interactions between the kinesin-1 'hinge' region and MAP7 N-terminal (Barlan *et al.*, 2013). Though MAP7 activates kinesin-1, it has been shown to inhibit kinesin-3 (Monroy *et al.*, 2017). This preferential activation/inhibition further demonstrates the complexity of cargo transport regulation.

Of the MAPs, MAP2 and Tau are the most frequently studied. MAP2 has three isoforms (a, b and c) whose expression is developmentally regulated (Tucker *et al.*, 1988). MAP2c is expressed during development while MAP2a/b are expressed in mature neurons (Dehmelt and Halpain, 2005). MAP2c has been shown to be sufficient to induce neurite formation (Dehmelt and Halpain, 2005). This is thought to be due to its ability to bind both microtubules and actin thereby coordinating microtubule and actin dynamics (Dehmelt and Halpain, 2005). As the neuron develops, MAP2 is excluded from the forming axon and in mature neurons, MAP2 localizes to dendrites (Dehmelt and Halpain, 2005). Conversely, Tau is confined to the forming axon and is excluded from dendrites (Dehmelt and Halpain, 2005). Both MAP2 and Tau have similar microtubule binding repeat regions, have been shown to act as scaffolding proteins and are known to bundle microtubules (Dehmelt and Halpain, 2005). The segregation of MAP2 and Tau must

therefore relate to their functions in the dendrite and axon respectively. Tau has been shown participate in many aspects of axonal transport including the regulation of kinesin-1 and -3 (Lessard and Berger; Stern *et al.*, 2017). A number of neurodegenerative diseases, grouped as Tauopathies, develop due to aberrant expression or regulation of Tau within the neuron (LaPointe *et al.*, 2009; Stern *et al.*, 2017; Yin *et al.*, 2017).

1.3 Tau

1.3.1 Roles of Tau in Axonal Transport

Tau was first identified in 1975 and at the time, it was thought to be a microtubule nucleating factor (Weingarten *et al.*, 1975). Later work found that Tau bound the microtubule surface with high affinity through a number of microtubule binding repeats which each have a weak affinity for the microtubule (Butner and Kirschner, 1991).

Since its discovery, Tau has been shown to have many roles beyond microtubule nucleation. This includes roles within the axon such as regulation of microtubule dynamics, participation in signaling cascades and inhibition of kinesin-1 motility (Stern *et al.*, 2017). While Tau is generally thought to stabilize microtubules, its function in the regulation of microtubule dynamics is more complex. Work done by Panda *et al.* shows that Tau affects specific aspects of microtubule growth and shortening (Panda *et al.*, 2003). 4RL-Tau reduces the rate of shortening while 3RL-Tau has no effect (Panda *et al.*, 2003). However, both isoforms increase microtubule growth and reduce dynamicity (Panda *et al.*, 2003).

Tau participates in signaling cascades in a number of ways. Tau has been shown to inhibit the deacetylation activity of histone deacetylase 6 (HDAC6) which acts on

microtubules (Perez *et al.*, 2009). Additionally, Tau's phosphatase activating domain (PAD) has been shown to play a role in the regulation of bulk cargo movement through the axon (LaPointe *et al.*, 2009). The PAD has been shown to act in the activation of the protein phosphatase 1 (PP1) which in turn leads to the activation of GSK3β (Morfini *et al.*, 2002; Kanaan *et al.*, 2011; Kanaan *et al.*, 2012). Outside of the axon in the dendrite, Tau acts as a scaffolding protein to mediate the interaction between Fyn kinase and post synaptic density 95 (PSD95) in the disease state (Ittner *et al.*, 2010). This interaction leads to the phosphorylation and toxic activation of the N-methyl-D-aspartate (NMDA) receptor (Ittner *et al.*, 2010). In addition to all of the above roles, Tau has been found in the nucleus where it is thought to protect DNA (Sultan *et al.*, 2011).

1.3.2 Regulation of Tau Isoform Expression

There are six human Tau isoforms (Figure 1.9) which arise from the alternative splicing of a single Tau gene on chromosome 17 (Andreadis, 2005). All the isoforms have a PAD and proline rich region (PRR) while isoforms differ based on number of acidic inserts (0-2) and microtubule binding repeats (3-4) (Figure 1.9) (Stern *et al.*, 2017). In the *mapT* gene, exon 10 encodes the second microtubule binding repeat and regulation of exon 10 inclusion controls 3 repeat (3R)- versus 4R-Tau isoform expression. This regulation occurs developmentally and 3R isoforms are exclusively expressed in the developing brain. In the adult brain 3R and 4R isoforms are expressed equally (Andreadis, 2005; Yin *et al.*, 2017). Splicing of exons 2 and 3 controls the number of acidic inserts (AI) and give rise to short (0 AI), intermediate (1 AI) and long (2 AI) isoforms (Yin *et al.*, 2017).

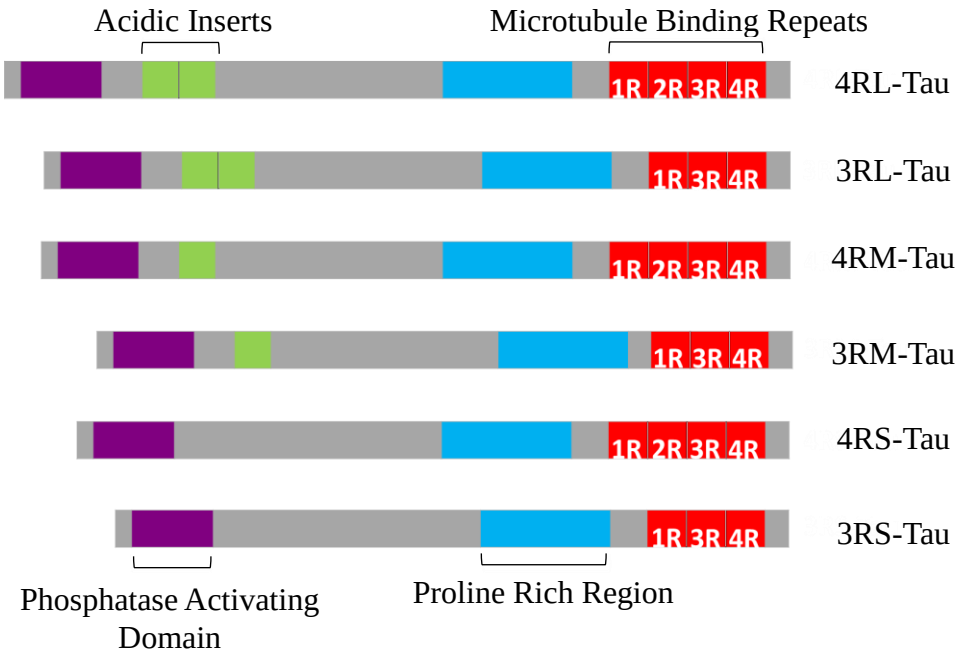

Figure 1.9 Tau isoforms.

Six Tau isoforms are expressed in the adult brain as the result of alternative splicing of the gene *mapT (Ballatore et al., 2007)*. All isoforms have a phosphatase activating domain (purple) and a proline rich region (blue). The isoforms differ based on number of acidic inserts (green; 0, 1 or 2) and microtubule binding repeats (red; 3 or 4). Inclusion of acidic inserts and the second microtubule binding repeat is regulated by alternative splicing of exons 2, 3 and 10. Figure and legend based on Ballatore *et al.*, (2007).

The regulation of exon 10 splicing is critically important for the maintenance of the neuron. Defects in exon 10 splicing lead to shifts in the ratio of 3R vs 4R Tau isoform expression (Yin *et al.,* 2017). In frontotemporal dementia with Parkinsonism linked to chromosome 17 (FTDP-17), mutations in the Tau gene result shifts in 3R or 4R isoform expression (Yin *et al.*, 2017). In Down Syndrome, trisomy of chromosome 21 leads to the overexpression of the kinase dual-specificity tyrosine-phosphorylated and regulated kinase 1A (Dyrk1A) (Yin *et al.,* 2017). Dyrk1A has mainly nuclear expression and has been shown to co-localize with splicing factors (Yin *et al.*, 2017). Furthermore Dyrk1A phosphorylates serine/arginine rich factor 55 (SRp55) (Yin *et al.*, 2017). SRp55 has been shown to regulate the inclusion of exon 10 (Yin *et al.*, 2012; Qian *et al.*, 2013). SRp55 promotes exon 10 inclusion and phosphorylation by Dyrk1A leads to down regulation of SRp55 activity and increased 3R-Tau expression (Yin *et al.*, 2017). Alternatively, inhibition of Dyrk1A leads to increased 4R-Tau expression (Yin *et al.*, 2017). In AD, calpain activation has been shown lead to increased Dyrk1A cleavage at the C-terminus (Jin *et al.,* 2015). This leads to increased Dyrk1A activity which is correlated with shifts in isoform expression (Jin *et al.*, 2015). During mouse development, Dyrk1A expression has been shown to decrease from postnatal day (P) 5 to P35 corresponding with a shift from 3R to 4R isoform expression (Yin *et al.*, 2017).

Dyrk1A action is not the only means by which Tau isoform expression is regulated. Transactive DNA-binding protein of 4 kDa (TDP-43) has been shown to promote exon 10 inclusion (Gu *et al.*, 2017). Interestingly, TDP-43 has been shown to aggregate in the cytoplasm of AD patients (Gu *et al.*, 2017). Unlike Dyrk1A activity,

increased TDP-43 activity leads to increased 4R isoform expression (Gu *et al.*, 2017). Shifts of to either extreme of isoform expression are detrimental for the cell and are a hallmark of disease development.

1.3.3 Post-translational Modifications of Tau

Tau is subject to a number of post-translational modifications (PTMs) including methylation, acetylation, ubiquitination, O-GlcNacylation and phosphorylation (Figure 1.10) (Morris *et al.*, 2015). Of these PTMs, phosphorylation is the most abundant though work has been done with acetylation and its role in disease state development (Cohen *et al.*, 2011; Morris *et al.*, 2015; Carlomagno *et al.*, 2017). Acetylation has been shown to inhibit Tau-microtubule interactions and promote filament formation (Cohen *et al.*, 2011). Recently, disease state acetylation of lysine 321has been shown to promote phosphorylation of serine 324 (Carlomagno *et al.*, 2017). This link between PTMs highlights the need to further study non-phosphorylation PTMs in Tau function.

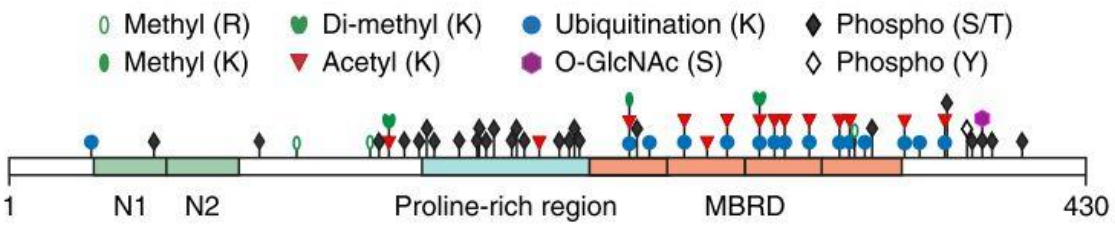

Figure 1.10 Domain structure of 4RL-Tau showing the positions of many PTMs.

Tau is an incredibly modified protein with 85 proposed or identified phosphorylation sites. Figure and legend adapted from Morris *et al.* (2015). Reprinted by permission from Copyright Clearance Center: Springer Nature, Nature Neuroscience, Tau post-translational modifications in wild-type and human amyloid precursor protein transgenic mice, Morris, M., Knudsen, G.M., Maeda, S., Trinidad, J.C., Ioanoviciu, A., Burlingame, A.L., and Mucke, L. (2015).

As the most abundant PTM, it is not surprising that Tau has 85 proposed or identified phosphorylation sites (Martin *et al.,* 2013b). Most of these sites have been identified in the disease state and cluster around the proline rich region and MBRs (Martin *et al.,* 2013b). It has been shown that phosphorylation in and around the MBR reduces Tau's affinity for the microtubule surface (Biernat *et al.,* 1993). As indicated by the large number of phosphorylation sites, Tau is phosphorylated by a number of kinases. These include the serine/threonine kinases GSK3β, CDK5, PKA and the tyrosine kinases Fyn, Lck and Abl (Martin *et al.,* 2013b).

Initially, GSK3β was thought to be Tau protein kinase 1 before Ishiguro proved that these kinases were identical (Ishiguro *et al.,* 1993). Both GSK3β and CDK5 phosphorylate Tau at many serine/threonine sites including serine 202/threonine 205 (widely known as the AT8 epitope) (Goedert *et al.,* 1995; Wada *et al.,* 1998). Disease state phosphorylation is exacerbated by the fact that phosphorylation by one kinase primes other sites (Hanger and Noble, 2011). For example, priming phosphorylation of serine 235 and serine 404 by CDK5 and other kinases, allows GSK3β to phosphorylate Tau at serine 396 and serine 400 (Hanger and Noble, 2011). PKA phosphorylation also serves to prime GSK3β sites (Hanger and Noble, 2011). PKA phosphorylation of serine 214 allows GSK3β phosphorylation of serines 175, 199, 210 and threonine 205 (Hanger and Noble, 2011). This paints a complex picture of hyperphosphorylation which requires the coordinated action of multiple misregulated kinases.

The Src family kinases have been shown to phosphorylate Tau at all five tyrosines (18, 29, 197, 310 and 394) (Lee *et al.,* 1998; Martin *et al.,* 2013b). The interactions between Tau and these kinases occur away from the microtubule surface

because Src family kinases are membrane anchored (Lee *et al.*, 1998). PXXP motifs in Tau's proline rich region, allow interactions with Src homology 3 domains (Lee *et al.*, 1998). Of the Src kinases that phosphorylate Tau, Fyn is of interest because it has been shown to predominantly phosphorylate Tau at tyrosine 18 (Y18). Both Tau and Fyn are present in the developing axon and the loss of Fyn leads to loss of axon extensions in Fyn knockout mice (Lee *et al.*, 1998). Fyn is itself subject to phosphorylation on tyrosine residues (Vacaresse *et al.*, 2008). Tyrosine phosphorylation in the C-terminal inhibits Fyn activity while auto-phosphorylation at tyrosine 416 and the action of protein tyrosine phosphatase to remove the inhibitory phosphorylation in response to external growth cues, activates the kinase and allows it to then phosphorylate Tau and other targets (Vacaresse *et al.*, 2008). Tau Y18 is phosphorylated in both the disease and non-disease states (Lee *et al.*, 1998; Martin *et al.*, 2013b) and Fyn has been shown to associate with neurofibrillary tangles in the disease state (Lee *et al.*, 2004). The case of tyrosine 18 phosphorylation is unique because of it has been shown to shield the PAD in the disease state (Kanaan *et al.*, 2012) and to potentially stabilize a non-disease sate, solution based dynamic folded conformation of Tau (Jeganathan *et al.*, 2006).

Tau regulates axonal transport in a number of ways (discussed above) including through participation in signaling cascades. Signaling cascade participation is mediated by Tau's PAD domain which has been shown to participate in the activation of GSK3β (Kanaan *et al.*, 2012). Tyrosine 18 is the last residue in the PAD and its phosphorylation prevents Tau from participating in GSK3β activation (Kanaan *et al.*, 2012). In fact, the PAD fragment has been shown to inhibit the bulk flow of cargo in the axoplasm while tyrosine 18 phosphorylated PAD did not have the same effect (Kanaan *et al.*, 2012)

highlighting a role for non-disease state phosphorylation events in the maintenance of axonal transport.

As with all phosphorylation events, Tau phosphorylation is antagonized by the action of phosphatases. These include, PP1, protein phosphatase 2A (PP2A) and protein tyrosine phosphatases (Martin *et al.*, 2013a). These phosphatases control the action of the kinases that phosphorylate Tau as well as the phosphorylation of Tau itself (Martin *et al.*, 2013a). In the disease state, phosphatase activity is greatly reduced further exacerbating the activity of the kinases which ultimately phosphorylate Tau (Martin *et al.*, 2013a).

1.3.4 Tau and Kinesin

MAP inhibition of motor motility was first demonstrated in 1989 (von Massow *et al.*, 1989). In 1991, Heins *et al.* showed that both MAP2 and Tau inhibited kinesin dependent motility (Heins *et al.*, 1991). This gave rise to a model where Tau and other MAPs act as obstacles for kinesin thereby reducing kinesin runlength (Seitz *et al.*, 2002). TIRF assays showed that this was indeed the case as both MAP2 and Tau inhibited kinesin runlength (Seitz *et al.*, 2002). These results agreed with previous work demonstrating that over expression of Tau in neuronal cell lines inhibits movement of kinesin cargo (Ebneth *et al.*, 1998). Interestingly, TIRF assays performed by Seitz *et al.* showed differences in tau isoform inhibition where 3RS-Tau was more inhibitory then 4RL-Tau (Seitz *et al.*, 2002).

Reports of MAP-motor inhibition suggested that both kinesin and dynein were inhibited by Tau (Trinczek *et al.*, 1999). However, more recent work demonstrated that both 3RS- and 4RL-Tau inhibited kinesin-1 at multiple concentrations while kinesin-2 and dynein were not affected (Dixit *et al.*, 2008; Hoeprich *et al.*, 2014). This work

showed Tau's preferential inhibition of kinesin-1 motility. TIRF assays also demonstrated Tau patch formation i.e. cooperative binding on the microtubule surface in accordance with earlier work (Ackmann *et al.*, 2000; Dixit *et al.*, 2008).

Highlighting the interconnectivity of the axonal transport system, in addition to Tau isoform differences, the microtubule lattice has been shown to affect the isoforms' ability to inhibit kinesin-1 (McVicker *et al.*, 2011). McVicker *et al.* (2011) showed that both 3RS- and 4RL-Tau inhibition of kinesin-1 motility was reduced on GMPCPP microtubules compared to paclitaxel stabilized microtubules. Additionally complicating the idea of Tau inhibition, increases in motor velocity were observed in the presence of both isoforms though kinesin-1 showed a greater increase in velocity in the presence of 4RL-Tau on paclitaxel stabilized microtubules (McVicker *et al.*, 2011). This paints a picture of Tau isoform and microtubule lattice regulation instead of straight inhibition of kinesin-1 motility.

For twenty-three years it was thought that Tau and other MAPs were immobile while bound to the microtubule (Ackmann *et al.*, 2000; Dixit *et al.*, 2008). However, further work showed that Tau is able to bind both statically and diffusively to the microtubule surface (Figure 1.11) (Hinrichs *et al.*, 2012). This study highlighted a possible mechanism by which the high concentrations of Tau found in the axon do not impede cargo delivery in non-disease state conditions. However, it did not explain the differences in Tau isoform ability to regulate kinesin-1 motility.

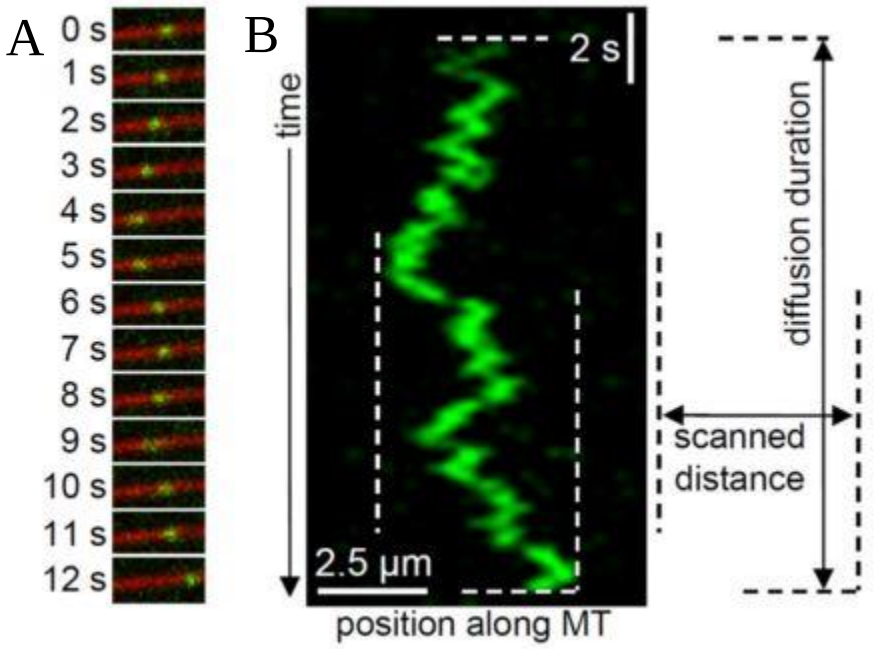

Figure 1.11 Tau diffuses along the microtubule surface.

A) Frames of a labeled 4RL-Tau molecule (green) moving along a Cy5-labeled microtubule (red) in the absence of ATP. Time intervals were as indicated. B) Kymograph showing the diffusive behavior of the event pictured in A. Figure and legend adapted from Hinrichs *et al.*, (2012) in accordance with the Creative Commons Attribution license.

Furthering the observation that Tau binds the microtubule in a static-diffusive state equilibrium, 3RS- and 4RL-Tau were observed to have different binding equilibria (McVicker *et al.*, 2014). 3RS-Tau binds more statically that 4RL-Tau on paclitaxel microtubules (McVicker *et al.*, 2014). This suggested that 3RS-Tau was more inhibitory to kinesin-1 because of its shift towards static binding. This hypothesis was further supported when both isoforms were observed to shift towards diffusive binding on GMPCPP microtubules where previous work demonstrated that Tau is less inhibitory to kinesin-1 motility (McVicker *et al.*, 2014).

While this work takes into account the nucleotide bound state of the lattice, questions remain about the involvement of lattice and Tau PTMs in the regulation of Tau behavior. Recent work has begun to answer these questions. Non-disease state phosphorylation of tyrosine 18 has been shown to regulate 3RS-Tau's binding equilibrium (Stern *et al.*, 2017). Work with acetylation demonstrated that Tau is insensitive to this microtubule PTM though it was observed to favor highly curved microtubule sections (Balabanian *et al.*, 2017).

1.3.5 Tau Structure

In 1975 when Tau was first identified, it was found to be heat stable (Weingarten *et al.*, 1975). This property surprised the authors at the time and was the first identification that Tau did not have a tertiary structure. Circular dichroism assays comparing Tau to myoglobin revealed that Tau had no significant α-helical or β-sheet structure confirming the 1975 observations (Cleveland *et al.*, 1977). Almost upon discovery, the challenge to understand Tau structure was made apparent.

By 1988, neuronal microtubules had been observed to have crosslinks comprised of MAP1 and MAP2 but the structure of Tau remained unknown though its role in the disease state was firmly established (Hirokawa *et al.*, 1988). Deep-etch cryo-EM studies showed that a portion of the Tau molecule extends away from the microtubule surface (Hirokawa *et al.*, 1988). Other cryo-EM studies that did not rely on pelleting, showed that Tau bound to microtubules results in a 'fuzzy' microtubule coating (Al-Bassam *et al.*, 2002; Santarella *et al.*, 2004). These studies used helical reconstruction and Tau labeling techniques to determine that Tau binds along protofilament ridges potentially with binding sites at the α-tubulin subunits (Al-Bassam *et al.*, 2002; Santarella *et al.*, 2004). Current work by the Nogales group, refines previous cryo-EM work confirming Tau binding on microtubule protofilaments with microtubule binding repeats binding in tandem (Kellogg *et al.*, 2018). This binding occurs along tubulin heterodimers (Kellogg *et al.*, 2018) and explains Tau's ability to regulate microtubule dynamics by crosslinking dimers. Together, these studies elucidate Tau structure though none of these studies account for the dynamic structural changes which the 'fuzzy' microtubule coat indicates.

In addition to the investigation of Tau's bound structure, solution based study of Tau confirmation using NMR, bulk FRET and single molecule FRET studies, show that Tau has a dynamic folded confirmation (Figure 1.12) (Jeganathan *et al.*, 2006; Elbaum-Garfinkle and Rhoades, 2012). These two studies differ in their placement of the N- and C-termini relative to the MBRs though they both agree in the folded nature of Tau in solution (Figure 1.12) (Jeganathan *et al.*, 2006). Further work with disease state phosphorylation events showed compaction of Tau's solution based folded confirmation (Jeganathan *et al.*, 2008).

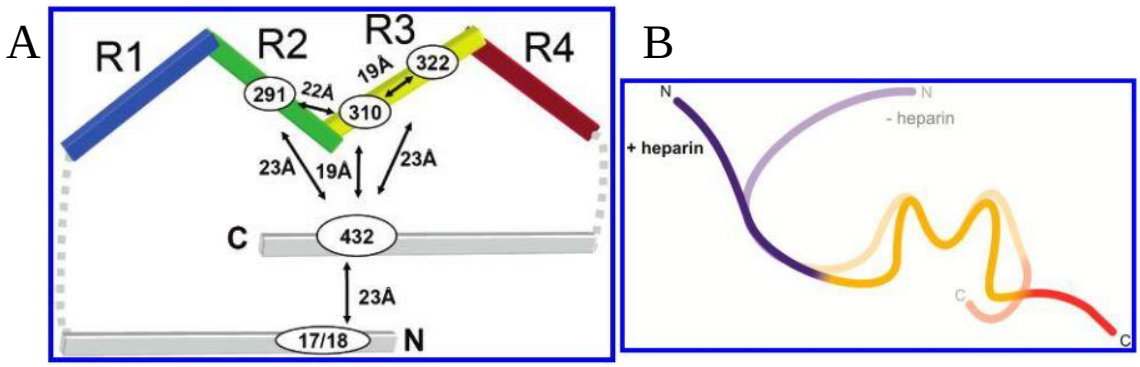

Figure 1.12 Structures of Tau in solution.

Tau has been shown to have a dynamic folded conformation in solution. A) NMR and bulk FRET studies were used to generate this paperclip-like folded conformation where the C-terminal interacts with the microtubule binding repeats and the N-terminal. The overall conformation is stabilized by interactions between the N- and C-termini. Figure and legend reprinted with permission from Jeganathan, S., von Bergen, M., Brutlach, H., Steinhoff, H.J., and Mandelkow, E. (2006). Global hairpin folding of tau in solution. Biochemistry *45*, 2283-2293. Copyright (2006) American Chemical Society. B) Single molecule solution based FRET was used to generate this conformation of Tau in the absence of heparin (watermark) where both the N- and C-termini interact with the microtubule binding repeats to stabilize this folded conformation. In the presence of heparin, which promotes Tau aggregation, these interactions are greatly reduced. Figure and legend reprinted with permission from Elbaum-Garfinkle, S., and Rhoades, E. (2012). Identification of an aggregation-prone structure of tau. J. Am. Chem. Soc. *134*, 16607-16613. Copyright (2012) American Chemical Society.

The studies of Tau structure to date, have elucidated our understanding of Tau structure both on and off the microtubule surface. However, many questions remain including whether structural changes on the microtubule surface underlie Tau's binding behavior and ability to inhibit kinesin-1 motility. The work presented in this dissertation represents a first attempt at linking Tau structural change to its behavior on the microtubule surface and regulation of motor motility.

1.4 Purpose and Scope

One hundred and twelve years have passed since Santiago Ramón y Cajal gave his acceptance speech in 1906. Over that time, the field has progressed in its understanding of the neuron and the processes that ensure neuronal function. Despite the strides that have been made, many questions remain open. One of the most basic and fascinating, is the means by which cellular material manufactured in the cell body is moved throughout the axon. This processes of axonal transport is a complex system of motors, microtubule tracks and regulators that in the largest axon can stretch up to 2 meters (Britannica, 2018). During axonal development and throughout the life of the cell, Tau plays an integral role in the regulation of this system (Figure 1.13). As described in the preceding text, the signaling pathways that regulate axonal development and function converge on the cytoskeletal elements involved in axonal transport. The regulation of axonal transport is complex involving inter-play between the tracks, the motors and the microtubule associated proteins. Of the microtubule associated proteins, Tau has been extensively studied because of its involvement in transport regulation (Figure 1.13) throughout the life of the cell and in disease development.

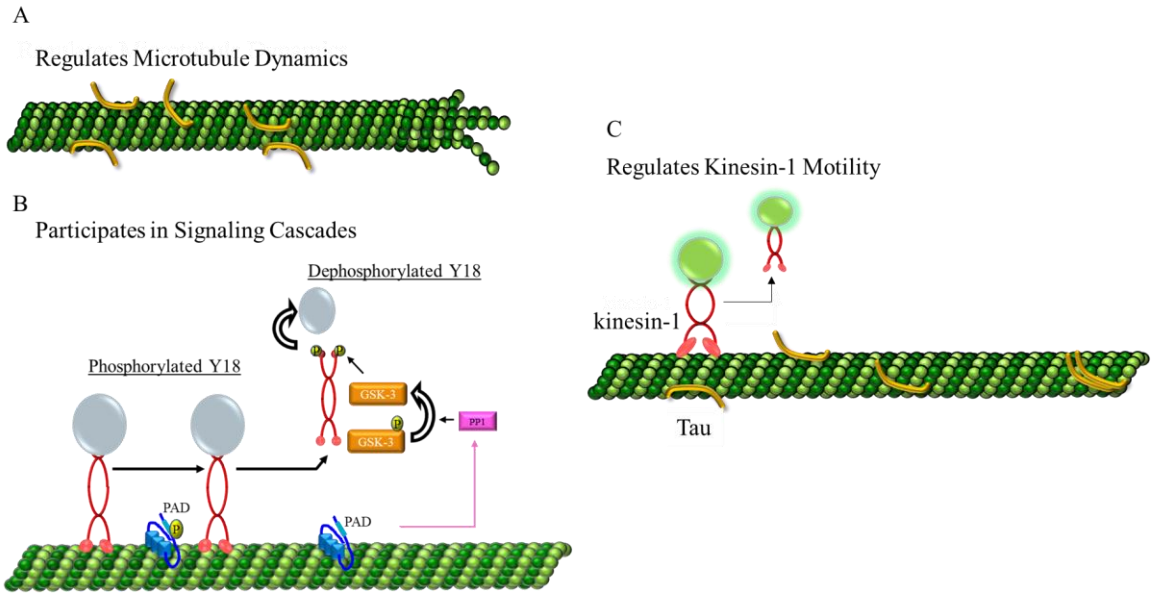

Figure 1.13: Tau Functions in Axonal Transport

Tau has been shown to regulate axonal transport in a number of ways. A) Tau isoforms differentially regulate microtubule growth and shortening (Panda *et al.*, 2003). B) Tau has also been shown to participate in signaling cascades. The PAD has been shown to activate PP1 which in turn activates GSK3β. Activation of GSK3β, leads to the phosphorylation of kinesin-1 light chains and the release of cargo (Morfini *et al.*, 2002; LaPointe *et al.*, 2009). The PAD is shielded by tyrosine 18 (Y18) phosphorylation (Kanaan *et al.*, 2012). In the disease state, PAD shielding by Y18 phosphorylation prevents inhibition of axonal transport. C) Tau has been shown to preferentially inhibit kinesin-1 motility *in vitro* (Dixit *et al.*, 2008). This inhibition does not disrupt cargo transport *in vivo* and raises the question of whether Tau is regulated on the microtubule and how this regulation affects motor motility. The work presented here focusses on cellular regulation of Tau's structure and function by phosphorylation and the role this may play in motor motility regulation.

Since Tau was identified as a regulator of kinesin-1 motility (Heins *et al.*, 1991), efforts have been made to understand the means by which this regulation occurs and how the cell controls this regulation (Ebneth *et al.*, 1998; Trinczek *et al.*, 1999; Seitz *et al.*, 2002). Counterintuitively, though Tau has been shown to inhibit kinesin-1 motility *in vitro* in a concentration dependent manner (Dixit *et al.*, 2008), cargo transport is not inhibited by the high concentration of Tau (2-5 μM) found in the axon (Morfini *et al.*, 2007; Avila, 2010). This apparent disagreement between *in vitro* and *in vivo* observations raises the question of how the cell regulates motor motility inhibition to allow for cargo delivery in non-disease state conditions. In partial answer to this question, Tau has been shown to bind the microtubule in a static-diffusive state equilibrium, which differs with isoform and lattice, and corresponds with isoform ability to inhibit kinesin-1 motility (Dixit *et al.*, 2008; McVicker *et al.*, 2011; Hinrichs *et al.*, 2012; McVicker *et al.*, 2014). These studies do not explain the purpose of the static-diffusive state binding equilibrium and do not show how this equilibrium is regulated. The work presented here aims to fill this gap in our knowledge so that we can begin to understand how regulation of Tau's static-diffusive state equilibrium allows for cellular regulation of axonal transport.

In vitro work studying Tau microtubule binding behavior and motor motility inhibition uses recombinant human Tau expressed in bacterial systems (Dixit *et al.*, 2008; McVicker *et al.*, 2014). This method of expression does not allow Tau to be post-translationally modified as it would be within the cell. Tau is subject to an incredible number of post-translational modifications including 85 proposed or identified phosphorylation events (Martin *et al.*, 2013b). It is therefore not inconceivable that

phosphorylation may play a role in the regulation of Tau function. In fact, it has been shown that phosphorylation of tyrosine 18 prevents Tau disease state inhibition of axonal transport (Kanaan *et al.*, 2012). These results made tyrosine 18 an interesting target to explore in the regulation of Tau behavior on the microtubule surface. In chapter two, we address the question of how tyrosine 18 phosphorylation affects Tau's ability to inhibit kinesin-1 motility. We demonstrate that phospho-mimetics of tyrosine 18 in 3RS-Tau exhibit a shift in static-diffusive state equilibrium towards the diffusive state, correlating with a reduction in inhibition of kinesin-1 motility. We further demonstrate that the static-diffusive state binding equilibrium is maintained *ex vivo*, as is the phosphorylation mediated diffusive state shift. This work represents the first demonstration of a means by which the cell can regulate Tau's binding equilibrium. Furthermore, this is the first evidence that Tau's static-diffusive state equilibrium is maintained under physiological conditions highlighting a role for static and diffusive binding in Tau's cellular function.

While chapter 2 highlights the importance of regulating Tau's binding equilibrium, it also raises more questions about microtubule bound Tau. Tyrosine 18 phosphorylation is an N-terminal modification. The N-terminal of Tau does not interact with the microtubule surface (Goode *et al.*, 2000), however, our results from chapter 2 demonstrate that phosphorylation of tyrosine 18 affects Tau binding behavior. This indicates that tyrosine 18 phosphorylation potentially affects Tau binding through long range structural change. Interestingly, in addition to regulating Tau's static-diffusive state equilibrium, tyrosine 18 has been implicated in the stabilization of a solution based dynamic folded conformation of Tau (Jeganathan *et al.*, 2006).

Admittedly, studying Tau's conformation is challenging because it has no tertiary structure (Cleveland *et al.*, 1977). Solution based structural studies have shown that Tau has a dynamic folded conformation (Jeganathan *et al.*, 2006; Elbaum-Garfinkle and Rhoades, 2012). However, these techniques have not been used to identify dynamic structural changes on the microtubule surface. Cryo-EM studies have attempted to visualize microtubule bound Tau and while they have had success resolving portions of the protein, they cannot be used to study dynamic structural changes (Hirokawa *et al.*, 1988; Al-Bassam *et al.*, 2002; Santarella *et al.*, 2004; Kadavath *et al.*, 2015; Kellogg *et al.*, 2018). The 'fuzzy' Tau coated microtubules that have been seen with cryo-EM do however support the idea of dynamic structural change (Al-Bassam *et al.*, 2002; Santarella *et al.*, 2004). Recent cryo-EM work has been able to show the interactions of microtubules with microtubule binding repeats while Tau is bound statically (Kellogg *et al.*, 2018). These structures have higher resolution than previous work and confirm that in the static state Tau binds along the protofilament with fully extended microtubule binding repeats (Kellogg *et al.*, 2018). While this study does not resolve Tau's N- and C-termini or the microtubule binding repeats in the diffusive state, it give us questions for future study.

In chapter 3, we hypothesize that distinct structural changes underlie static versus diffusive binding. Instead of solution or cyro-EM based studies, we use a three color single molecule fluorescence resonance energy transfer assay imaging with total internal reflection fluorescence microscopy and alternating laser excitation (ALEX) to show that in the static state the N- and C- termini of Tau interact more closely than in the diffusive state. Our assay allows us to observe dynamic structural changes while Tau is bound to

the microtubule. The results indicate that there are indeed distinct structural changes that underlie Tau's binding equilibrium. Prior to this work, no studies have been done to elucidate what structural changes underlie the static-diffusive binding equilibrium and therefore Tau's behavior and function on the microtubule surface.

Taken together, these studies demonstrate the link between structure and function of Tau and the cellular means by which Tau behavior and function can be regulated. While we have begun to address the link between Tau structure and function on the microtubule surface, this work also points to new questions that must be answered. In chapter 4, I outline our work in the context of the field and provide directions that the techniques we have developed now allow us to take.

CHAPTER 2: PHOSPHO-REGULATION OF TAU MODULATES KINESIN-1 MOTILITY

2.1 Abstract

Microtubule-based axonal transport is tightly regulated by numerous pathways ensuring appropriate delivery of specific organelle cargoes to selected subcellular domains. Highlighting the importance of this process, pathological evidence has linked alterations in these pathways to the pathogenesis of several neurodegenerative diseases. An important regulator of this system, the microtubule associated protein Tau has been shown to participate in signaling cascades, modulate microtubule dynamics and preferentially inhibit kinesin-1 motility. However the cellular means of regulating Tau's inhibition of kinesin-1 motility remains unknown. Tau is subject to various post-translational modifications including phosphorylation, but whether phosphorylation regulates Tau on the microtubule surface has not been addressed. It has been shown that tyrosine 18 phosphorylated Tau regulates inhibition of axonal transport in the disease state. Tyrosine 18 is both a disease and non-disease state modification and is therefore an attractive starting point for understanding control of Tau's inhibition of kinesin-1 motility. We show that pseudophosphorylation of tyrosine 18 reduces 3RS-Tau's inhibition of kinesin-1 motility. Additionally, we show that introduction of negative charge at tyrosine 18 shifts Tau's previously described static-dynamic state binding equilibrium towards the dynamic state. We also present the first evidence of the establishment of Tau's static-dynamic state equilibrium under physiological conditions.

2.2 Introduction

The neuronal microtubule associated protein (MAP) Tau is involved in axonal development from its earliest stages onwards (Andreadis, 2005). Tau has been implicated in many processes within the neuron, the majority of which are associated with its participation in axonal transport (AT). The AT system encompasses the microtubule track, molecular motors including kinesin-1 and -2, numerous MAPs including Tau, and many signaling cascades (Maday *et al.*, 2014). Tau's role in AT is multi-faceted, as it has been shown to stabilize microtubules (Panda *et al.*, 2003), participate in signaling cascades (Kanaan *et al.*, 2012) and inhibit kinesin-1 motility (Vershinin *et al.*, 2007; Dixit *et al.*, 2008; McVicker *et al.*, 2011). In the non-disease state Tau's ability to preferentially inhibit kinesin-1 motility is of particular interest when juxtaposed with the failure of this inhibition to disrupt normal cargo delivery, suggesting that Tau has a role in the modulation of kinesin-mediated cargo delivery during AT (Kanaan *et al.*, 2012). This highlights the importance of cellular regulation of Tau's inhibitory function of kinesin-1 transport during AT, but how this control is achieved is currently unknown.

Understanding Tau's function and corresponding regulation is compounded by its sequence diversity. There are six Tau isoforms which arise from strict developmental regulation of the alternative splicing of the *MAPT* gene on chromosome 17 (Andreadis, 2005; Ballatore *et al.*, 2007). While all six isoforms have a central proline rich region (PRR) and N-terminal phosphatase activating domain (PAD) (Ballatore *et al.*, 2007; Kanaan *et al.*, 2012), they differ by number of C-terminal microtubule binding repeats (three – four) and N-terminal acidic inserts (zero – two) (Goode *et al.*, 2000; Ballatore *et al.*, 2007). Tau's role in signaling is partly mediated by its PAD which has been shown to

activate protein phosphatase 1 (PP1) (LaPointe *et al.*, 2009; Kanaan *et al.*, 2011). In the disease state, a phospho-mimetic of tyrosine 18 (Y18), the last residue in the PAD, has been shown to prevent the inhibition of axonal transport when incorporated into neurofibrillary tangles (Kanaan *et al.*, 2012). Y18 is predominantly phosphorylated by the Src family kinase Fyn in both the disease and non-disease states (Lee *et al.*, 1998; Kanaan *et al.*, 2012; Larson *et al.*, 2012).

Adding to this isoform diversity, it has recently been shown that Tau can bind the microtubule in an equilibrium between static and ATP-independent dynamic states (Vershinin *et al.*, 2007; Dixit *et al.*, 2008; Hinrichs *et al.*, 2012). We have shown that the static-dynamic state equilibrium differs with Tau isoform and microtubule lattice structure with the shortest isoform, 3RS-Tau, being more static on paclitaxel stabilized microtubules than the longest isoform, 4RL-Tau (McVicker *et al.*, 2014). Tau's ability to inhibit kinesin-1 motility also differs with isoform. 3RS-Tau, which favors the static state, is more inhibitory to kinesin-1 than 4RL-Tau (Dixit *et al.*, 2008; McVicker *et al.*, 2011). This correlation indicates that the static state is more inhibitory to kinesin-1 motility than the dynamic state. Given these isoform-specific differences in behavior, a common mechanism for regulating multiple Tau isoforms and their static-dynamic state equilibria remains unclear.

All isoforms of Tau are subject to a variety of post-translational modifications (Watanabe *et al.*, 1993; Funk *et al.*, 2014; Kamah *et al.*, 2014) which may have important roles in many aspects of Tau regulation. We postulate that post-translational modifications (especially phosphorylation) are the link between controlling Tau's static-dynamic equilibrium and Tau's inhibition of kinesin-1 motility. As stated above, static

Tau is more inhibitory to kinesin-1 motility than dynamic Tau (McVicker *et al.*, 2011) while phosphorylation/a phospho-mimetic of Y18 has been shown to prevent inhibition of axonal transport in the disease state (Kanaan *et al.*, 2012). We hypothesize that the negative charge provided by phosphorylation of Y18 stabilizes the dynamic state/destabilizes the static state thereby shifting the static-dynamic equilibrium towards the less inhibitory dynamic state. To test this hypothesis, we generated phospho-mimetic and control 3RS-Tau constructs by mutating Y18 to glutamic acid (Y18E 3RS-Tau) and alanine (Y18A 3RS-Tau). To study the effect of increasing the negative charge at/around Y18, a double phospho-mimetic was generated by mutating threonine 17 and Y18 to glutamic acid (dE 3RS-Tau). Using total internal reflection fluorescence (TIRF) microscopy, we observed single molecule 3RS-Tau interactions with paclitaxel stabilized microtubules. Our results provide the first evidence for direct control by phosphorylation of Tau's dynamic behavior, and therefore its function, on the microtubule surface.

2.3 Results

Introduction of negative charge at Y18 reduces 3RS-Tau inhibition of kinesin-1 motility. TIRF microscopy was used to visualize kinesin-1 motility (Figure 2.1) on paclitaxel stabilized microtubules in the presence of 200 nM unlabeled and Alexa 488 labeled WT and Y18E 3RS-Tau (1:5; Tau:tubulin) (Figure 2.2A). In the absence of Tau, kinesin-1 had a run length of 1.64 $\pm$ 0.50 µm (Figure 2.2B) which was significantly decreased in the presence of both unlabeled and labeled WT 3RS-Tau (0.99 $\pm$ 0.23 µm and 0.99 $\pm$ 0.24 µm; Figure 2.2, C and D; Supplemental Table S2.2; Supplemental Figure S2.1) as we have previously demonstrated (McVicker *et al.*, 2011). Interestingly however, kinesin-1's run length significantly increased in the presence of Y18E 3RS-Tau

(unlabeled = 1.37 ± 0.39 µm, labeled = 1.35 ± 0.39 µm; Figure 2.2, E and F) compared to the WT 3RS-Tau condition (Figure 2.2, C and D). Kinesin-1's velocity did not differ under any of the conditions tested (Supplemental Table S2). These results indicate that introduction of negative charge at Y18 reduces 3RS-Tau's inhibition of kinesin-1 run length without affecting its velocity. WT Tau's ability to inhibit kinesin-1 run length without affecting velocity has been reported previously (Dixit *et al.*, 2008). This is the first evidence for phosphorylation mediated regulation of 3RS-Tau's ability to inhibit kinesin-1 motility.

A Y18 phospho-mimetic of 3RS-Tau exhibits a significant shift towards the dynamic state in vitro. Given the results of our motility assays, we wanted to know if the introduction of negative charge at Y18 affects Tau's static-dynamic equilibrium on the microtubule surface. TIRF microscopy was used to visualize the interactions of the constructs used in the motility assays (WT and Y18E 3RS-Tau) (Figure 2.3A) with TRITC rhodamine labeled paclitaxel stabilized microtubules at 200 nM Tau (1:5, Tau:tubulin). We observed predominantly static events for WT 3RS-Tau (77.1 ± 4.2 %, Figure 2.3B; Supplemental Table S2.3), a result which we have previously demonstrated (McVicker *et al.*, 2014). Conversely, we observed a significant decrease ($p < 0.05$) in the number of static events for Y18E 3RS-Tau (47.7 ± 5.0 %, Figure 2.3B; Supplemental Table S2.3).

Static dwell times for WT 3RS-Tau were best fit to a two phase exponential function. This revealed one population of long dwell times and one of short dwell times (Supplemental Figures S2.2A and S2.3; Supplemental Table S2.3), most likely corresponding to the small multi-protein complexes (long dwell times) and single molecule interactions (short dwell times) with the microtubule surface that we have

previously observed in the static state (McVicker *et al.*, 2014). Y18E 3RS-Tau static dwell times were best fit to a one phase exponential function (Supplemental Figure S2.2B and S2.3; Supplemental Table S2.3) with an average of 14.5 s which is comparable to WT 3RS-Tau's long static dwell time of 15.7 s. Dynamic dwell times for both WT and Y18E 3RS-Tau were best fit to one phase exponential functions (Supplemental Figure S2.2C and D; Supplemental Figure S2.3; Supplemental Table S2.3) and did not differ from each other. The ability to control the equilibrium between the static and dynamic states of Tau, and to specifically regulate that control by mimicking phosphorylation at Y18, has not been previously demonstrated.

Phospho-mimetic constructs of Y18 3RS-Tau bind with decreased affinity for the microtubule. Given the observed shift towards the dynamic state we considered the possibility that the introduction of negative charge at Y18 reduced Tau's affinity for the microtubule surface. This would also lead to a decrease in 3RS-Tau's ability to inhibit kinesin-1 motility. To address this, TIRF microscopy was used to image increasing concentrations (50-650 nM) of Alexa 532 labeled 3RS-Tau binding to HiLyte 488 labeled, paclitaxel stabilized microtubules (Figure 2.4A). An unphosphorylatable construct (Y18A 3RS-Tau) and a construct with increased negative charge (dE 3RS-Tau) were observed alongside WT and Y18E 3RS-Tau in an effort to better understand the effect of the introduction of negative charge. The average intensity of Alexa 532 labeled 3RS-Tau per unit length along the microtubule was measured and plotted against Tau concentration. The plots were then fit to one site-specific binding curves from which the K_D was determined. We found that WT 3RS-Tau binds the microtubule with a K_D of 150 ± 126 nM while Y18A 3RS-Tau had a K_D of 331 ± 100 nM (Figure 2.4B; Supplemental

Table S2.3). Introduction of increasing negative charge decreased the affinity of Tau for the microtubule as evidenced by a K_D of 700 ± 318 nM for Y18E 3RS-Tau with an even greater decrease for dE 3RS-Tau (K_D of 902 ± 266 nM) (Figure 2.4B; Supplemental Table S3).

Phospho-mimetic mediated shift towards the dynamic state is maintained for comparable bound fractions of 3RS-Tau. Using the K_D values from our binding assays, we determined that at a microtubule concentration of 1 uM, WT 3RS-Tau had a bound fraction of 87% while Y18E 3RS-Tau's bound fraction was 59%. At the high concentration used in our kinesin-1 motility assays (200 nM; 1:5 (Tau:tubulin)), WT 3RS-Tau would have a microtubule bound concentration of 174 nM while Y18E 3RS-Tau would have 118 nM bound. The inhibition of kinesin-1 by Y18E 3RS-Tau that we observed for this high concentration could then be attributed to this difference in bound fraction of Tau. To address this possibility, we observed WT, control (Y18A) and phospho-mimetic (Y18E, dE) constructs of 3RS-Tau at 10 nM (1:3000; Tau:tubulin) where the bound concentrations of WT (9 nM), Y18A (7 nM), Y18E (7 nM) and dE (5 nM) 3RS-Tau were comparable. At this concentration, the percentage of static events for Y18A (77.8 ± 4.2%) was not significantly different from WT 3RS-Tau (81.4 ± 3.9%) (Figure 2.5; Supplemental Table S2.3). Under these conditions Y18E 3RS-Tau had a static population of 67.4 ± 4.7% (Figure 2.5; Supplemental Table S2.3) which was a statistically significant difference from WT 3RS-Tau ($p < 0.05$) and Y18A 3RS-Tau ($p < 0.05$) (Figure 2.5; Supplemental Table S2.3). dE 3RS-Tau had a static population of 51.4 ± 5.0% (Figure 2.5; Supplemental Table S2.3) which was a statistically significant decrease compared to Y18E 3RS-Tau ($p < 0.05$).

Dynamic state dwell times for WT, Y18A, Y18E and dE 3RS-Tau (Supplemental Figure S2.4, A-D; Supplemental Table S2.3), were best fit to one phase exponential functions and did not significantly differ. Dwell times for static events from WT, Y18A, Y18E and dE 3RS-Tau populations were best fit to two phase exponential functions (Supplemental Figure S2.5, A-D). Though there was a slight decrease in the long and short dwell times for Y18E 3RS-Tau (Supplemental Figure S2.5C; Supplemental Table S2.3) and an increase in the short dwell time for dE 3RS-Tau (Supplemental Figure S2.5D; Supplemental Table S2.3); the WT, Y18A and dE 3RS-Tau dwell times (long) were not appreciably different. This result indicates that the observed shift towards the dynamic state is independent of the fraction of Tau bound to the microtubule.

Negative charge mediated shift towards the dynamic state is maintained ex vivo. All the *in vitro* assays presented here were performed at low ionic strength. We therefore asked if the effect of negative charge on 3RS-Tau's behavior was still present under more physiologically relevant conditions. TIRF microscopy was used to visualize Tau behavior (Figure 2.6) in *ex vivo* preparations of axoplasm extruded from the giant axons of Atlantic squid (*Loligo pealei*). The extruded axoplasm samples were perfused with a mixture of Alexa 568 labeled WT, Y18A or Y18E 3RS-Tau to visualize microtubules and Alexa 488 labeled WT, Y18A or Y18E 3RS-Tau to observe single molecule events (Supplemental Movie S2.4 and S2.5). Non-phosphorylatable Y18A 3RS-Tau had a static population of 82.0 ± 3.8 % (Figure 2.7; Supplemental Table S2.3). This was statistically significant from static populations for WT (74.0 ± 4.4 %) and Y18E 3RS-Tau (73.2 ± 4.4 %) ($p < 0.05$) (Figure 2.7; Supplemental Table S2.3). These results highlight the importance of using an unphosphorylatable construct to prevent possible *ex vivo*

phosphorylation at Y18. Based on this data we conclude that the Y18E mediated shift towards the dynamic state observed *in vitro* is maintained within the axoplasm. Unlike the *in vitro* dwell times, all *ex vivo* dwell times for WT, Y18A and Y18E 3RS-Tau best fit a single exponential function. There was no difference in the *ex vivo* static dwell times (Supplemental Figure S2.6, A-F; Supplemental Table S2.3) for WT, Y18A and Y18E 3RS-Tau. We observed *ex vivo* dwell times which were an order of magnitude shorter than the *in vitro* dwell times (Supplemental Figures S2.2, S2.4 and S2.5). This difference has been previously observed (Janning *et al.*, 2014) and can most likely be attributed to the increased ionic strength found under physiological conditions. This is the first evidence demonstrating that the static-dynamic equilibrium of Tau on the microtubule surface observed *in vitro* is present under conditions found within the axon.

2.4 Discussion

Recently, we have shown that Tau's established ability to inhibit kinesin-1 motility differs with isoform (McVicker *et al.*, 2014). However, the cellular means of regulating Tau's inhibition of kinesin-1 is still not understood. Y18 phosphorylation is of particular interest because of its role in preventing the inhibition of axonal transport in the disease state (Kanaan *et al.*, 2012) and its possible involvement in stabilizing a non-disease state dynamic folded conformation of Tau in solution (Jeganathan *et al.*, 2006). Our results (Figure 2.2) are the first evidence of phosphorylation regulating Tau's ability to inhibit kinesin-1.

We hypothesized two possible explanations for the reduced inhibition of kinesin-1. Introduction of negative charge at Y18 could shift the static-dynamic state equilibrium towards the less inhibitory dynamic state. Alternatively, the negative charge at Y18 could

decrease Tau's affinity for the microtubule surface, effectively reducing the number of Tau obstacles for kinesin-1 to circumnavigate. Specifically for our kinesin-1 motility assay conditions (1:5, Tau:tubulin) (Figure 2.2), a final concentration of 200 nM Tau was used for which WT 3RS-Tau had a fraction bound of 87% (174 nM) compared to Y18E 3RS-Tau's fraction bound of 59% (118 nM) (based on binding assay results; Figure 2.4). But we also found that Y18E 3RS-Tau's shift towards the dynamic state is maintained at comparable fractions of Tau bound to the microtubule surface (5-9 nM) (Figure 2.5). Therefore, the dynamic state shift observed upon Y18 phosphorylation is intrinsic to behavior of individual Tau molecules and not dependent on amount of Tau bound to the microtubule.

However, the difference in affinity for the microtubule between WT and Y18E 3RS-Tau must still be taken into account. Though the exact structural changes that underlie static vs dynamic binding are not well understood, the negative charge mediated decrease in affinity indicates that long range structural interactions may affect protein binding and behavior. Based on the behavior observed in the high concentration dynamics assays (Figure 2.3), 134 nM of the bound WT 3RS-Tau would be static while for Y18E 3RS-Tau 56 nM would be static. For 1 μM of microtubules, statically bound WT 3RS-Tau would occupy 13% of the available kinesin-1 binding sites while static Y18E 3RS-Tau would occupy 5% of the available binding sites. This indicates that Y18E 3RS-Tau's decreased inhibition of kinesin-1 is due to *a combination of* a decreased bound fraction and an equilibrium shift towards the dynamic state. Ultimately this leads to a reduction in the number of static Tau obstacles that kinesin-1 encounters on the microtubule surface.

It has previously been demonstrated that with increasing concentration Tau forms multi-protein patches on the microtubule surface (Dixit *et al.*, 2008). Our high concentration behavioral assays (Figure 2.3, Supplemental Table S2.3) show two populations of WT 3RS-Tau static dwell times. The long dwell time (Supplemental Table S2.3, Supplemental Figures S2.2 and S2.3) may be indicative of multi-protein complexes formed by N-terminal region mediated Tau-Tau interactions (Feinstein *et al.*, 2016). The loss of a short static dwell time for Y18E 3RS-Tau (Supplemental Table S2.3, Supplemental Figure S2.2) indicates that with the introduction of negative charge at high concentration, static binding may only occur when multi-protein complexes are formed. Additionally, the introduction of N-terminal negative charge may disrupt complex formation (Feinstein *et al.*, 2016) which would lead to the observed shift towards dynamic binding at high concentration (Supplemental Table S2.3). In keeping with these results we have previously shown that 4RL-Tau which has two acidic N-terminal inserts, forms smaller multi-protein complexes and is more shifted towards dynamic binding than 3RS-Tau which has no acidic inserts (McVicker *et al.*, 2014). At low concentration (Figure 2.3), static binding is not governed by concentration driven complex formation.

Tau's inhibition of kinesin-1 motility does not impact velocity (Supplemental Table S2.2) (Dixit *et al.*, 2008). We have previously demonstrated that while kinesin-1 pauses both in the presence and absence of Tau the pause-step frequency does not change (Hoeprich *et al.*, 2014). Therefore, the effect of pausing on velocity is not significant. An increase in run termination would lead to the observed decrease in run length.

We have previously reported the importance of the lattice structure in regulation of Tau isoforms' static-dynamic state equilibria (McVicker *et al.*, 2014). Tau's ability to

inhibit kinesin-1 motility is also regulated by lattice structure (McVicker *et al.*, 2011). On GMPCPP stabilized microtubules, 3RS-Tau binds dynamically and does not inhibit kinesin-1 motility (McVicker *et al.*, 2011; McVicker *et al.*, 2014). Tau's inhibitory effect is restored on paclitaxel stabilized microtubules where 3RS-Tau's binding equilibrium is shifted towards the static state (McVicker *et al.*, 2011; McVicker *et al.*, 2014). The present study demonstrates that lattice regulation is not the only means available for control of Tau's binding equilibrium. Controlling Tau's intrinsic equilibrium through phosphorylation and the microtubule lattice structure through nucleotide binding states and PTMs (McVicker *et al.*, 2014; Yu *et al.*, 2015) gives the cell greater flexibility in regulating Tau obstacles and allows for continued AT. We have demonstrated that Tau's static-dynamic state equilibrium is maintained under physiological conditions and that the shift towards the dynamic state that we observed *in vitro* occurs *ex vivo* (Figure 2.5). As we have shown and has been previously reported (Janning *et al.*, 2014), Tau binds both dynamically and transiently to the microtubule surface under physiological conditions. Extending this observation, we emphasize the importance of regulating these dynamic interactions to control Tau function. It should be noted that the dwell times reported here are longer than those previously reported (Janning *et al.*, 2014), which may relate to the different Tau constructs and neuronal systems used, and highlight the importance of further study to better understand Tau dynamics *in vivo*.

Within the axon phosphorylation of Y18, the last residue of the PAD, not only shields the PAD (Kanaan *et al.*, 2012), but as our results show, the negative charge provided by phosphorylation facilitates a dynamic state shift independent of fraction bound (Figures 2.3 and 2.5). This gives the cell two levels of regulating Tau's function by

preventing Tau signaling through the PAD and Tau's physical inhibition of kinesin-1 motility. In this model while Y18 is phosphorylated, individual motors continue to transport cargo (Figure 2.8). Dephosphorylation of Y18 leads to signaling activation (Kanaan *et al.*, 2012) and increased physical inhibition of kinesin-1 motility (Figure 2.8). Exposure of Tau's PAD has been shown to ultimately activate glycogen synthase kinase 3β (GSK-3β) which in addition to phosphorylating Tau (Lovestone *et al.*, 1996; Martin *et al.*, 2013b) can phosphorylate kinesin light chains (Morfini *et al.*, 2002) (Figure 2.8). This leads to further disruption of cargo-motor interactions leading to the dissociation of motors from cargo, thereby allowing cargo delivery (Morfini *et al.*, 2002) (Figure 2.8).

PAD shielding by phosphorylation of Y18 (Kanaan *et al.*, 2012) may partly depend on structural change. The misregulation of Tau's structure (Elbaum-Garfinkle and Rhoades, 2012) and therefore its function could be a common pathway by which neurodegeneration occurs in diseases where shifts in isoform expression and aberrant phosphorylation lead to the same outcome (Qian *et al.*, 2013; Gerson *et al.*, 2014).

Control of Tau's function is further complicated by abnormal modifications which occur in the disease state (Morris *et al.*, 2015). Our group and others have previously shown that Tau's ability to inhibit kinesin-1 motility differs with isoform (Vershinin *et al.*, 2007; Dixit *et al.*, 2008; McVicker *et al.*, 2011) as does the static-dynamic state equilibrium (McVicker *et al.*, 2014). The results we present here indicate that phosphorylation provides a common means of regulating the isoforms and their equilibria. Perturbing the equilibrium between the static and dynamic states would lead to disruption of cargo transport within the axon by disrupting inhibition of kinesin-1 motility and release of cargo. Given our results, it is highly likely that the equilibrium

between the static and dynamic states is spatially regulated in order to effectively control local cargo delivery. This localized signaling would require the involvement of multiple signaling pathways and a complex pattern of Tau phosphorylation. To date, it is not known how these phosphorylation events affect the normal behavior of the protein or how the cell balances N- and C-terminal phosphorylation to maintain a working static-dynamic state equilibrium. In addition to phosphorylation, Tau is subject to acetylation (Kamah *et al.*, 2014) and methylation (Funk *et al.*, 2014), whose purposes in the regulation of Tau's function have yet to be fully understood. It is imperative that the balance of non-disease state modifications, especially phosphorylation, is understood given that one of the first steps in neurodegeneration may be disruption of these normal modifications. We have begun to elucidate the importance of regulating phosphorylation at specific sites to control Tau function. Here we have highlighted new implications for the cellular control of Tau's static-dynamic state equilibrium in axonal transport under both normal and disease state conditions.

2.5 Materials and Methods

All protein work and experiments were done in BRB80 (80 mM PIPES, 1 mM EGTA, 1 mM $MgCl_2$, pH 6.9 at room temperature) unless otherwise noted.

Tau Mutant Generation, Purification and Labeling Alanine/glutamic acid 3RS-Tau constructs were generated using the QuikChange II XL Site-Directed Mutagenesis Kit (Agilent Technologies, Santa Clara, CA). Constructs were then expressed in BL21-CodonPlus(DE3)-RP *Escherichia coli* cells (Stratagene, La Jolla, CA) and purified using Q and SP Sepharose (Sigma-Aldrich, St. Lois, MO) affinity column chromatography (McVicker *et al.*, 2011; McVicker *et al.*, 2014). Following purification, samples were

dialyzed against BRB80 and protein concentrations were determined with the bicinchonic acid (BCA) assay (Pierce, Rockford, IL) using WT 3RS-Tau standards. The concentrations were then validated with SDS PAGE gels (Bio-Rad, Hercules, CA). For labeling, samples were incubated with 10-fold molar excess Dithiothreitol (DTT) at room temperature for 2 h followed by DTT removal with a 2 ml 7K MWCO Zeba™ spin desalting column (Peirce, Rockford, IL). Samples were then incubated with 3-fold molar excess of Alexa Fluor® (488, 532 or 568) C5 Maleimide (Invitrogen Molecular Probes, Carlsbad, CA) for 2 h at room temperature. Excess fluor was removed with desalting columns. A 640® Spectrophotometer (Beckman, Pasadena, CA) was used to determine the labeling efficiency using the following Alexa extinction coefficients: Alexa 488 – 71,000 $cm^{-1}M^{-1}$ at 495 nm; Alexa 532 – 78,000 $cm^{-1}M^{-1}$ at 532 nm; Alexa 568 – 88,000 $cm^{-1}M^{-1}$ at 578 nm. The protein concentration was determined using the BCA assay and the ratio of fluor concentration to protein concentration was calculated. All Tau proteins had labeling efficiencies of 30 - 86% (detailed in Supplemental Table S2.1).

Tubulin Purification and Microtubule Preparation Tubulin was purified from bovine brain obtained from Vermont Livestock & Slaughter (Ferrisburgh, VT) as previously described (McVicker *et al.*, 2014). Purified tubulin was clarified by ultracentrifugation (20 min, 95,000 rpm, 4°C) in an Optima™ TLX Ultracentrifuge (Beckman, Pasadena, CA). Following clarification, tubulin was mixed with rhodamine-labeled tubulin (Cytoskeleton Inc., Denver, CO) at a 1:200 (labeled:unlabeled) ratio and supplemented with 1 mM GTP (Sigma-Aldrich, St. Lois, MO). This mixture was incubated for 20 min at 37°C. Following polymerization, microtubules were stabilized with 20 µM paclitaxel (Sigma-Aldrich, St. Lois, MO). Post-clarification tubulin concentration was calculated

with the spectrophotometer using the tubulin extinction coefficient of 115,000 $cm^{-1}M^{-1}$ at 280 nm.

Coverslip Preparation and Flow Chamber Assembly For silanization, glass coverslips were incubated in 100% methanol for 2 h with shaking. Methanol-washed coverslips were then plasma cleaned (Harrick Plasma Cleaner, HarrickPlasma, Ithaca, NY) for 2-5 min and then incubated in a silane mixture (97% toluene (Sigma-Aldrich, St. Lois, MO), 2% 2-methoxy(polyethyleneoxy)propyltrimethoxysilane (Gelest Inc., Morrisville, PA), and 1% butylamine (Acros Organics, New Jersey, USA)) with flowing nitrogen gas for 90 min (Lowndes and Nelson, 2013). Coverslips were then washed in toluene (Lowndes and Nelson, 2013) and then dried and cured with flowing nitrogen gas for 30 min. Using Norland optical adhesive (Norland Products, Cranbury, NJ), flow chambers were constructed by adhering ARTUS shims (ARTUS, Eaglewood, NJ) to the silanized glass coverslips before 15 min UV irradiation (McVicker *et al.*, 2011).

***In vitro* TIRF Dynamics Assay** Paclitaxel stabilized microtubules were incubated with WT, alanine (Y18A), single glutamic acid (Y18E) or double glutamic acid (dE) 3RS-Tau constructs at a 1:3000 (Tau:tubulin) ratio (10-12 nM) 30 min prior to imaging. For imaging, washes and incubations were performed with BRB80+OS (BRB80 supplemented with a previously published oxygen scavenging system (McVicker *et al.*, 2011)). Flow chambers were incubated with monoclonal anti-β III (neuronal) tubulin antibodies (Sigma-Aldrich, St. Lois, MO) at 33 µg/mL for 5 min followed by a 5 min 2X chamber volume wash with 2mg/mL BSA (Sigma-Aldrich, St. Lois, MO). Alternatively, a 5 min 2.5% Pluronic® F-127 (Sigma-Aldrich, St. Lois, MO) incubation was done before the chambers were washed (10X chamber volume) with BSA for 5 min to remove excess

Pluronic® F-127. Chambers were then incubated for 12 min with microtubule/Tau mixtures diluted to 0.5-1 µM. Finally, chambers were washed with 160-333 pM Tau (1:3000 imaging concentration) for 2-4 min to remove non-adherent microtubules. All Tau and microtubule dilutions were made in warm (37°C) BRB80+OS.

To observe Tau's behavior at a 1:5 (Tau:tubulin) ratio, the needed concentration of unlabeled WT or Y18E 3RS-Tau (200 nM) was spiked with 500 pM Alexa 488 labeled WT or Y18E 3RS-Tau. Microtubules were stabilized as described above and were incubated with either the WT or Y18E 3RS-Tau spike mixture 30 mins prior to imaging. As before, washes and incubations were performed with warm BRB80+OS. Microtubule/Tau mixtures were diluted to a final imaging concentration of 1 µM. Chambers were prepared as previously detailed and were then incubated with diluted microtubule/Tau mixtures. Chambers were washed with warm WT or Y18E 3RS-Tau mixtures (see above for concentrations) to remove non-adherent microtubules and keep Tau concentrations constant (2-4 min).

An inverted Eclipse Ti-U Microscope (Nikon, Melville, NY) with a 100X PlanApo objective lens (1.49 NA) and auxiliary 1.5X magnification and an XR/Turbo-Z (Stanford Photonics, Palo Alto, CA) camera running Piper Control v2.3.39 or v2.6.09 (Stanford Photonics, Palo Alto, CA) was used to perform TIRF microscopy as previously described (Previs *et al.*, 2012; Hoeprich *et al.*, 2014; Previs *et al.*, 2015). Alexa 488 labeled Tau and rhodamine labeled tubulin were excited and imaged as previously described with 473 nm or 532 nm argon lasers and previously reported emission filters (McVicker *et al.*, 2014). Images were collected at room temperature at 10 frames/s, 95 or 93 nm/pixel, 50 frames for microtubules and 500 or 1000 frames for Tau.

TIRF Binding Assay The affinity and cooperativity of 3RS-Tau binding to microtubules were assessed using a TIRF-based binding assay. Microtubules were prepared as described above expect that labeling was carried out with porcine HiLyte 488 labeled tubulin (Cytoskeleton Inc., Denver, CO) at a 1:400 (labeled:unlabeled) ratio. Tau constructs were labeled with Alexa 532 as described above. As with the *in vitro* Dynamics Assay, all dilutions, washes and incubations were done in BRB80+OS. Final Tau and microtubule dilutions were done in warm BRB80+OS as described above. Microtubules were polymerized as described except that no Tau was added prior to imaging. Microtubules were then flowed into prepared flow chambers at 1.5 µM as described above. Initially, chambers were washed to remove non-adherent microtubules. Then, 50 nM Tau was flowed in and imaged. Following this, increasing concentrations of Tau were flowed in and imaged until a final concentration of 650 nM was reached. 20 frames of Tau were collected at 10 frames/s for each concentration. Imaging was done on the same system with the same conditions used for the *in vitro* TIRF Dynamics Assay described above.

***Ex vivo* TIRF Dynamics Assay** To visualize Tau under physiological conditions, Atlantic squid (*Loligo pealii*; Marine Biological Laboratory in Woods Hole, MA) axons were isolated and their axoplasms extruded following previously established protocols (Brady *et al.*, 1993; Song and Brady, 2013). Briefly, flow chambers were constructed using 25 x 75 x ~1 mm glass slides (VWR Scientific, Radnor, PA) and strips of 22 × 22 mm coverslips (VWR Scientific, Radnor, PA) cut with a diamond tipped pen and coated with Compound III Silicon grease (Dow Corning, Midland, MI). Paired axoplasms were extruded onto individual chamber slides. Flow chambers were then completed by adding

a top coverslip that was silanized as previously described. Chambers were then secured with a 1:1:1 lanoline, vaseline and paraffin mixture (Song and Brady, 2013).

Tau constructs were initially diluted in 20 mM HEPES (pH 7.2) and all axoplasm imaging was done in Buffer X/0.8 (437.5 mM potassium aspartate, 162.5 mM taurine, 87.5 mM betaine, 62.5 mM glycine, 25 mM HEPES, 16.25 mM $MgCl_2$, 12.5 mM EGTA, 3.75 mM $CaCl_2$, 1.25 mM glucose, pH 7) (Song and Brady, 2013) diluted to Buffer X/2 with ddH_2O. Perfusion mixtures were made with 200 nM Alexa 568 labeled Y18A or Y18E 3RS-Tau, 500 pM Alexa 488 labeled Y18A or Y18E 3RS-Tau and a final ATP concentration of 1 mM. Following perfusion, axoplasms were incubated at room temp for 20 min before imaging began. An inverted Eclipse Ti microscope (Nikon, Melville, NY) with a 100x Apochromatic objective lens (1.49 NA) was used to carry out TIRF microscopy with 488 nm (LU-NV laser combiner, Nikon, Melville, NY) and 561 nm (Agilent MLC400 Monolithic Laser Combiner, Santa Clara, CA) lasers and emission band-pass filter sets 525/50 nm and 600/50 nm (Chroma Technology, Bellows Falls, VT). An Andor iXon Ultra 897 camera (Belfast BT12 7AL, UK) running NIS-Elements AR v4.30.02 (Nikon, Melville, NY) was used to image Tau in the axoplasm. The relatively high concentration of Alexa 568 (200 nM) labeled Tau allowed for visualization of microtubules while the low Alexa 488 (500 pM) labeled Tau concentration allowed imaging of single Tau molecules. One hundred frames each were collected at room temperature of microtubules and Tau with an interval of 0.3 s and a pixel size of 0.16 x 0.16 µm.

***In vitro* Kinesin-1 Motility Assay** Motility assays were performed with a truncated (560 aa) *Drosophila melanogaster* biotin tagged kinesin-1 construct (gift from Hancock lab).

Motors were labeled with streptavidin conjugated Qdot® 655 (Life Technologies, Carlsbad, CA) at a 1:4 (motor:Qdot) ratio. Paclitaxel stabilized microtubules were prepared as described above except that after polymerization microtubules were centrifuged at room temperature for 30 min before the pellet was resuspended in motility assay buffer (MAB) (10 mM PIPES, pH 7.4 at room temperature, 50 mM potassium acetate, 4 mM magnesium acetate, 1 mM EGTA) at 37ºC supplemented with an oxygen scavenging system (MAB+OS) as previously described (Hoeprich *et al.*, 2014). Prior to imaging, microtubules were incubated with Tau (Alexa 488 labeled or unlabeled WT or Y18E 3RS-Tau) at a 1:5 (Tau:tubulin) ratio for 20 min at 37ºC. Flow chambers were prepared by incubation with monoclonal anti-tubulin antibodies (detailed above) diluted with MAB+OS. Blocking and washing were done as previously detailed. Briefly, chambers were blocked with 0.5 mg/mL of BSA in MAB+OS before 1 μM of microtubules or microtubules/Tau as added and incubated as for the Tau behavioral assays. Non-adherent microtubules were removed with an MAB+OS wash. A working concentration of 20 pM – 50 pM kinesin-1 along with 1 mM ATP was added just prior to imaging. Imaging was performed on the same system as the *in vitro* Tau assays. Qdots were excited with the 473 nm laser and all movies were acquired at five frames per second.

Data Analysis *In vitro TIRF Dynamics Assays* ImageJ 1.48v (NIH, Bethesda, MD) was used to create kymographs of Tau interacting with the microtubule using the MultipleKymograph plugin. To determine dwell times, the MTrackJ plugin was used to measure the length of events that were clearly static or dynamic. Eleven percent of events display switching and were not included in further analysis. Only events that began,

remained and ended on the microtubule during the imaging period were used. Dynamic and static dwell times were exported to GraphPad Prism v6.00 (GraphPad Software, La Jolla, CA). Cumulative frequency distribution plots were generated for each population and fit to one or two phase exponential functions. Average dwell times were calculated as the time constant of the exponential function. The goodness of the fit (R^2) and the 95% confidence bands were also reported. Fisher's Exact Test was used to determine statistical significance for static compared to dynamic populations of 3RS-Tau construct data sets. All data sets are composites of data collected on different days. High concentration (Spike): (WT, N = 8; Y18E, N = 8), comparable bound fraction: (WT, N = 12; Y18A, N= 5; Y18E, N = 4; dE, N = 5).

Ex vivo TIRF Dynamics Assay Events were tracked using the MTrackJ plugin for ImageJ. Events were chosen if they lasted more than one frame and if the signal remained within a snap range of 13 x 13 pixels from one frame to the next (snap range chosen based on maximum diffusive range of a Tau protein (Konzack *et al.*, 2007)). Tracks were exported to Excel and events with a max distance from start $\leq$ 0.5 µm were designated static while events $>$ 0.5 µm were designated dynamic. GraphPad Prism was used as described above, to plot the cumulative frequency distribution of the dwell times to which one phase exponential functions were fit. The average dwell time was determined from the fit of the exponential function. As above, the goodness of the fit (R^2) and the 95% confidence bands were reported. Statistical significance was determined using Chi-square with Yates' correction. All data sets are comprised of data collected on different days (WT, N = 4; Y18A, N= 5; Y18E, N = 5).

TIRF Binding Assay The average intensity (*Avg I*; Arbitrary Units) per unit length of Tau binding the microtubule was measured for each frame using the Multi Measure plugin for ImageJ. In GraphPad Prism, the average *AvgI* per unit length was used to plot $\frac{Avg\ I}{Unit\ Length}$ vs [*Tau*]. Binding curves were fit to one site-specific binding with Hill slope, which was used to determine the Hill coefficient and K_D using the Hill equation:

$$\frac{Avg\ I}{Unit\ Length} = \frac{A_{max}[Tau]^h}{K_D^h + [Tau]^h}$$

where *h* is the Hill coefficient and A_{max} is the maximum $\frac{Avg\ I}{Unit\ Length}$ The $\frac{Avg\ I}{Unit\ Length}$ reported here was normalized to *Amax*. Tau's fraction bound (f_B) for the kinesin-1 motility assay was determined using the equation:

$$f_B = \frac{[MT]}{K_{D_{Tau}} + [MT]}$$

where [*MT*] is the concentration of microtubules used for imaging and $K_{D_{Tau}}$ is the affinity of Tau for the microtubule surface calculated in the binding assay. All data sets are comprised of data collected on different days (WT, N = 4; Y18A, N= 3; Y18E, N = 3).

In vitro Kinesin-1 Motility Assay Data were analyzed as reported previously (Hoeprich *et al.*, 2014). Briefly, the MTrackJ plugin for ImageJ was used to measure motility while the segmented line tool was used to measure track lengths. Average velocity was plotted as a histogram and fit to a Gaussian distribution. The mean and standard deviation are reported here. Using methods that we have previously outlined (Thompson *et al.*, 2013), cumulative frequency plots were generated for run lengths corrected for microtubule track length effects (through resampling of the data) and reported here (99% confidence

level of data resampling repeated 10,000 times). Statistical significance was determined as previously described (Thompson *et al.,* 2013). All data sets are comprised of data collected on different days (No Tau, N = 10; WT, N = 10; Y18E, N = 10).

Statistics For the motor motility assay average velocities for events were fit to a Gaussian distribution. The mean of the average velocities and standard deviation of those velocities are reported here. It has been shown that motor run length is affected by the length of the track (Thompson *et al.*, 2013). Differences in microtubule track length that might lead to underestimation of motor run length were corrected using previously published work (Thompson *et al.,* 2013). Average run lengths were determined using a bootstrapping method where data was resampled with replacement (for the size of the data set) 10,000 times (Thompson *et al.,* 2013). The standard deviation in these values is reported. Statistical significance was determined as previously described by comparing resampled data for the run length (difference between observed and control run lengths) to a null hypothesis (Thompson *et al.*, 2013).

For the *in vitro* and dynamics assays, the percentage of events that were static or diffusive are reported for 14 experiments. The error bars represent the standard deviation in the percentage of static or diffusive events across 14 separate experiments. Significance was determined using Fisher's Exact Test (a variation of a Chi-squared test which calculates an exact P-value) best used when the sample size is small.

Like the *in vitro* dynamics assays, the *ex vivo* dynamics assay reports the percentage of static or diffusive events for a dataset made up of 5 experiments. The error bars are also the standard deviation in the percentage of static or diffusive events across 5 experiments. Because of the larger sample size, significance was determined using a Chi-

squared test with Yates' correction to improve the P-value approximation of the Chi-squared test.

The TIRF binding assay reports the average intensity per unit length at each concentration imaged. The error bars represent the standard deviation in intensity at each concentration over 4 experiments.

2.6 Acknowledgements

This work was supported by NIGMS/NIH funding to Dr. Christopher Berger (GM101066) and Dr. Gerardo Morfini (NS066942A). We thank Dr. David Warshaw and Guy Kennedy for training, use and technical support of the TIRF microscope used at the University of Vermont. Special thanks to Vermont Livestock & Slaughter (Ferrisburgh, VT) for their continued support of our work. We would also like to thank the Marine Biological Laboratory for providing an extraordinary working environment. Thanks to Dr. Lynne Chang (Nikon; Melville, NY) for provision of, and technical support for the TIRF microscope used at the Marine Biological Laboratory. Thanks to Dr. William Hancock for use of his kinesin-1 construct. Additional thanks to Dr. Scott Brady, Dr. Jason Stumpff, Lynn Chrin, Phillipe Mouchati, Rehan Ali, Minsu Kang and Henry Thomsett for their support at different stages in the development of this work. The authors declare no conflicts of interest with the work presented here. This manuscript was written by JS and CB. JS, CB and GM participated in editing. Experiments were designed by JS, GH, GM and CB and performed by JS, DL and GH.

References

Andreadis, A. (2005). Tau gene alternative splicing: expression patterns, regulation and modulation of function in normal brain and neurodegenerative diseases. Biochim. Biophys. Acta *1739*, 91-103.

Ballatore, C., Lee, V.M., and Trojanowski, J.Q. (2007). Tau-mediated neurodegeneration in Alzheimer's disease and related disorders. Nat. Rev. Neurosci. *8*, 663-672.
Brady, S.T., Richards, B.W., and Leopold, P.L. (1993). Assay of vesicle motility in squid axoplasm. Methods Cell Biol. *39*, 191-202.
Dixit, R., Ross, J.L., Goldman, Y.E., and Holzbaur, E.L. (2008). Differential regulation of dynein and kinesin motor proteins by tau. Science *319*, 1086-1089.
Elbaum-Garfinkle, S., and Rhoades, E. (2012). Identification of an aggregation-prone structure of tau. J. Am. Chem. Soc. *134*, 16607-16613.
Feinstein, H.E., Benbow, S.J., LaPointe, N.E., Patel, N., Ramachandran, S., Do, T.D., Gaylord, M.R., Huskey, N.E., Dressler, N., Korff, M., Quon, B., Cantrell, K.L., Bowers, M.T., Lal, R., and Feinstein, S.C. (2016). Oligomerization of the Microtubule Associated Protein Tau is Mediated by its N-Terminal Sequences: Implications for Normal and Pathological Tau Action. J. Neurochem.
Funk, K.E., Thomas, S.N., Schafer, K.N., Cooper, G.L., Liao, Z., Clark, D.J., Yang, A.J., and Kuret, J. (2014). Lysine methylation is an endogenous post-translational modification of tau protein in human brain and a modulator of aggregation propensity. Biochem. J. *462*, 77-88.
Gerson, J.E., Sengupta, U., Lasagna-Reeves, C.A., Guerrero-Munoz, M.J., Troncoso, J., and Kayed, R. (2014). Characterization of tau oligomeric seeds in progressive supranuclear palsy. Acta neuropathologica communications *2*, 73.
Goode, B.L., Chau, M., Denis, P.E., and Feinstein, S.C. (2000). Structural and functional differences between 3-repeat and 4-repeat tau isoforms. Implications for normal tau function and the onset of neurodegenetative disease. J. Biol. Chem. *275*, 38182-38189.
Hinrichs, M.H., Jalal, A., Brenner, B., Mandelkow, E., Kumar, S., and Scholz, T. (2012). Tau protein diffuses along the microtubule lattice. J. Biol. Chem. *287*, 38559-38568.
Hoeprich, G.J., Thompson, A.R., McVicker, D.P., Hancock, W.O., and Berger, C.L. (2014). Kinesin's neck-linker determines its ability to navigate obstacles on the microtubule surface. Biophys. J. *106*, 1691-1700.
Janning, D., Igaev, M., Sundermann, F., Bruhmann, J., Beutel, O., Heinisch, J.J., Bakota, L., Piehler, J., Junge, W., and Brandt, R. (2014). Single-molecule tracking of tau reveals fast kiss-and-hop interaction with microtubules in living neurons. Mol. Biol. Cell *25*, 3541-3551.
Jeganathan, S., von Bergen, M., Brutlach, H., Steinhoff, H.J., and Mandelkow, E. (2006). Global hairpin folding of tau in solution. Biochemistry *45*, 2283-2293.
Kamah, A., Huvent, I., Cantrelle, F.X., Qi, H., Lippens, G., Landrieu, I., and Smet-Nocca, C. (2014). Nuclear magnetic resonance analysis of the acetylation pattern of the neuronal Tau protein. Biochemistry *53*, 3020-3032.
Kanaan, N.M., Morfini, G., Pigino, G., LaPointe, N.E., Andreadis, A., Song, Y., Leitman, E., Binder, L.I., and Brady, S.T. (2012). Phosphorylation in the amino terminus of tau prevents inhibition of anterograde axonal transport. Neurobiol. Aging *33*, 826 e815-830.
Kanaan, N.M., Morfini, G.A., LaPointe, N.E., Pigino, G.F., Patterson, K.R., Song, Y., Andreadis, A., Fu, Y., Brady, S.T., and Binder, L.I. (2011). Pathogenic forms of tau inhibit kinesin-dependent axonal transport through a mechanism involving activation of axonal phosphotransferases. J. Neurosci. *31*, 9858-9868.

Konzack, S., Thies, E., Marx, A., Mandelkow, E.M., and Mandelkow, E. (2007). Swimming against the tide: mobility of the microtubule-associated protein tau in neurons. J. Neurosci. *27*, 9916-9927.
LaPointe, N.E., Morfini, G., Pigino, G., Gaisina, I.N., Kozikowski, A.P., Binder, L.I., and Brady, S.T. (2009). The amino terminus of tau inhibits kinesin-dependent axonal transport: implications for filament toxicity. J. Neurosci. Res. *87*, 440-451.
Larson, M., Sherman, M.A., Amar, F., Nuvolone, M., Schneider, J.A., Bennett, D.A., Aguzzi, A., and Lesne, S.E. (2012). The complex PrP(c)-Fyn couples human oligomeric Abeta with pathological tau changes in Alzheimer's disease. J. Neurosci. *32*, 16857-16871a.
Lee, G., Newman, S.T., Gard, D.L., Band, H., and Panchamoorthy, G. (1998). Tau interacts with src-family non-receptor tyrosine kinases. J. Cell Sci. *111 (Pt 21)*, 3167-3177.
Lovestone, S., Hartley, C.L., Pearce, J., and Anderton, B.H. (1996). Phosphorylation of tau by glycogen synthase kinase-3 beta in intact mammalian cells: the effects on the organization and stability of microtubules. Neuroscience *73*, 1145-1157.
Lowndes, M., and Nelson, W.J. (2013). Fabricating surfaces with distinct geometries and different combinations of cell adhesion proteins. Methods Mol. Biol. *1046*, 219-230.
Maday, S., Twelvetrees, A.E., Moughamian, A.J., and Holzbaur, E.L. (2014). Axonal transport: cargo-specific mechanisms of motility and regulation. Neuron *84*, 292-309.
Martin, L., Latypova, X., Wilson, C.M., Magnaudeix, A., Perrin, M.-L., Yardin, C., and Terro, F. (2013). Tau protein kinases: Involvement in Alzheimer's disease. Ageing Research Reviews *12*, 289-309.
McVicker, D.P., Chrin, L.R., and Berger, C.L. (2011). The nucleotide-binding state of microtubules modulates kinesin processivity and the ability of Tau to inhibit kinesin-mediated transport. J. Biol. Chem. *286*, 42873-42880.
McVicker, D.P., Hoeprich, G.J., Thompson, A.R., and Berger, C.L. (2014). Tau interconverts between diffusive and stable populations on the microtubule surface in an isoform and lattice specific manner. Cytoskeleton (Hoboken, N.J.) *71*, 184-194.
Morfini, G., Szebenyi, G., Elluru, R., Ratner, N., and Brady, S.T. (2002). Glycogen synthase kinase 3 phosphorylates kinesin light chains and negatively regulates kinesin-based motility. EMBO J. *21*, 281-293.
Morris, M., Knudsen, G.M., Maeda, S., Trinidad, J.C., Ioanoviciu, A., Burlingame, A.L., and Mucke, L. (2015). Tau post-translational modifications in wild-type and human amyloid precursor protein transgenic mice. Nat. Neurosci. *18*, 1183-1189.
Panda, D., Samuel, J.C., Massie, M., Feinstein, S.C., and Wilson, L. (2003). Differential regulation of microtubule dynamics by three- and four-repeat tau: implications for the onset of neurodegenerative disease. Proc. Natl. Acad. Sci. U. S. A. *100*, 9548-9553.
Previs, M.J., Beck Previs, S., Gulick, J., Robbins, J., and Warshaw, D.M. (2012). Molecular mechanics of cardiac myosin-binding protein C in native thick filaments. Science *337*, 1215-1218.
Previs, M.J., Prosser, B.L., Mun, J.Y., Previs, S.B., Gulick, J., Lee, K., Robbins, J., Craig, R., Lederer, W.J., and Warshaw, D.M. (2015). Myosin-binding protein C corrects an intrinsic inhomogeneity in cardiac excitation-contraction coupling. Sci Adv *1*.

Qian, W., Jin, N., Shi, J., Yin, X., Jin, X., Wang, S., Cao, M., Iqbal, K., Gong, C.X., and Liu, F. (2013). Dual-specificity tyrosine phosphorylation-regulated kinase 1A (Dyrk1A) enhances tau expression. J. Alzheimers Dis. *37*, 529-538.
Song, Y., and Brady, S.T. (2013). Analysis of microtubules in isolated axoplasm from the squid giant axon. Methods Cell Biol. *115*, 125-137.
Thompson, A.R., Hoeprich, G.J., and Berger, C.L. (2013). Single-molecule motility: statistical analysis and the effects of track length on quantification of processive motion. Biophys. J. *104*, 2651-2661.
Vershinin, M., Carter, B.C., Razafsky, D.S., King, S.J., and Gross, S.P. (2007). Multiple-motor based transport and its regulation by Tau. Proc. Natl. Acad. Sci. U. S. A. *104*, 87-92.
Watanabe, A., Hasegawa, M., Suzuki, M., Takio, K., Morishima-Kawashima, M., Titani, K., Arai, T., Kosik, K.S., and Ihara, Y. (1993). In vivo phosphorylation sites in fetal and adult rat tau. J. Biol. Chem. *268*, 25712-25717.
Yu, I., Garnham, C.P., and Roll-Mecak, A. (2015). Writing and Reading the Tubulin Code. J. Biol. Chem. *290*, 17163-17172.

Figures

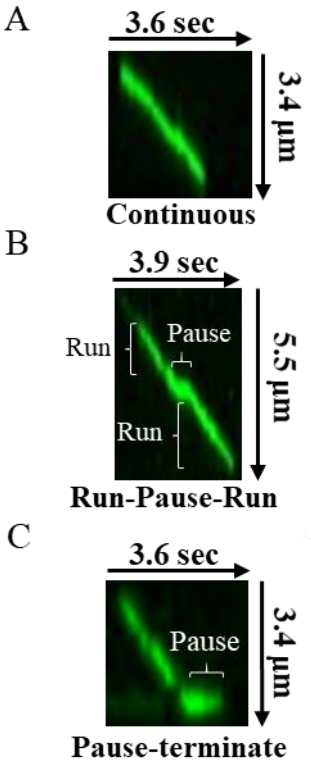

Figure 2. 1 Representative kymographs of kinesin-1 motility.

TIRF microscopy was used to observe kinesin-1 motility was in the absence of Tau and in the presence of unlabeled or Alexa 488 labeled WT and Y18E 3RS-Tau (200 nM (1:5, Tau:tubulin)). Continuous (A), Run-Pause-Run (B) and Pause-Terminate (C) events were observed under all conditions.

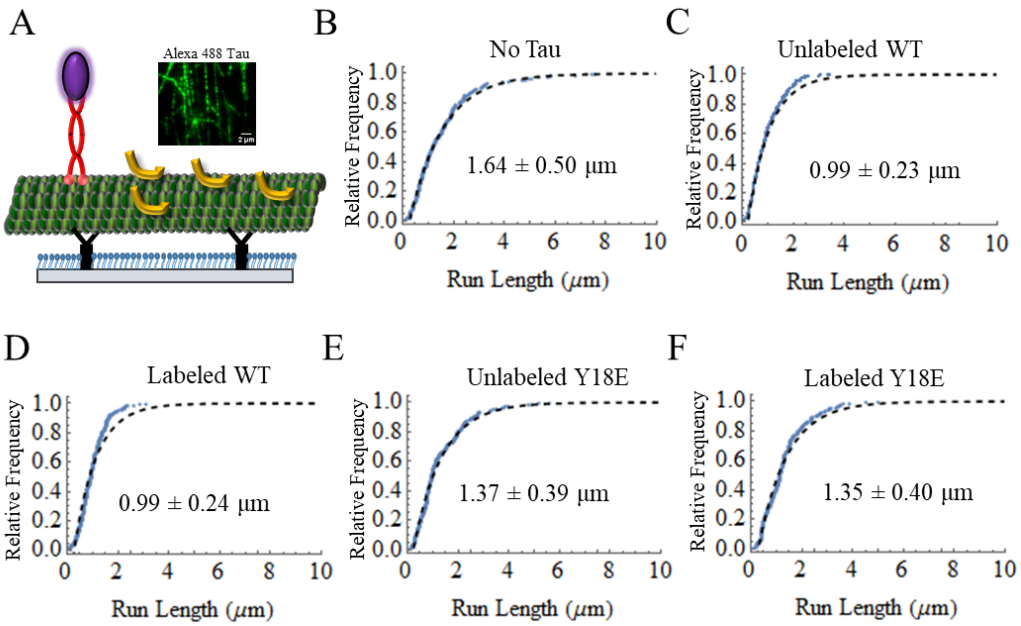

Figure 2.2 Diagram of motility assays with cumulative frequency plots of run lengths (mean ± SD) for kinesin-1 in the absence and presence of 3RS-Tau.

A) Flow chambers were passivated with PEG-silane (blue) before tubulin antibodies (black) were used to adhere paclitaxel stabilized microtubules (green). Q-dot labeled kinesin-1 (purple/red) motility was observed on undecorated or label/unlabeled Tau (yellow) decorated microtubules. Inset: Unlabeled microtubules coated with 200 nM Alexa 488 labeled Tau. B) On undecorated microtubules, kinesin-1 had a run length of 1.64 ± 0.50 µm. Introduction of both unlabeled (C) and labeled (D) WT 3RS-Tau, significantly reduced kinesin-1's run length to 0.99 ± 0.23 and 0.99 ± 0.24 µm ($p < 0.05$). In the presence of unlabeled (E) and labeled (F) Y18E 3RS-Tau, kinesin-1's run length was significantly increased to 1.37 ± 0.39 µm ($p < 0.05$) and 1.35 ± 0.40 µm ($p < 0.05$), respectively. Introduction of negative charge reduced Tau's ability to inhibit kinesin-1 motility and led to a significant increase in run length (Supplemental Table S2.2). Experiments: 10.

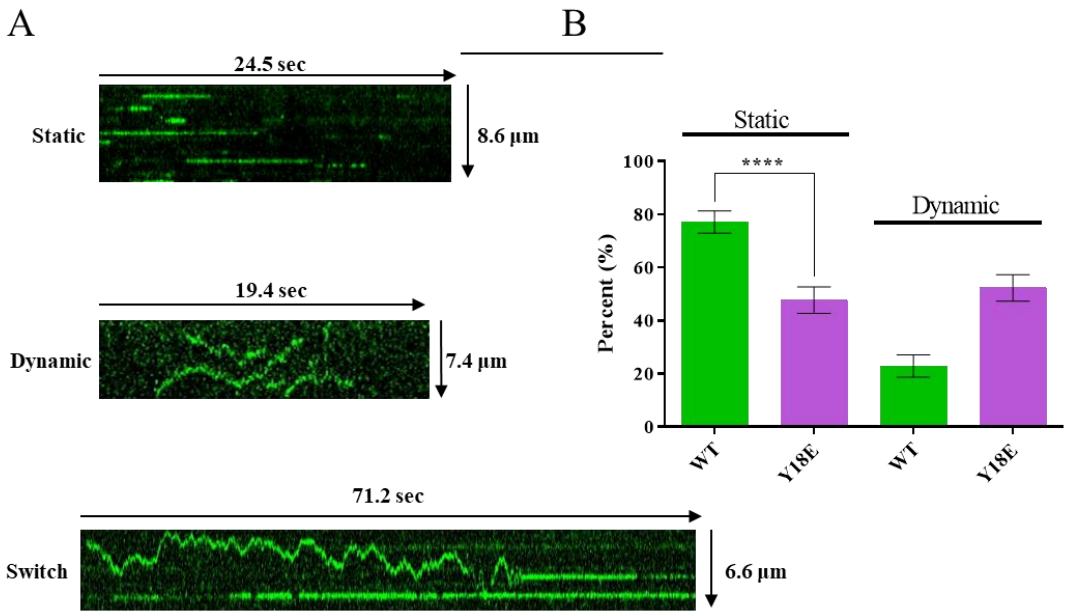

Figure 2.3 Comparison of WT and Y18E 3RS-Tau behavior on Taxol stabilized microtubules at high concentration.

A) Representative kymographs show the different types of behaviors that can be observed. Tau can bind statically (Static: horizontal lines) while interacting with the microtubule or exhibit dynamic binding along the microtubule surface (Dynamic: jagged lines). Tau can also switch between these states (Switch). B) Bar graph comparing the percentage (± SD) of static to dynamic events for WT and Y18E 3RS-Tau. For WT 3RS-Tau, 77.1 ± 4.2% of events were static while Y18E 3RS-Tau's equilibrium was shifted towards the dynamic state (47.7 ± 5.0% static events). (**** denotes a statistically significant difference of $p < 0.05$). Events: WT = 388, Y18E = 235 from eight experiments.

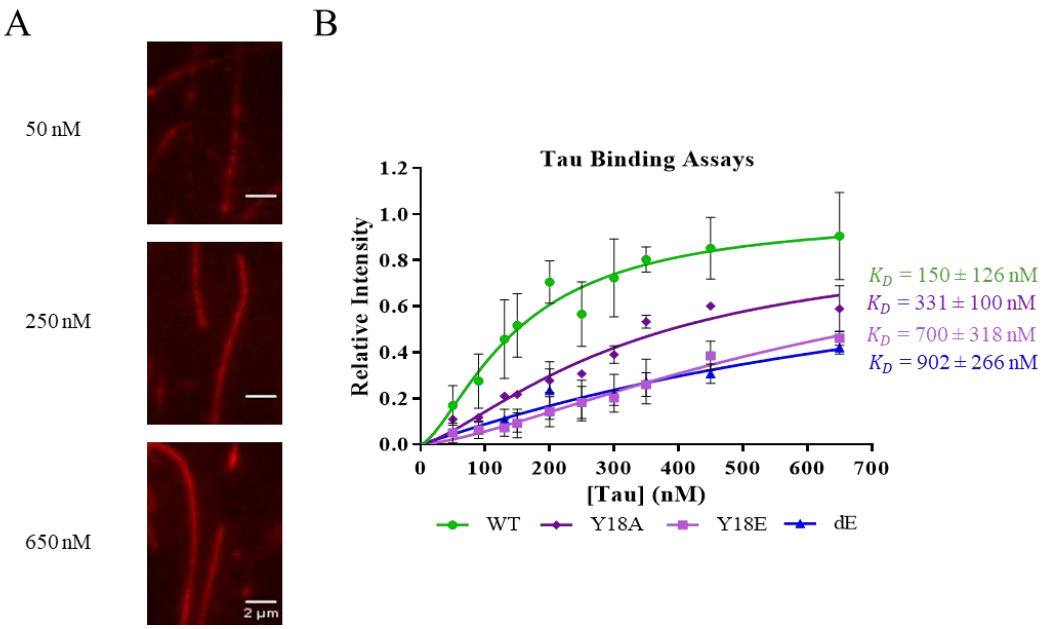

Figure 2.4 Comparison of TIRF binding assays.

TIRF binding assays for WT (N = 4), Y18A (N = 3), Y18E (N = 3) and dE (N = 3) 3RS-Tau. WT 3RS-Tau had a K_D (mean ± SD) of 150 ± 126 nM, Y18A 3RS-Tau had a K_D of 331 ± 100 nM, Y18E 3RS-Tau had a K_D of 700 ± 318 nM and dE 3RS-Tau had a K_D of 902 ± 266 nM. The affinity of Tau for the microtubule surface decreases with the introduction of increasing negative charge at Y18.

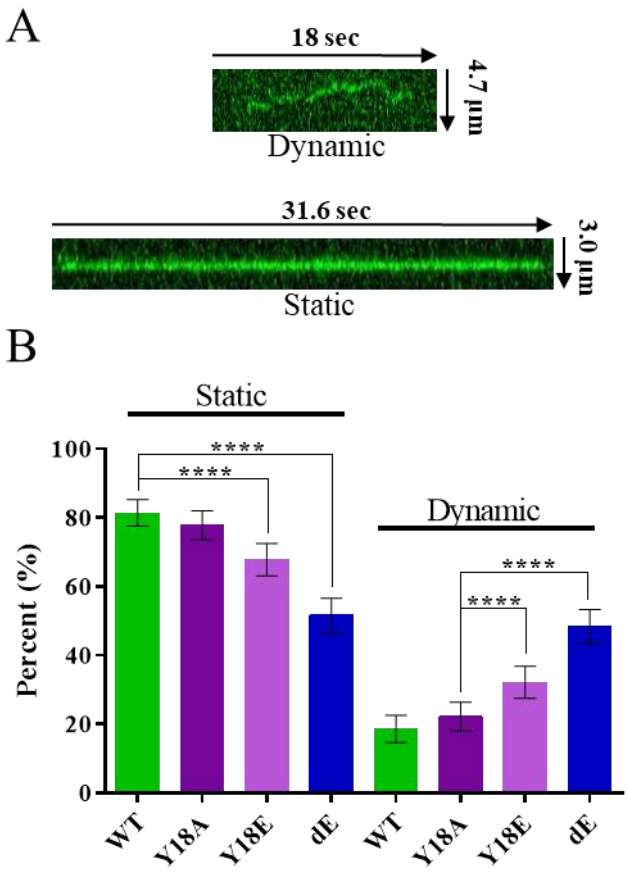

Figure 2.5 The behavior of comparable bound fractions of WT, Y18A, Y18E and dE 3RS-Tau on paclitaxel-stabilized microtubules.

A) Representative kymographs show both dynamic (jagged line) and static binding along the microtubule surface (horizontal lines). B) Bar graph comparing the percentage of static to dynamic events (percentage ± SD) for each Tau construct. Introduction of negative charges at Y18 and T17 shifted the equilibrium between the static and dynamic states towards the dynamic state. (****) denotes a statistically significant difference of $p < 0.05$. Events: WT = 566 (N = 12), Y18A = 320 (N = 5), Y18E = 472 (N = 4), and dE = 220 (N = 5).

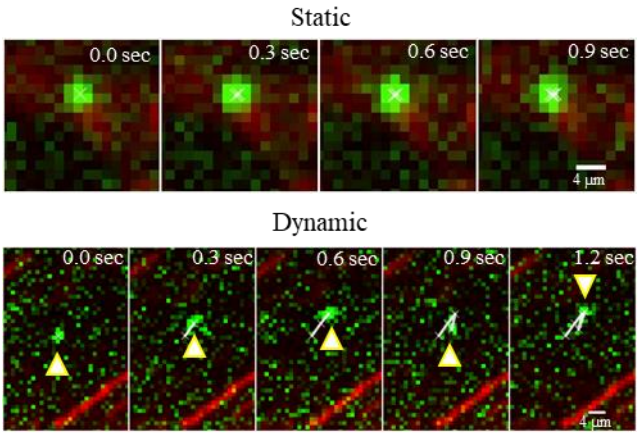

Figure 2.6 Static and dynamic (arrow) binding events with the axoplasm.

Squid giant axon axoplasm samples were used to image WT, Y18A and Y18E 3RS-Tau interactions (500 pM Alexa 488 labeled Tau, green) with axonal microtubules (200 nM Alexa 568 labeled Tau, red). Tau binds both statically and dynamically under physiological conditions.

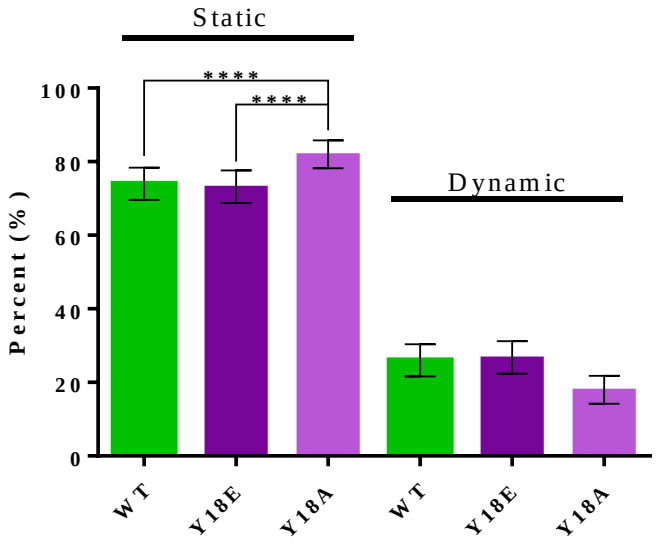

Figure 2.7 Tau's binding equilibrium between static and dynamic states is maintained *ex vivo*.

Bar graph comparing the percentage (± SD) of static to dynamic events for Y18E and Y18A 3RS-Tau in the axoplasm preparation. As observed *in vitro* (Figures 3 and 5), a shift in Tau's equilibrium towards the dynamic state was observed upon introduction of negative charge at Y18. ****:$p < 0.05$. Events: Y18A = 972 (N = 5), WT =1129 (N = 4), Y18E = 757 (N = 5).

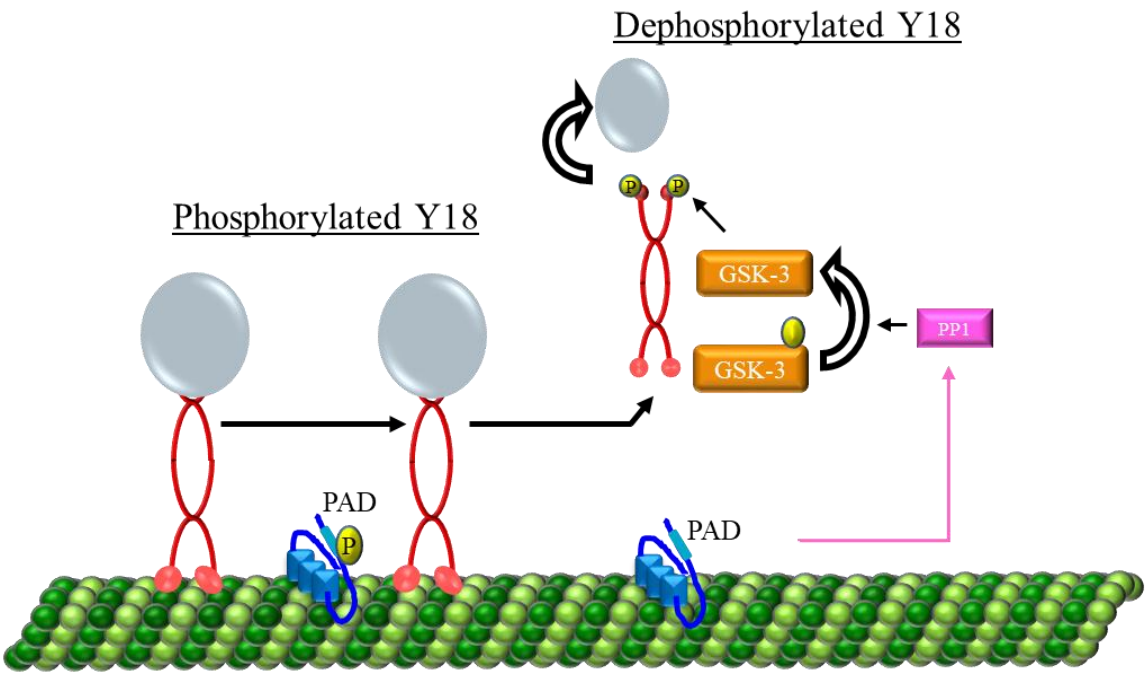

Figure 2.8 Model of Tau regulation.

Results from our work here indicate that Y18 phosphorylation (yellow) not only prevents PP1 activation induced by exposed PAD (light blue) (Kanaan *et al.*, 2012), but also stabilizes Tau (blue) in the dynamic state, allowing for continued kinesin-1 (red) mediated cargo transport. On the other hand, Y18 dephosphorylation would shift Tau's equilibrium towards the more inhibitory static state while allowing PAD activation of PP1 (pink) upon exposure. PP1 would then dephosphorylate and activate GSK-3β (orange), which in turn phosphorylates kinesin-1 light chains and promotes dissociation from its transported cargoes. Thus, misregulation of Tau's dynamic equilibrium could promote neuronal degeneration by compromising localized delivery of kinesin-1 cargoes.

Table S2.1: Tau Labeling Efficiencies

	Percent (%) Labeled		
	Alexa 488	**Alexa 532**	**Alexa 568**
WT 3RS-Tau	51	80	-
Y18A 3RS-Tau	86	-	40
Y18E 3RS-Tau	61	61	40
dE 3RS-Tau	32	30	-

Labeling efficiencies for all Tau constructs used in all *in vitro* and *ex vivo* experiments. Alexa 488 labeled Tau was used in *in vitro* and *ex vivo* dynamics assays. Alexa 568 labeled Tau was also used in *ex vivo* dynamics assays. Alexa 532 labeled Tau was used for *in vitro* binding assays.

Table S2.2: Kinesin-1 Behavior in the Presence and Absence of 3RS-Tau Constructs

3RS-Tau	N	$X_{observed}$ (µm) (± SD)	$L_{observed}$ (µm) (± SD)	$X_{corrected}$ (µm) (± SD)	P-value	Velocity (µm/s) (± SD)
None	215	1.32 ± 0.23	3.80 ± 0.87	1.64 ± 0.50	-	0.76 ± 0.09
WT Unlab.	332	0.84 ± 0.11	3.25 ± 0.72	0.99 ± 0.23	3.5×10^{-5}	0.75 ± 0.11
WT Lab.	245	0.85 ± 0.11	3.74 ± 0.23	0.99 ± 0.24	2.9×10^{-5}	0.70 ± 0.15
Y18E Unlab.	214	1.12 ± 0.21	3.52 ± 0.72	1.37 ± 0.39	0.003	0.70 ± 0.12
Y18E Lab.	252	1.12 ± 0.17	3.78 ± 0.74	1.35 ± 0.40	0.003	0.70 ± 0.12

Data from *in vitro* kinesin-1 motility assays. Observed run lengths ($X_{observed}$) and microtubule lengths ($L_{observed}$) were used to determine the corrected run length ($X_{corrected}$) following previously described methods (Thompson *et al.*, 2013). Median p-values for data sets compared to the no Tau condition were calculated using a previously detailed resampling method (Thompson *et al.*, 2013). Average velocities for kinesin-1 under all conditions tested. There was no change in velocity in the presence and absence of Tau.

Table S2.3: Behavior of 3RS-Tau Constructs in all Experimental Conditions

3RS-Tau	SpikeN	Spike % Static (± SD)	Spike Static Dwell Time (s)		Spke Dynamic Dwell Time (s)	Comp.N	Comp. % Static (± SD)	Comp. Static Dwell Time (s)		Comp. Dynamic Dwell Time (s)	K_D (nM) (± SD)
			Long	Short				Long	Short		
in vitro											
WT	388	77.1 ± 4.2	15.7 (R^2 = 0.9988) 80.2%	1.4 (R^2 = 0.9988) 19.8%	1.6 (R^2 = 0.9931)	566	81.4 ± 3.9	13.8 (R^2 = 0.9991) 42.6%	2.1 (R^2 = 0.9991) 57.4%	2.8 (R^2 = 0.9977)	150 ± 126
Y18A	-	-	-	-	-	320	77.8 ± 4.2	12.2 (R^2 = 0.9985) 29.4%	2.2 (R^2 = 0.9985) 70.6%	1.7 (R^2 = 0.9934)	-
Y18E	235	47.7 ± 5.0	14.5 (R^2 = 0.9960)		1.9 (R^2 = 0.9883)	469	67.8 ± 4.7	9.5 (R^2 = 0.9990) 39.8%	1.8 (R^2 = 0.9990) 60.2%	1.7 (R^2 = 0.9945)	700 ± 318
dE	-	-	-	-	-	219	51.6 ± 5.0	14.4 (R^2 = 0.9986) 63.7%	6.8 (R^2 = 0.9986) 32.7%	3.2 (R^2 = 0.9960)	902 ± 266
ex vivo											
WT	1129	74.0 ± 4.4	0.5 (R^2 = 0.9609)		0.4 (R^2 = 0.9578)	-	-	-		-	-
Y18A	972	82.0 ± 3.8	0.7 (R^2 = 0.9859)		0.9 (R^2 = 0.9785)	-	-	-	-	-	-
Y18E	757	73.2 ± 4.4	0.8 (R^2 = 0.9966)		1.3 (R^2 = 0.9924)	-	-	-	-	-	-

Data from *in vitro* and *ex vivo* dynamics assays along with *in vitro* binding assays. Spike Experiments: WT static dwell times were best fit to a two phase exponential function which revealed two populations of events with long and short dwell times (amplitudes given in table). Y18E static dwell times were best fit to a single exponential function one with one average dwell time. Dynamic dwell times were best fit to single exponential functions. *In vitro* binding assays: Affinity (K_D) was determined by plotting the average intensity Alexa 532 3RS-Tau per unit length of microtubule vs Tau concentration. These plots were normalized to max average intensity and fit to one site-specific binding with Hill slope curves. Comparable bound fraction Experiments: Comparable bound fractions were determined based on *in vitro* binding assays. All static dwell times were best fit to two phase exponential functions with both a long and short average dwell time. All dynamic dwell times were best fit to single exponential functions. *Ex vivo* dynamics assays: all dwell times were best fit to single exponential functions.

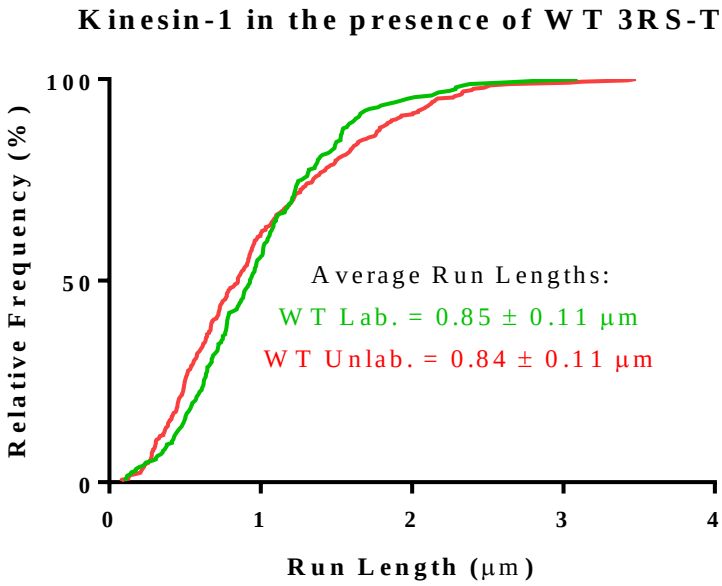

Figure S2.1 Cumulative frequency plots of uncorrected kinesin-1 run lengths in the presence of unlabeled and Alexa 488 labeled WT 3RS-Tau.

Average run lengths were calculated through data resampling (10,000 times) as previously described (Thompson *et al.*, 2013).

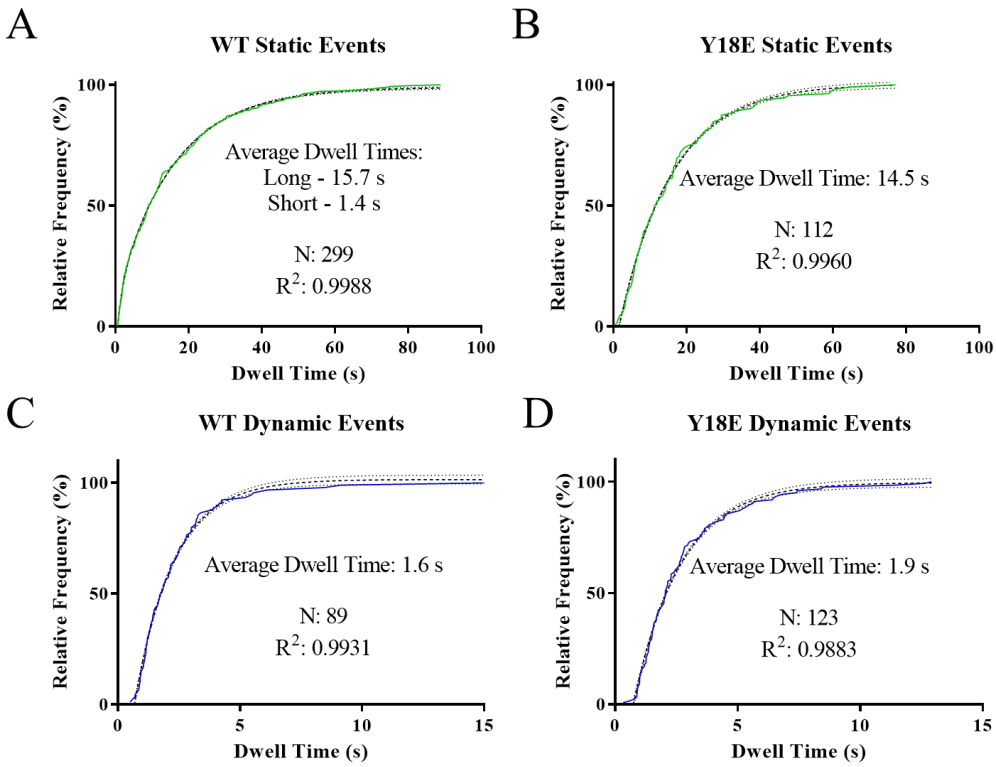

Figure S2.2 Cumulative frequency plots for WT and Y18E 3RS-Tau static and dynamic dwell times at high concentration.

All plots show 95% confidence bands as dotted lines. A) WT 3RS-Tau static dwell times were best fit to a two phase exponential function. This revealed an average long static dwell time of 15.7 s and a short static dwell time of 1.4 s (R^2 = 0.9988; N = 299). B) Y18E 3RS-Tau static dwell times best fit a one phase exponential function and had an average dwell time of 14.5 s (R^2 = 0.9960; N = 112). C) Dynamic dwell times for WT 3RS-Tau were fit to a one phase exponential function with an average dwell time of 1.6 s (R^2 = 0.9931; N = 89). D) Y18E 3RS-Tau dynamic dwell times were also fit to a one phase exponential function with an average of 1.9 s (R^2 = 0.9883; N = 123).

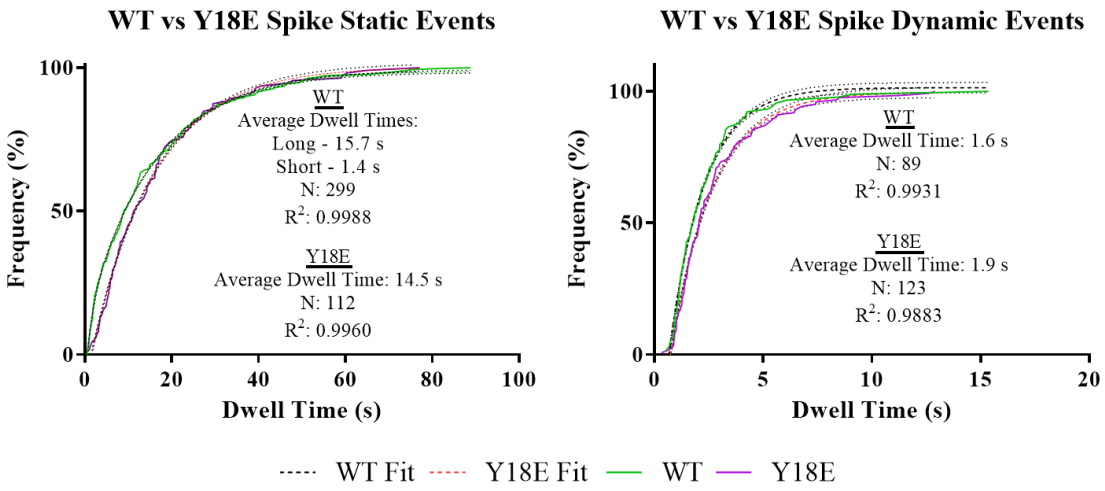

Figure S2.3 Overlay of static and dynamic cumulative frequency plots for WT and Y18E 3RS-Tau spike experiments.

WT 3RS-Tau static events were best fit to a two phase exponential function while Y18E 3RS-Tau was best fit to a one phase exponential function. Dynamic dwell times for both WT and Y18E 3RS-Tau were best fit to one phase exponential functions. Plots show 95% confidence bands as dotted lines.

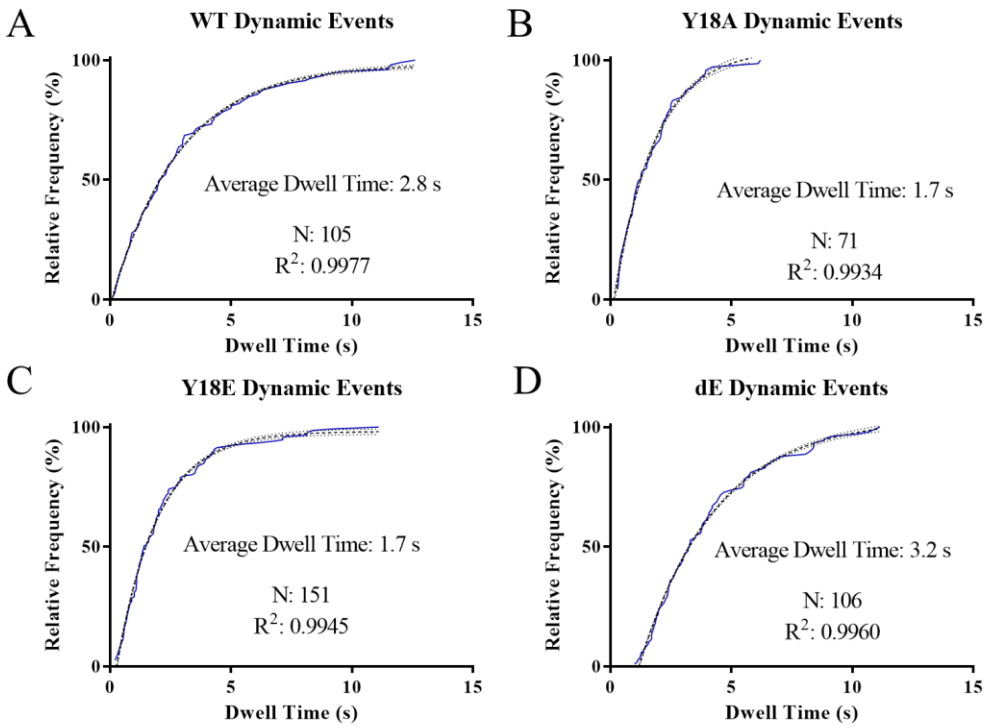

Figure S2.4 Cumulative frequency plots for WT, Y18A, Y18E and dE 3RS-Tau dynamic dwell times.

All dynamic dwell times were best fit to one phase exponential functions with 95% confidence bands as dotted lines. A) WT 3RS-Tau had an average dwell time of 2.8 s (R^2 = 0.9977). B) Y18A 3RS-Tau had an average dwell time of 1.7 s (R^2 = 0.9934). C) Y18E 3RS-Tau had an average dwell time of 1.7 s (R^2 = 0.9945). D) dE 3RS-Tau had and average dwell time of 3.2 s (R^2 = 0.9960). There were no notable changes in dynamic dwell times for WT and 3RS-Tau constructs.

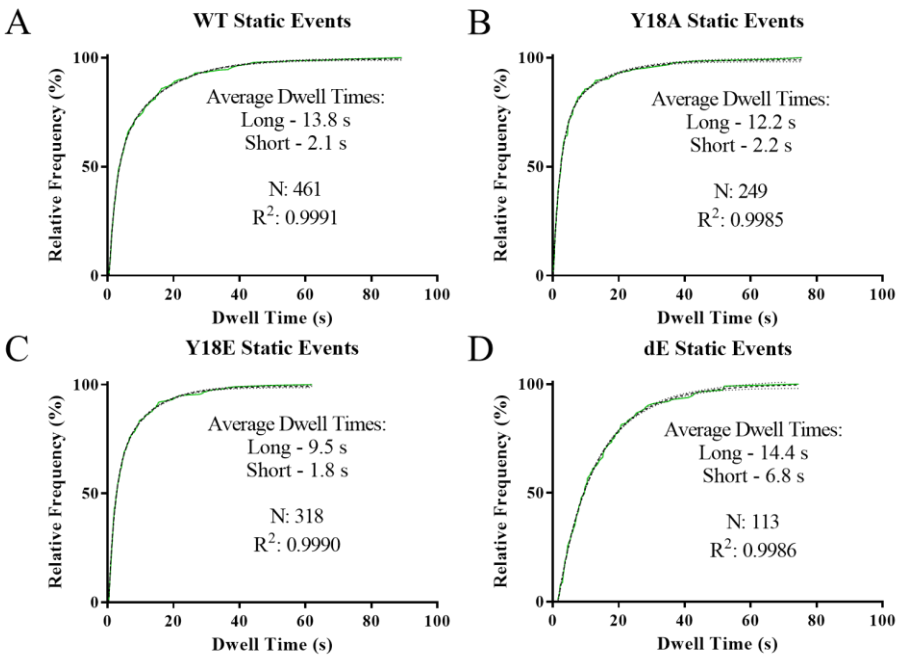

Figure S2.5 Cumulative frequency plots for WT, Y18A, Y18E and dE 3RS-Tau static dwell times.

All static dwell times were best fit to two phase exponential functions with 95% confidence bands as dotted lines. A) WT 3RS-Tau had a long dwell time of 13.8 s and a short dwell time of 2.1 s (R^2 = 0.9991). B) Y18A 3RS-Tau had a long dwell time of 12.2 s and a short dwell time of 2.2 s (R^2 = 0.9985). C) Y18E 3RS-Tau had a long dwell time of 9.5 s and a short dwell time of 1.8 s (R^2 = 0.9990). D) dE 3RS-Tau had a long dwell time of 14.4 s and a short dwell time of 6.8 s (R^2 = 0.9986). There were no notable changes in static dwell times (both long and short) for WT and 3RS-Tau constructs.

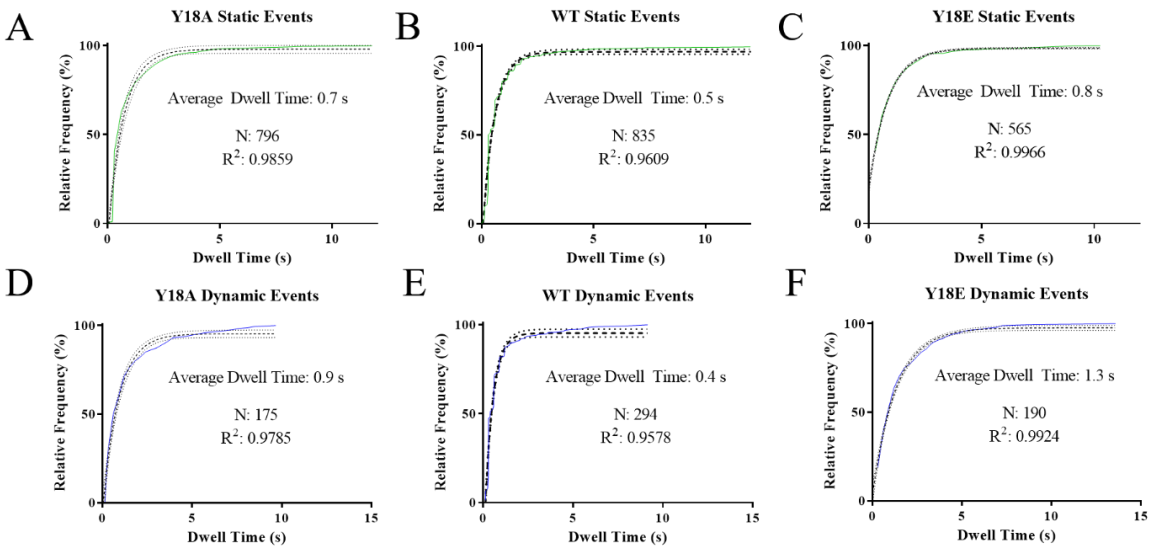

Figure S2.6 Cumulative frequency plots for Y18A and Y18E 3RS-Tau *ex vivo* dwell times.

All dwell times were best fit to single exponential functions with 95% confidence bands as dotted lines. A) Y18A 3RS-Tau had a static dwell time of 0.7 s (R^2 = 0.9859), (B) WT 3RS-Tau had a static dwell time of 0.5 s (R^2 = 0.9609) and C) Y18E 3RS-Tau had a static dwell time of 0.8 s (R^2 = 0.9966). D) Y18A 3RS-Tau had a dynamic dwell time of 0.9 s (R^2 = 0.9785), (E) WT 3RS-Tau had a dynamic dwell time of 0.4 s (R^2 = 0.9578) and (F) Y18E 3RS-Tau had a dynamic dwell time of 1.3 s (R^2 = 0.9924). Static and dynamic dwell times for Y18A, WT and Y18E 3RS-Tau are not appreciably different. However, these dwell times were shorter than those found in the *in vitro* assays due to the increased ionic strength found under physiological conditions.

Supplemental Movies

Movie S1 Sample motility assay for kinesin-1 in the presence of labeled WT 3RS-Tau. TIRF microscopy was used to observe the motility of Q-dot 655 labeled kinesin-1 on paclitaxel stabilized microtubules coated with Alexa 488 labeled WT 3RS-Tau (200 nM; 1:5, Tau:tubulin). 500 frames were recorded at 5 fps. Shown here at 15 fps. Arrows indicate runs. Data was analyzed using ImageJ as described.

Movie S2 Sample motility assay for kinesin-1 in the presence of unlabeled Y18E 3RS-Tau. We observed the motility of Qdot 655 labeled kinesin-1 on rhodamine labeled, paclitaxel stabilized microtubules coated with Y18E 3RS-Tau with the same ratio as above (Supplemental Movie S1). 500 frames were recorded at 5 fps. Shown here at 5 fps. Arrows indicate runs. Data was analyzed using ImageJ as described previously (Supplemental Movie S1).

Movie S3 Sample *in vitro* dynamics assay. Unlabeled WT 3RS-Tau at 200 nM (1:5; Tau:tubulin) spiked with Alexa 488 labeled WT 3RS-Tau (500 pM) behavior on rhodamine labeled microtubules. Arrows indicate binding events. 1000 frames were recorded at 10 fps shown here at 5 fps. Data was analyzed as described in the Methods sections.

Movie S4 Sample *in vitro* dynamics assay. Alexa 488 labeled Y18E 3RS-Tau was imaged at 1:3000 ratio with rhodamine labeled microtubules. Arrows indicate binding events. Data was acquired and analyzed as described in Supplemental Movie S3.

Movie S5 Sample *ex vivo* dynamics assay. Squid axoplasm was used to observe the behavior of Alexa 488 labeled Y18A 3RS-Tau on Alexa 568 labeled Y18A 3RS-Tau

coated microtubules. Images were collected at 3 fps. 100 frames were collected for each channel. Upward pointing arrows indicate dynamic events while downward pointing arrows indicate static events.

Movies can be found at http://www.molbiolcell.org.

CHAPTER 3: STRUCTURAL CHANGES UNDERLIE STATIC AND DIFFUSIVE TAU BINDING ON THE MICROTUBULE SURFACE

3.1 Abstract

The neuronal microtubule associated protein Tau is integral to the regulation of axonal transport and has been shown to carry out numerous functions including regulation of kinesin-1 cargo delivery. Kinesin-1 cargo transport is regulated through Tau participation in signaling cascades and direct modulation of motor movement. Our recent observation that N-terminal phosphorylation regulates Tau static-diffusive binding equilibrium and ability to modulate kinesin-1 motility, indicates that long range structural changes underlie static vs diffusive binding. This observation, coupled with solution and microtubule bound studies to determine Tau structure, led us to hypothesize that Tau binds the microtubule in multiple conformations. To address the challenge of observing structural change for a dynamically bound protein, we used total internal reflection fluorescence (TIRF) microscopy and alternating laser excitation (ALEX) to develop a three color single-molecule fluorescence resonance energy transfer (smFRET) assay. With this assay we have imaged the shortest isoform (3RS) of Tau in both the static and diffusive state on the microtubule surface. Using N- and C-termini dual labeled 3RS-Tau, we correlate changes in FRET efficiency with behavioral changes to demonstrate the efficacy of our approach. Our results show that the N- and C-termini interact while Tau is bound statically while this interaction is reduced in the diffusive state.

3.2 Introduction

Within the axon the molecular motor based movement of cargo along microtubule tracks (fast axonal transport, FAT) is regulated by complex signaling

pathways and many microtubule associated proteins (MAPs). The MAP Tau has been shown to carry out numerous functions during FAT including regulation of kinesin-1 based cargo delivery (Kanaan *et al.*, 2012). Tau mutations, aberrant isoform expression, and modification all lead to the disruption of FAT and are part of the pathology associated with Alzheimer's disease and other Tauopathies (Martin *et al.*, 2011; Ling, 2018). Six Tau isoforms are expressed in the adult brain and arise from alternative splicing of a single gene (Andreadis, 2005; Ballatore *et al.*, 2007). These isoforms differ based on the number of C-terminal microtubule binding repeats (MBRs, 3-4) and N-terminal acidic inserts (0-2) (Andreadis, 2005; Ballatore *et al.*, 2007). All isoforms have an N-terminal phosphatase activating domain (PAD) and proline rich region (PRR) (Margeat *et al.*; Ballatore *et al.*, 2007). All isoforms are subject to post-translational modifications including phosphorylation (Lee *et al.*, 2004; Andreadis, 2005; Ballatore *et al.*, 2007; Martin *et al.*, 2013b).

Tau regulates kinesin-1 based cargo transport through participation in signaling cascades and direct inhibition of motor motility (McVicker *et al.*, 2011; Kanaan *et al.*, 2012; Stern *et al.*, 2017). Tau's direct inhibition of kinesin-1 motility is well documented (Vershinin *et al.*, 2007; Dixit *et al.*, 2008; McVicker *et al.*, 2011; Hoeprich *et al.*, 2014). We have shown that the level of inhibition is dependent on Tau isoform and microtubule lattice structure (McVicker *et al.*, 2011). The shortest isoform, 3RS-Tau is more inhibitory to kinesin-1 on paclitaxel stabilized microtubules than the longest isoform 4RL-Tau (McVicker *et al.*, 2011). These isoform differences extend to Tau's behavior on the microtubule. Tau has been shown to bind the microtubule in a static-diffusive state equilibrium (Dixit *et al.*, 2008; Hinrichs *et al.*, 2012; McVicker *et al.*, 2014) which we

have demonstrated differs with isoform (McVicker *et al.*, 2014) and correlates with the isoform's ability to inhibit kinesin-1 motility (McVicker *et al.*, 2011; McVicker *et al.*, 2014). 3RS-Tau which is more inhibitory to kinesin-1 favors static binding on paclitaxel microtubules while the less inhibitory isoform 4RL-Tau is shifted towards diffusive binding (McVicker *et al.*, 2014).

The PAD has been shown to facilitate Tau's interaction with protein phosphatase 1 (PP1) which in turn regulates cargo delivery (Kanaan *et al.*, 2012). Fyn kinase mediated phosphorylation of tyrosine 18 (Y18), the last amino acid in the PAD, prevents the Tau-PP1 interaction (Kanaan *et al.*, 2012). The behavioral and functional differences we observed for 4RL- and 3RS-Tau led us to ask whether Tau's binding equilibrium could be regulated by the cell. We observed that phospho-mimetics of Y18 3RS-Tau induce a shift towards diffusive state binding and reduce both inhibition of kinesin-1 and Tau's affinity for the microtubule surface (Stern *et al.*, 2017). Phosphorylation within the MBRs and adjacent regions has been shown to reduce microtubule binding affinity (Biernat *et al.*, 1993) but our observation that this occurs with phosphorylation in the N-terminal projection region which does not bind the microtubule (Goode *et al.*, 2000; Stern *et al.*, 2017), indicates that long range structural changes may underlie static vs diffusive binding. Furthermore, phosphorylation mediated control of both Tau's signaling cascade participation and ability to inhibit kinesin-1 suggests a link between structural and functional regulation.

Recently, two dynamic folded conformations have been identified for Tau in solution (Jeganathan *et al.*, 2006; Elbaum-Garfinkle and Rhoades, 2012). While they differ in their finer details, they show that a folded conformation is stabilized by N- and

C-termini interactions (Jeganathan *et al.*, 2006; Elbaum-Garfinkle and Rhoades, 2012). To date structures underlying static and diffusive microtubule binding have not been observed. Initial transmission electron microscopy (TEM) studies of microtubule bound Tau showed no distinct bound structure (Cleveland *et al.*, 1977). Hirokawa *et al.* (1988) performed cryo-EM studies of densely packed Tau-microtubule pellets where Tau projections from the microtubule surface were clearly visible (Hirokawa *et al.*, 1988), but the microtubule bound portion of the protein could not be resolved. More recent cryo-EM work with Tau and MAP2c, found that both proteins bind along microtubule protofilament ridges (Al-Bassam *et al.*, 2002). Santarella *et al.* (2004) determined that Tau binds to α-tubulin subunits however, their study suggested that Tau binds both along and across protofilaments. Though these studies furthered our understanding of the Tau-microtubule interaction, they also show that Tau decorated microtubules appear to have a 'fuzzy' coat (Al-Bassam *et al.*, 2002; Santarella *et al.*, 2004). This 'fuzziness' indicates that the portions of Tau that do not interact with the microtubule surface are free to adopt multiple conformations (Santarella *et al.*, 2004) that cryo-EM techniques cannot resolve. This is further supported by recent nuclear magnetic resonance (NMR) studies which suggest that when Tau is bound to the microtubule local folding occurs in MBR inter-repeat regions (Kadavath *et al.*, 2015). These regions are connected by a flexible linker indicating that Tau may have the ability to adopt multiple conformations while bound to the microtubule (Kadavath *et al.*, 2015).

We propose a model of dynamic binding where Tau's structure while statically bound is distinct from its diffusively bound structure. These structural changes create a conformational equilibrium underlying a behavioral equilibrium. To address the

challenge of observing structural change for a dynamically bound protein, we have developed a three color single-molecule fluorescence resonance energy transfer (smFRET) (Roy *et al.*, 2008) assay. This assay allows us to image dual labeled Tau interacting with labeled microtubules. Using total internal reflection fluorescence (TIRF) microscopy and alternating laser excitation (ALEX) (Kapanidis *et al.*, 2005), we have imaged both statically and diffusively bound Tau. From these data we can correlate changes in FRET efficiency with behavioral changes. Here we demonstrate the efficacy of our approach using N- and C-termini dual labeled 3RS-Tau. Our results show that the N- and C-termini interact while Tau is bound in the static state and this interaction is reduced in the diffusive state.

3.3 Methods

All work was done with 1X Brinkley's Reassembly Buffer 80 (BRB80; 80 mM PIPES, 1 mM EGTA, 1 mM $MgCl_2$, pH 6.9 at room temperature) unless otherwise noted (Stern *et al.*, 2017).

Tau Construct Generation Our N&C 3RS-Tau smFRET construct was generated by introducing the following changes: T17C, C322I, S346C using the QuikChange II XL Site-Directed Mutagenesis Kit (Agilent Technologies, Santa Clara, CA) (Figure 3.1A). Similarly, N 3RS-Tau and C 3RS-Tau constructs were generated using the QuikChange Mutagenesis Kit to introduce cysteines at T17 and S346 respectively in a C322I construct (Figure 3.1A). WT 3RS-Tau and all Tau constructs were expressed in BL21-CodonPlus(DE3)-RP *Escherichia coli* cells (Stratagene, La Jolla, CA) and purified using Q and SP Sepharose (Sigma-Aldrich, St. Lois, MO) affinity column chromatography as previously described (McVicker *et al.*, 2011; McVicker *et al.*, 2014). After purification,

samples were dialyzed against 1X BRB80. Protein concentrations were determined using the bicinchonic acid (BCA) assay (Pierce, Rockford, IL) and WT 3RS-Tau standards. SDS PAGE gels (Bio-Rad, Hercules, CA) were used to validate concentrations.

Tau Construct Labeling *smFRET Construct* N&C 3RS-Tau was dual labeled with the FRET pair Alexa Fluor® 488/647 (Alexa Fluor® 488 C_5 Maleimide and Alexa Fluor® 647 C_2 Maleimide; Invitrogen Molecular Probes, Carlsbad, CA). N&C 3RS-Tau was incubated in 4M guanidine hydrochloride (GndHCl), 1X phosphate-buffered saline (PBS) pH 7.4 (diluted from 10X PBS pH 7.4; Gibco® by Life Technologies, Grand Isle, NY) and 10 fold molar excess dithiothreitol (DTT) for 10 min at 37 ^{o}C. Following this incubation, a 2 ml 7K MWCO Zeba™ spin desalting column (Peirce, Rockford, IL) was used to remove reducing agents. N&C 3RS-Tau was then incubated with 10 fold molar excess of Alexa Fluor® 647 in the presence of 1 mM sodium bicarbonate (to raise the pH above 7 and improve labeling) for 24 hr in the dark at room temperature. Two fold molar excess Alexa Fluor® 488 was then added for an additional 24 hr incubation. Excess fluorophore was removed by three rounds of dialysis against 1X BRB80. The protein concentration was determined using both the Modified Lowry Assay (Peirce, Rockford, IL) and densitometry performed on SDS PAGE gels. Labeling efficiency was determined as described previously (Stern *et al.*, 2017) using the extinction coefficients Alexa Fluor® 488 – 71,000 $cm^{-1}M^{-1}$ at 493 nm and Alexa Fluor® 647 – 270,000 $cm^{-1}M^{-1}$ at 652 nm. Labeling efficiency was Alexa 488: 26%, Alexa 647: 79%.

WT, N and C 3RS-Tau Constructs WT 3RS-Tau and both Tau constructs were singly labeled with Alexa Fluor® 647 and 488. For Alexa Fluor® 647 labeling was carried out following the method detailed for dual labeling except that there was no 24 hr Alexa

Fluor® 488 incubation. For Alexa Fluor® 488, labeling was carried out at as detailed previously (McVicker *et al.,* 2014; Stern *et al.,* 2017). Briefly, constructs were incubated with 10 fold molar excess DTT for 2 hr at room temperature before the DTT was removed with a desalting column. Protein was then incubated with 5 fold molar excess fluor at room temperature before excess fluor was removed with a desalting column. Protein concentration and labeling efficiency was determined as described previously (Stern *et al.,* 2017) using the extinction coefficients listed above. Labeling efficiency was Alexa 488 – WT: 42%, N: 50%, C: 75%; Alexa 647 – WT: 60 %, N: 34%, C: 47 %.

High, Intermediate and Low FRET Oligomer Design The R_0 for the FRET pair Alexa 488/647 was calculated using the equation:

1:

$$R_0 = 9.78 \times 10^3 (K^2 n^{-4} \Phi_D J(\lambda))^{1/6}$$

Where K^2 is the orientation factor (assumed to be 2/3) (Shrestha *et al.*, 2015), ϕ_D is quantum yield of donor (0.92) (Johnson, 2010) and $J(\lambda)$ is the overlap integral of donor emission and acceptor excitation spectra defined as:

2:

$$J(\lambda) = \int \varepsilon_A(\lambda) F_D(\lambda) \lambda^4 d\lambda$$

Where ε_A is the acceptor extinction coefficients and $F_D(\lambda)$ is the normalized donor emission spectrum both measured using a fluorimeter to determine the excitation and emission spectra of Alexa 488 and 647 at 200 nM (Supplemental Fig. S2). The R_0 was determined to be 52.7 Å.

Based on the R_0 DNA oligomers were developed for High, Intermediate and Low FRET states. The High FRET control oligomer was designed as follows: 5’-

/Alexa488/TCCCACCTGTCCATGCCAGCCT/Biotin/-3’ and 5’-AGGCTGGCATGGACAGGTGGGA/Alexa647/-3’ (Integrated DNA Technologies, Coralville, IA) with a FRET pair spacing of 24 Å. The Low FRET control oligomer was designed using the same sequence for the High FRET oligomer as follows: 5’-/Alexa488/TCCCACCTGTCCATGCCAGCCT/Biotin/-3’ and 5’/Alexa647/AGGCTGGCA TGGACAGGTGGGA-3’ (Integrated DNA Technologies, Coralville, IA) with a FRET pair spacing of 73 Å. The Intermediate FRET control was designed with the sequence: 5’/Alexa488/AGGCTGGCATGGACGT/Biotin/-3’ and 5’-/Alexa647/ACGTCCATG CCAGCCT-3’ (Integrated DNA Technologies, Coralville, IA) with a FRET pair spacing of 53 Å.

Tubulin Purification and Labeling Tubulin was purified as previously described from bovine brain obtained from Vermont Livestock & Slaughter (Ferrisburgh, VT) (McVicker *et al.*, 2014). For imaging in our three color system, purified tubulin was labeled with Alexa Fluor® 405 using methods developed by Hyman *et al.* (Hyman *et al.*, 1991). Purified tubulin (20-25 mg) was polymerized at 37 ºC for 30 min. Following polymerization, microtubules were layered on a warm high cushion buffer (0.1 M NaHEPES (pH 8.6) (Sigma-Aldrich, St. Lois, MO), 1 mM $MgCl_2$, 1 mM EGTA, 60% (v/v) glycerol) and pelleted at 40,000 rpm, 45 min, 35 ºC in an Optima™ TLX Ultracentrifuge (Beckman, Pasadena, CA). The supernatant was aspirated and the cushion surface was washed with warm label buffer (0.1 M NaHEPES (pH 8.6), 1 mM $MgCl_2$, 1 mM EGTA, 40% (v/v) glycerol). The cushion was then aspirated and the pellet resuspended in warm label buffer. The resuspended microtubules were incubated with 10 fold molar excess Alexa Fluor® 405 for 1 hr at 37 ºC with vortexing.

To quench labeling, an equal volume of stop buffer (2X BRB80, 100 mM L-Glutamic acid potassium salt monohydrate (K-glutamate; Sigma-Aldrich, St. Lois, MO), 40% (v/v) glycerol) was added to the microtubule/dye mixture and incubated for 5 min at 37 ^{o}C. The quenched mixture was placed on a warm low cushion buffer (60% (v/v) glycerol, 1X BRB80) and centrifuged at 80,000 rpm, 35 ^{o}C for 20 min. The supernatant was discarded and warm 1X BRB80 (37 ^{o}C) was used to wash the cushion before the pellet was resuspended in ice cold 1X depolymerization buffer (50 mM K-glutamate, 5 mM $MgCl_2$, pH 7.0) and incubated for 30 min at 4 ^{o}C. Depolymerized tubulin was centrifuged at 80,000 rpm, 2 ^{o}C for 10 min. Supernatant was recovered. 1X BRB80, 4 mM $MgCl_2$ and 1 mM GTP were added to the supernatant before the mixture was incubated on ice for 3 min. This mixture was then incubated at 37 ^{o}C for 2 min before ½ volume warm glycerol (33% v/v) was added. The solution was incubated for a further 30 min at 37 ^{o}C. Polymerized tubulin was layered onto warm low cushion buffer and pelleted at 80,000 rpm, 20 min, 37 ^{o}C. The resulting microtubule pellet was resuspended in ice cold 1X BRB80 and incubated at 4 ^{o}C for 30 min. Depolymerized tubulin was centrifuged a final time at 80,000 rpm, 10 min, 2 ^{o}C. Protein concentration was determined using Beer-Lambert's law and the tubulin extinction coefficient of 110,000 $cm^{-1}M^{-1}$ at 280 nm. Labeling efficiency was determined in the same manner using the Alexa 405 extinction coefficient of 35,000 $cm^{-1}M^{-1}$ at 401 nm. Tubulin concentration was validated using SDS PAGE gels.

Slide Coating and Chamber Construction *Biotin-PEG coating* Coverslips (Marienfeld High Precision Microscope Cover Glass No. 1.5H (tol. ± 0.5 µm), Azer Scientific, Morgantown, PA) were methanol washed and plasma cleaned as previously described

(McVicker *et al.*, 2014; Stern *et al.*, 2017). Cleaned slides were then incubated with an amino silane mixture (94 % methanol, 5 % acetic acid and 1 % N-(2-aminoethyl)-3-aminopropyltrimethoxysilane (MilliporeSigma, Billerica, MA)) for 15 min before a 30 sec sonication and additional 15 min incubation (Joo and Ha, 2012b). Slides were rinsed in ddH_2O and dried. Following this, slides were incubated with a PEG solution (0.57 mM mPEG-Biotin (Laysan Bio Inc, Arab, AL), 22 mM mPEG-SC (Laysan Bio Inc, Arab, AL) in 0.1 M $NaHCO_3$ (Sigma-Aldrich, St. Lois, MO) per slide) overnight in a humidifying chamber (Joo and Ha, 2012b). Slides were then washed with ddH_2O and stored at -20 ^oC until used. Flow chambers were constructed on the day of the experiment using double sided tape.

Silane-PEG coating Glass coverslips were silane-PEG coated as previously described (Stern *et al.*, 2017). Briefly, methanol washed slides were plasma cleaned and incubated in a silane mixture (97% toluene (Sigma-Aldrich, St. Lois, MO), 2% 2-methoxy(polyethyleneoxy)propyltrimethoxysilane (Gelest Inc., Morrisville, PA), and 1% butylamine (Acros Organics, New Jersey, USA)) with flowing nitrogen gas for 90 min (Lowndes and Nelson, 2013). Coverslips were then washed in toluene, dried and cured with flowing nitrogen gas for 30 min. Flow chambers were constructed using ARTUS shims (ARTUS, Eaglewood, NJ) and Norland optical adhesive (Norland Products, Cranbury, NJ) as previously described (Stern *et al.*, 2017).

Microtubule Polymerization *Paclitaxel stabilized* Purified, unlabeled tubulin was clarified by ultracentrifugation (20 min, 95,000 rpm, 4^oC). Clarified tubulin was mixed with Alexa Fluor® 405 labeled tubulin at a 1:7 (labeled:unlabeled) ratio and 1 mM GTP (Sigma-Aldrich, St. Lois, MO). Microtubules were polymerized for 20 min at 37^oC

(McVicker *et al.*, 2014; Stern *et al.*, 2017). Following polymerization, microtubules were stabilized with 20 µM paclitaxel (paclitaxel; Sigma-Aldrich, St. Lois, MO). Post-clarification tubulin concentration was calculated using the tubulin extinction coefficient of 110,000 $cm^{-1}M^{-1}$ at 280 nm.

GMPCPP stabilized Clarified tubulin was mixed with Alexa Fluor® 405 labeled tubulin in a 1:7 (labeled:unlabeled) ratio and 20 µM guanosine-5'-[(α,β)-methyleno]triphosphate (GMPCPP; Jena Bioscience, Jena, Germany). Microtubules were polymerized by incubating small volumes of the mixture stepwise at 37 ^{o}C with 20 min incubations between additions (McVicker *et al.*, 2014). Post clarification tubulin concentration was determined as described above.

DNA Oligomer Assay 1X BRB80 (pH 7.4 w/KOH) was used to prepare all assay buffers. Chambers were washed with 1 mg/mL biotinylated BSA (Sigma-Aldrich, St. Lois, MO) for 5 minutes. Chambers were then incubated with one chamber volume 0.2 mg/mL streptavidin (Sigma-Aldrich, St. Lois, MO) (diluted in 1 mg/mL BSA (Sigma-Aldrich, St. Lois, MO)) for 5 minutes before one chamber volume of 50 pM desired DNA oligomer (diluted in 1 mg/mL biotinylated BSA) was flown in for 5 minutes. Chambers were washed with 2X chamber volume 1mg/mL biotinylated BSA to remove non-adherent oligomers. To prevent drying, chambers were sealed with grease. An inverted Eclipse Ti Microscope (Nikon, Melville, NY) with a 100X PlanApo objective lens (1.49 NA) and auxiliary 1.5X magnification and two iXON Ultra EMCCD cameras (Andor, Belfast, N-IRL) running NIS Elements v4.51 (Nikon, Melville, NY) were used to perform TIRF microscopy with alternating laser excitation. Alexa 488/647 labeled oligomers were imaged by alternating exposure with 640 nm and 488 nm argon lasers

and 525/50 and 655 LP emission filters. Three hundred frames were collected at room temperature at 0.2 s, 0.11 μm/pixel.

Behavioral and Intermolecular FRET Assays For both assays, washes and incubations were performed with BRB80+OS (BRB80 supplemented with a previously published oxygen scavenging system (McVicker *et al.*, 2011)) supplemented with 20 μM paclitaxel and 1.5 mM (±)-6-Hydroxy-2,5,7,8-tetramethylchromane-2-carboxylic acid (Trolox) (Sigma-Aldrich, St. Lois, MO) (Joo and Ha, 2012a). Silanized flow chambers were incubated with monoclonal anti-β III (neuronal) tubulin antibodies (Sigma-Aldrich, St. Lois, MO) at 33 μg/mL for 5 min followed by a 5 min 2X chamber volume wash with 2 mg/mL BSA (Sigma-Aldrich, St. Lois, MO) (McVicker *et al.*, 2014).

Behavioral Assay Chambers were incubated for 12 min with paclitaxel stabilized, Alexa 405 labeled microtubules diluted to 1 – 1.5 μM in 333 – 500 pM N, C or WT 3RS-Tau constructs. Finally, chambers were washed with 333 - 500 pM N, C or WT 3RS-Tau for 2-4 min to remove non-adherent microtubules. All Tau and microtubule dilutions were made in warm (37^{o}C) BRB80+OS with paclitaxel and Trolox. Imaging was done using the system described for the DNA oligomer assay. Alexa 405 labeled tubulin was excited and imaged with a 405 nm argon laser and a 450/50 emission filter. For microtubules, 10 frames were collected at room temperature at 0.3 s, 0.11 μm/pixel. Tau was imaged using the laser and filter combinations described for the DNA oligomers. 300 frames were collected at room temperature at 0.2 s, 0.11 μm/pixel.

Intermolecular smFRET Assay This assay was prepared using the buffers and chamber preparation described for the behavioral assay above. Chambers were incubated for 12 min with paclitaxel stabilized, Alexa 405 labeled microtubules diluted to a final

concentration of 1-1.5 uM. An equal mixture of singly labeled (Alexa 488 and 647) N and C 3RS-Tau was flown into the chamber at 1 nM (20X the concentration used for smFRET experiments) before imaging. Imaging was carried out using the system detailed in the DNA oligomer assay and data was collected as for the behavioral assay.

smFRET Assay For imaging, washes and incubations were performed with BRB80+OS (BRB80 supplemented with a previously published oxygen scavenging system (McVicker *et al.*, 2011)) supplemented with 1.5 mM (±)-6-Hydroxy-2,5,7,8-tetramethylchromane-2-carboxylic acid (Trolox) (Sigma-Aldrich, St. Lois, MO) (Joo and Ha, 2012a). Silanized flow chambers (McVicker *et al.*, 2014) were incubated with monoclonal anti-β III (neuronal) tubulin antibodies (Sigma-Aldrich, St. Lois, MO) at 33 µg/mL for 5 min followed by a 5 min 2X chamber volume wash with 2 mg/mL BSA (Sigma-Aldrich, St. Lois, MO). Chambers were then incubated for 12 min with paclitaxel or GMPCPP stabilized, Alexa 405 labeled microtubules diluted to 1.5 µM in 50 pM dual labeled N&C 3RS-Tau. Finally, chambers were washed with 50 pM dual labeled N&C 3RS-Tau for 2-4 min to remove non-adherent microtubules. All Tau and microtubule dilutions were made in warm (37^{o}C) BRB80+OS with Trolox. Imaging was done using the system described for the DNA oligomer assay. Alexa 405 labeled tubulin was excited and imaged with a 405 nm argon laser and a 450/50 emission filter. For microtubules, 10 frames were collected at room temperature at 0.3 s, 0.11 µm/pixel. Tau was imaged using the laser and filter combinations described for the DNA oligomers. 300 frames were collected at room temperature at 0.2 s, 0.11 µm/pixel.

Data Analysis *Behavioral Assay* Events were tracked using the MTrackJ plugin for FIJI if they lasted more than three frames, the signal remained within a snap range of 19 x 19

pixels from one frame to the next (snap range chosen based on maximum diffusive range of a Tau protein (Konzack *et al.,* 2007)) and the event began and ended on one microtubule. Tracks were measured and the points were then exported to Excel. These files were analyzed using a custom MATLAB (R2014b) sliding window analysis script (Rehan Ali, Unpublished) to calculate mean squared displacement. The mean squared displacement was used to separate events as either static or diffusive. Diffusion coefficients and alpha values were calculated for diffusive events (Supplemental Table S1).

DNA Oligomers Images were analyzed using FIJI (Schindelin *et al.,* 2012). Dual labeled oligomers were identified using kymographs for the donor and acceptor channels generated with the Multi Kymograph function. Co-localized events were further analyzed. Dual labeled events were tracked using MTrackJ from the ImageScience plugin (v3.0.0; Eric Meijering) for FIJI. Tracks were measured in all channels and track points were exported to Excel. Points in Excel were further analyzed using MATLAB (R2014b) to track the event frame by frame within a 3 x 3 pixel area around the central x,y position provided by the track (Rehan Ali, Unpublished). Local background subtraction was performed before the average intensity of the event in each frame was calculated. Average intensities were used to calculate the constants χ and γ using the following equations:

3:
$$\chi = {I_D^A}\Big/{I_D^D}$$

Where χ is the bleed-through of the donor (I_D^D) into the energy transfer channel (I_D^A) was calculated upon acceptor photo-bleaching.

4:

$$\gamma = {\Delta I_A^A}\Big/{\Delta I_D^D}$$

Where **γ** is the sensitivity of the system when detecting the acceptor (I_A^A) versus the donor (I_D^D) fluorophore was calculated upon acceptor photo-bleaching.

Donor/acceptor fluorophore stoichiometry (***S***) and efficiency of energy transfer (***E***) for each event were calculated as follows:

5:

$$S = \frac{I_D^D + (I_D^A - \chi \times I_D^D)}{I_D^D + (I_D^A - \chi \times I_D^D) + I_A^A}$$

6:

$$E = \frac{(I_D^A - \chi \times I_D^D)}{(I_D^A - \chi \times I_D^D) + \gamma \times I_D^D}$$

Intermolecular FRET Assay Alexa 488 and 647 binding events that overlapped or occurred close to each other, were identified by generating kymographs as for oligomer analysis. Using the MTrackJ plugin, events were tracked in their respective channels (data shown from events tracked in the donor channel). Upon measurement of these tracks in each channel, the points were exported to Excel for further analysis with a custom MATLAB script as for the behavioral assay. The x,y position associated with each track was used to identify the event within the image field for calculation of the corrected intensity as described for the DNA oligomer. These corrected intensities were then used to calculate average ***S*** and ***E*** for each event.

smFRET Assay Dual labeled events were identified as described for oligomer analysis. Identified dual labeled events were further analyzed using the MTrackJ plugin. Events lasting longer than three frames were tracked using a snap range of 19 x 19 pixels with bright centroid tracking. Tracks were measured in each channel and were scored static or

diffusive based on their maximum distance to start as described in Stern *et al.*, (2017). Points were exported to Excel for further analysis.

The x, y positions provided by the event points were used to identify events in the image field so that the average corrected intensity of the event in each channel from frame to frame could be calculated as detailed for oligomer analysis. The average corrected intensities for static and diffusive events were then used to calculate average ***S*** and ***E*** for each event using the equations detailed above.

Statistics Percentages for static and diffusive populations were presented as described for the behavioral assay in chapter two. Briefly, the standard deviation shown is the spread in the static and diffusive populations for two experiments.

Average ***S*** and ***E*** calculations for high, intermediate and low DNA oligomer constructs are based on the averages of 8 events for each oligomer collected over three experiments. For intermolecular FRET, average ***S*** and ***E*** calculations are for averages of 6 events collected over two experiments. Average ***S*** and ***E*** calculations for Tau are based on averages of 12 events collected over two experiments for both paclitaxel and GMPCPP stabilized microtubules. The standard deviation reported for average ***S*** and ***E*** is the deviation for total events. Significance was determined for all ***S*** and ***E*** calculations using a T-test with Welch's correction assuming different standard deviations for static and diffusive events.

3.4 Results

Tau's behavior is not affected by introduction/removal of cysteine residues or labeling in the N- and C-termini. To generate our smFRET construct for dual labeling (N&C 3RS-Tau), we mutated 3RS-Tau's naturally occurring cysteine to an isoleucine (C322I) and

introduced cysteines in the N- and C-termini (T17C and S346C) (Figure 3.1A). In order to ensure that these changes did not affect Tau's behavior while bound to the microtubule surface, we generated single cysteine constructs (T17C/C322I and C322I/S346C; Figure 3.1A). These single cysteine constructs were labeled with either Alexa 488 or 647. Using TIRF microscopy, we observed Alexa 488 and 647 labeled WT, N and C 3RS-Tau bound to paclitaxel stabilized, Alexa 405 labeled microtubules (Figure 3.1B and 3.2A). Behavioral assays performed for donor (Alexa 488) labeled N 3RS-Tau (74 ± 4 % static) and C 3RS-Tau (66 ± 5 % static) revealed no significant differences in binding equilibrium when compared to WT 3RS-Tau (72 ± 5 % static; $P > 0.05$) or to each other ($P > 0.05$) (Figure 3.2B and Supplementary Table S3.1). We also observed that labeling with acceptor (Alexa 647) did not have a significant effect ($P > 0.05$) on binding equilibrium when comparing N 3RS-Tau (67 ± 5 % static) to C 3RS-Tau (60 ± 5 % static) or comparing both to WT 3RS-Tau (65 ± 5 % static; $P > 0.05$) (Figure 3.2B and Supplemental Table S3.1). Dwell times, diffusion coefficients and alpha values determined for WT, N, and C 3RS-Tau did not change with fluorophore (Supplementary Table S3.1).

DNA oligomer constructs demonstrate imaging of high, intermediate and low FRET states and allow calculation of γ *and* χ*.* Based on the R_0 (52.7 Å) calculated for our FRET pair (Alexa 488/647), we designed DNA oligomers to measure high (23 Å, $\boldsymbol{E} > 0.9$), intermediate (53 Å, $\boldsymbol{E} = 0.5$) and low (73 Å, $\boldsymbol{E} < 0.2$) FRET states (Supplemental Fig. 3.1). These oligomers were imaged using TIRF microscopy and ALEX to test the system's ability to image both fluorophores in these different FRET states. Upon acceptor photo-bleaching (Figure 3.3), χ (donor bleed-through into the acceptor channel) was

calculated to be 0.021 while γ (differences in detecting donor and acceptor fluorophores) was calculated to be 0.83. These constants were used to correct all ***S*** and ***E*** calculations. For the high FRET oligomer we measured an average ***S*** of 0.57 ± 0.09 and an average ***E*** of 1.1 ± 0.23 (24 Å) (Figure 3.4, Supplementary Fig. 3.1). The intermediate FRET oligomer had average ***S*** of 0.63 ± 0.13 and an average ***E*** of 0.52 ± 0.11 (52 Å) (Figure 3.4, Supplementary Fig. S3.1). For the low FRET oligomer, we measured an average ***S*** of 0.52 ± 0.09 and an average ***E*** of 0.14 ± 0.11 (71 Å) (Figure 3.4, Supplementary Fig. S3.1). These results demonstrate that our system is capable of accurately detecting changes in fluorophore intensity that correspond to different FRET states.

Intermolecular FRET does not occur at the smFRET imaging concentration. Though our smFRET imaging concentration (50 pM) results in Tau-microtubule ratio of 1:30,000 (based on a 1.5 μM microtubule imaging concentration), which greatly reduces possible Tau-Tau interactions on the microtubule surface, interactions may still occur. Such interactions could result in intermolecular FRET leading to false measurements with our dual labeled population. To determine if intermolecular FRET occurs, we imaged a mixture (1:1:1) of Alexa 488 and Alexa 647 singly labeled WT, N and C 3RS-Tau. Using TIRF microscopy and ALEX, we imaged N and C 3RS-Tau at 1 nM (20X smFRET assay concentration). Alexa 488 and 647 labeled binding events that overlapped or occurred in close proximity (Figure 3.5A) were tracked using MTrackJ. Using MATLAB, intensity values associated with these events were used to calculate both ***S*** and ***E***. We observed that even when binding events overlapped, they had an ***E*** of 0.04 ± 0.23 (Figure 3.5B) indicating that we were not able to observe intermolecular FRET at 1.5 μM Tau making it unlikely that intermolecular FRET is occurring at lower concentrations.

3RS-Tau's N- and C- termini interact in the static state on paclitaxel and GMPCPP stabilized microtubules but this interaction is reduced in the diffusive state. Having completed our control experiments, we imaged the behavior of dual labeled (Alexa 488/647) N&C 3RS-Tau on Alexa 405 labeled, paclitaxel stabilized microtubules. Within the dual labeled preparation, only ~20 % of the Tau molecules were labeled with both the donor and the acceptor. In order to identify dual labeled events for further analysis, we imaged using TIRF microscopy with ALEX.

In addition to separating N&C 3RS-Tau behavior into static and diffusive binding events as described in the methods, dual labeled tracks were used to calculate the frame by frame intensity values (I_A^A , I_D^A , I_D^D) needed to determine average $\boldsymbol{S}$ and $\boldsymbol{E}$ for static and diffusive binding events.

As we have previously shown, 3RS-Tau favors static binding on paclitaxel stabilized microtubules (McVicker *et al.*, 2014; Stern *et al.*, 2017). To increase our chances to observe diffusive behavior, we imaged N&C 3RS-Tau on GMPCPP microtubules (Figure 3.6) where it has been shown that 3RS-Tau's binding equilibrium is shifted towards the diffusive state (McVicker *et al.*, 2014). We found that for both lattice structures, the N- and C-termini interact closely in the static state (Figure 3.6&3.7) while this interaction is reduced in the diffusive state (Figure 3.6&3.7).

3.5 Discussion

Over the last three decades cryo-EM, NMR and single molecule imaging have begun to elucidate Tau structure and function on the microtubule surface (Hirokawa *et al.*, 1988; Al-Bassam *et al.*, 2002; Santarella *et al.*, 2004; Jeganathan *et al.*, 2006; Elbaum-Garfinkle and Rhoades, 2012; Kadavath *et al.*, 2015). Cryo-EM studies hint at

the dynamic nature of Tau binding (Al-Bassam *et al.*, 2002). However, the static-diffusive state binding equilibrium was not observed until recent TIRF studies were performed (Hinrichs *et al.*, 2012). If distinct structural changes occur on the microtubule surface, they could not be observed with NMR, cyro-EM and solution based FRET (Hirokawa *et al.*, 1988; Al-Bassam *et al.*, 2002; Santarella *et al.*, 2004; Jeganathan *et al.*, 2006; Elbaum-Garfinkle and Rhoades, 2012; Kadavath *et al.*, 2015). In the case of NMR and cryo-EM, averages of the microtubule associated portion of the protein were observed but no structure could be observed away from the microtubule surface (Al-Bassam *et al.*, 2002; Santarella *et al.*, 2004; Kadavath *et al.*, 2015). Solution based FRET experiments revealed a folded conformation for Tau (Jeganathan *et al.*, 2006; Elbaum-Garfinkle and Rhoades, 2012) but these assays could not be used to image structural differences between static and diffusive binding on the microtubule surface. Though these studies did not focus on the structural changes that underlie static versus diffusive binding, along with our own observations of Tau N-terminal phosphorylation mediated modulation of kinesin-1 motility (Stern *et al.*, 2017), they led us to hypothesize that Tau binds the microtubule surface in multiple conformations which are regulated by Tau N- and C-termini interactions and that global conformational change underlies static and diffusive microtubule binding. In order to observe potential structural changes on the microtubule surface, we developed a three color smFRET TIRF assay using ALEX to image Alexa 488/647 labeled Tau on Alexa 405 labeled microtubules.

Based on our hypothesis, any conformational change would be most noticeable in the interaction between the N- and C-termini. Therefore we chose N&C 3RS-Tau as a first test of our system. Our experimental procedure allows us to correlate behavioral

changes with changes in energy transfer efficiency for static and diffusive events. Our DNA oligomer controls demonstrate that we are able to measure energy transfer efficiencies between 24 Å and 71 Å (Figure 3.3&3.4). Our results report the average interactions of N&C 3RS-Tau in the static and diffusive state (Figure 3.6&3.7) however, other structural changes exist may occur.

Our smFRET experiments show that the N- and C-termini interact closely in the static state on both paclitaxel and GMPCPP stabilized microtubules while the interaction is reduced in the diffusive state (Figure 3.8). This interaction suggests that Tau binds the microtubule surface in a folded conformation which is more compact in the static state. The more open confirmation that underlies diffusive binding may be the result of Tau interactions with tubulin C-terminal tails (CTT). It has previously been shown that diffusive behavior is dependent on CTT (Hinrichs *et al.*, 2012). On subtilisin treated microtubules the frequency of binding is reduced and those events that do occur are predominantly static (Hinrichs *et al.*, 2012). This supports work demonstrating that the Tau-microtubule interaction is partially dependent on the CTT and requires interactions between the CTT and C-terminal residues of Tau (Al-Bassam *et al.*, 2002; Hinrichs *et al.*, 2012; Di Maïo *et al.*, 2014). Static binding is then the result of the folded conformation's inability to interact with the CTT due to shielding of the C-terminal region.

Previous work by our group demonstrates that static Tau is more inhibitory to kinesin-1 motility than diffusive Tau (McVicker *et al.*, 2011; Stern *et al.*, 2017). A folded conformation preventing Tau C-terminal interactions with the CTT would allow for more stable lattice interactions promoting static binding. This would in turn allow Tau to modulate kinesin-1 run-length. The phosphorylation mediated shift towards diffusive

binding would result from disruption of N- and C-termini interactions leading to an equilibrium shift. In addition to regulating kinesin-1 motility, Tau participates in signaling cascades governing cargo delivery (Morfini *et al.*, 2002; LaPointe *et al.*, 2009; Kanaan *et al.*, 2012). Phosphorylation of Y18 which facilitates a diffusive state shift, has also been shown to prevent Tau from participating in signaling cascades (Morfini *et al.*, 2002; LaPointe *et al.*, 2009; Kanaan *et al.*, 2012). Therefore, the more stable lattice interactions found in the static state could facilitate Tau involvement in signaling. However, the more open conformation of the diffusive state would be more accessible for signaling though this would be phosphorylation dependent. Based on this reasoning Tau participation in signaling cascades could occur in either the static or diffusive state but, protein-protein interactions might further alter Tau conformation on the microtubule surface. Hirokawa *et al.* (1988) observed an open, extended N-terminal in cryo-EM micrographs of densely packed Tau-microtubule pellets. It has been shown that Tau bundles microtubules potentially through N-terminal/N-terminal interactions (Chen *et al.*, 1992; Rosenberg *et al.*, 2008; Choi *et al.*, 2017). This would lead to the extended N-terminal projections observed by Hirokawa *et al.* (1988). We do not know how Tau-Tau interactions or other binding partners would further affect Tau on the microtubule surface.

Further work must be done with other smFRET constructs to determine the overall structure of Tau on both paclitaxel and GMPCPP stabilized microtubules. Additionally, Tau is a heavily post translationally modified protein (Martin *et al.*, 2011). As we have previously demonstrated, phosphorylation plays a role in regulating Tau's behavior and function on the microtubule surface (Stern *et al.*, 2017). It is not hard to see

how disease state modifications to Tau would affect its bound structure and therefore its function beginning at early disease development time points. Future work with Tau will allow us to understand how disease and non-disease state phosphorylation events (such as Y18 phosphorylation) may affect Tau's bound structure and whether the structural changes we have observed *in vitro* occur *in vivo* under normal and disease state conditions. This work highlights the need for continued study of factors which regulate Tau's static-diffusive microtubule binding equilibrium.

3.6 Acknowledgements

This work was supported by NIGMS/NIH funding to Dr. Christopher Berger (GM101066). We thank Dr. David Warshaw and Guy Kennedy for training and technical support during the development of this work. We would also like to thank Vermont Livestock & Slaughter (Ferrisburgh, VT) for their continued support of our work. Thanks to Micro Video Instruments especially Dr. Sean Christie and Dr. Roy Kinoshita for technical support for the TIRF microscope. Additional thanks to Dr. Jason Stumpff, Lynn Chrin and Dr. Gregory Hoeprich for their support at different stages in the development of this work. The authors declare no conflicts of interest with the work presented here. This manuscript was written by JS and CB. JS and CB participated in editing. Experiments were designed by JS and CB and performed by JS and AC. RA designed MATLAB code.

References

Al-Bassam, J., Ozer, R.S., Safer, D., Halpain, S., and Milligan, R.A. (2002). MAP2 and tau bind longitudinally along the outer ridges of microtubule protofilaments. J. Cell Biol. *157*, 1187-1196.

Andreadis, A. (2005). Tau gene alternative splicing: expression patterns, regulation and modulation of function in normal brain and neurodegenerative diseases. Biochim. Biophys. Acta *1739*, 91-103.
Ballatore, C., Lee, V.M., and Trojanowski, J.Q. (2007). Tau-mediated neurodegeneration in Alzheimer's disease and related disorders. Nat. Rev. Neurosci. *8*, 663-672.
Biernat, J., Gustke, N., Drewes, G., Mandelkow, E.M., and Mandelkow, E. (1993). Phosphorylation of Ser262 strongly reduces binding of tau to microtubules: distinction between PHF-like immunoreactivity and microtubule binding. Neuron *11*, 153-163.
Brouhard, G.J., Stear, J.H., Noetzel, T.L., Al-Bassam, J., Kinoshita, K., Harrison, S.C., Howard, J., and Hyman, A.A. (2008). XMAP215 Is a Processive Microtubule Polymerase. Cell *132*, 79-88.
Chen, J., Kanai, Y., Cowan, N.J., and Hirokawa, N. (1992). Projection domains of MAP2 and tau determine spacings between microtubules in dendrites and axons. Nature *360*, 674-677.
Choi, M.C., Chung, P.J., Song, C., Miller, H.P., Kiris, E., Li, Y., Wilson, L., Feinstein, S.C., and Safinya, C.R. (2017). Paclitaxel suppresses Tau-mediated microtubule bundling in a concentration-dependent manner. Biochim. Biophys. Acta *1861*, 3456-3463.
Cleveland, D.W., Hwo, S.-Y., and Kirschner, M.W. (1977). Physical and chemical properties of purified tau factor and the role of tau in microtubule assembly. J. Mol. Biol. *116*, 227-247.
Di Maïo, I.L., Barbier, P., Allegro, D., Brault, C., and Peyrot, V. (2014). Quantitative Analysis of Tau-Microtubule Interaction Using FRET. Int. J. Mol. Sci. *15*, 14697-14714.
Dixit, R., Ross, J.L., Goldman, Y.E., and Holzbaur, E.L. (2008). Differential regulation of dynein and kinesin motor proteins by tau. Science *319*, 1086-1089.
Elbaum-Garfinkle, S., and Rhoades, E. (2012). Identification of an aggregation-prone structure of tau. J. Am. Chem. Soc. *134*, 16607-16613.
Goode, B.L., Chau, M., Denis, P.E., and Feinstein, S.C. (2000). Structural and functional differences between 3-repeat and 4-repeat tau isoforms. Implications for normal tau function and the onset of neurodegenetative disease. J. Biol. Chem. *275*, 38182-38189.
Hinrichs, M.H., Jalal, A., Brenner, B., Mandelkow, E., Kumar, S., and Scholz, T. (2012). Tau protein diffuses along the microtubule lattice. J. Biol. Chem. *287*, 38559-38568.
Hirokawa, N., Shiomura, Y., and Okabe, S. (1988). Tau proteins: the molecular structure and mode of binding on microtubules. J. Cell Biol. *107*, 1449-1459.
Hoeprich, G.J., Thompson, A.R., McVicker, D.P., Hancock, W.O., and Berger, C.L. (2014). Kinesin's neck-linker determines its ability to navigate obstacles on the microtubule surface. Biophys. J. *106*, 1691-1700.
Hyman, A., Drechsel, D., Kellogg, D., Salser, S., Sawin, K., Steffen, P., Wordeman, L., and Mitchison, T. (1991). Preparation of modified tubulins. Methods Enzymol. *196*, 478-485.
Jeganathan, S., von Bergen, M., Brutlach, H., Steinhoff, H.J., and Mandelkow, E. (2006). Global hairpin folding of tau in solution. Biochemistry *45*, 2283-2293.
Johnson, I.D. (2010). The Molecular Probes Handbook: A Guide to Fluorescent Probes and Labeling Technologies, 11th Edition. Life Technologies Corporation.
Joo, C., and Ha, T. (2012a). Imaging and identifying impurities in single-molecule FRET studies. Cold Spring Harbor protocols *2012*, 1109-1112.

Joo, C., and Ha, T. (2012b). Preparing sample chambers for single-molecule FRET. Cold Spring Harbor protocols *2012*, 1104-1108.
Kadavath, H., Hofele, R.V., Biernat, J., Kumar, S., Tepper, K., Urlaub, H., Mandelkow, E., and Zweckstetter, M. (2015a). Tau stabilizes microtubules by binding at the interface between tubulin heterodimers. Proc. Natl. Acad. Sci. U. S. A. *112*, 7501-7506.
Kadavath, H., Jaremko, M., Jaremko, L., Biernat, J., Mandelkow, E., and Zweckstetter, M. (2015b). Folding of the Tau Protein on Microtubules. Angew. Chem. Int. Ed. Engl. *54*, 10347-10351.
Kanaan, N.M., Morfini, G., Pigino, G., LaPointe, N.E., Andreadis, A., Song, Y., Leitman, E., Binder, L.I., and Brady, S.T. (2012). Phosphorylation in the amino terminus of tau prevents inhibition of anterograde axonal transport. Neurobiol. Aging *33*, 826 e815-830.
Kapanidis, A.N., Laurence, T.A., Lee, N.K., Margeat, E., Kong, X., and Weiss, S. (2005). Alternating-laser excitation of single molecules. Acc. Chem. Res. *38*, 523-533.
Konzack, S., Thies, E., Marx, A., Mandelkow, E.M., and Mandelkow, E. (2007). Swimming against the tide: mobility of the microtubule-associated protein tau in neurons. J. Neurosci. *27*, 9916-9927.
LaPointe, N.E., Morfini, G., Pigino, G., Gaisina, I.N., Kozikowski, A.P., Binder, L.I., and Brady, S.T. (2009). The amino terminus of tau inhibits kinesin-dependent axonal transport: implications for filament toxicity. J. Neurosci. Res. *87*, 440-451.
Lee, G., Thangavel, R., Sharma, V.M., Litersky, J.M., Bhaskar, K., Fang, S.M., Do, L.H., Andreadis, A., Van Hoesen, G., and Ksiezak-Reding, H. (2004). Phosphorylation of tau by fyn: implications for Alzheimer's disease. J. Neurosci. *24*, 2304-2312.
Ling, H. (2018). Untangling the tauopathies: Current concepts of tau pathology and neurodegeneration. Parkinsonism Relat. Disord. *46 Suppl 1*, S34-s38.
Lowndes, M., and Nelson, W.J. (2013). Fabricating surfaces with distinct geometries and different combinations of cell adhesion proteins. Methods Mol. Biol. *1046*, 219-230.
Margeat, E., Kapanidis, A.N., Tinnefeld, P., Wang, Y., Mukhopadhyay, J., Ebright, R.H., and Weiss, S. (2006). Direct observation of abortive initiation and promoter escape within single immobilized transcription complexes. Biophys. J. *90*, 1419-1431.
Martin, L., Latypova, X., and Terro, F. (2011). Post-translational modifications of tau protein: Implications for Alzheimer's disease. Neurochem. Int. *58*, 458-471.
Martin, L., Latypova, X., Wilson, C.M., Magnaudeix, A., Perrin, M.-L., Yardin, C., and Terro, F. (2013). Tau protein kinases: Involvement in Alzheimer's disease. Ageing Research Reviews *12*, 289-309.
McVicker, D.P., Chrin, L.R., and Berger, C.L. (2011). The nucleotide-binding state of microtubules modulates kinesin processivity and the ability of Tau to inhibit kinesin-mediated transport. J. Biol. Chem. *286*, 42873-42880.
McVicker, D.P., Hoeprich, G.J., Thompson, A.R., and Berger, C.L. (2014). Tau interconverts between diffusive and stable populations on the microtubule surface in an isoform and lattice specific manner. Cytoskeleton (Hoboken, N.J.) *71*, 184-194.
Morfini, G., Szebenyi, G., Elluru, R., Ratner, N., and Brady, S.T. (2002). Glycogen synthase kinase 3 phosphorylates kinesin light chains and negatively regulates kinesin-based motility. EMBO J. *21*, 281-293.
Rosenberg, K.J., Ross, J.L., Feinstein, H.E., Feinstein, S.C., and Israelachvili, J. (2008). Complementary dimerization of microtubule-associated tau protein: Implications for

microtubule bundling and tau-mediated pathogenesis. Proc. Natl. Acad. Sci. U. S. A. *105*, 7445-7450.
Roy, R., Hohng, S., and Ha, T. (2008). A practical guide to single-molecule FRET. Nature methods *5*, 507-516.
Santarella, R.A., Skiniotis, G., Goldie, K.N., Tittmann, P., Gross, H., Mandelkow, E.M., Mandelkow, E., and Hoenger, A. (2004). Surface-decoration of microtubules by human tau. J. Mol. Biol. *339*, 539-553.
Schindelin, J., Arganda-Carreras, I., Frise, E., Kaynig, V., Longair, M., Pietzsch, T., Preibisch, S., Rueden, C., Saalfeld, S., Schmid, B., Tinevez, J.Y., White, D.J., Hartenstein, V., Eliceiri, K., Tomancak, P., and Cardona, A. (2012). Fiji: an open-source platform for biological-image analysis. Nature methods *9*, 676-682.
Shrestha, D., Jenei, A., Nagy, P., Vereb, G., and Szöllősi, J. (2015). Understanding FRET as a Research Tool for Cellular Studies. Int. J. Mol. Sci. *16*, 6718-6756.
Stern, J.L., Lessard, D.V., Hoeprich, G.J., Morfini, G.A., and Berger, C.L. (2017). Phospho-regulation of tau modulates inhibition of kinesin-1 motility. Mol. Biol. Cell.
Vershinin, M., Carter, B.C., Razafsky, D.S., King, S.J., and Gross, S.P. (2007). Multiple-motor based transport and its regulation by Tau. Proc. Natl. Acad. Sci. U. S. A. *104*, 87-92.

Figures

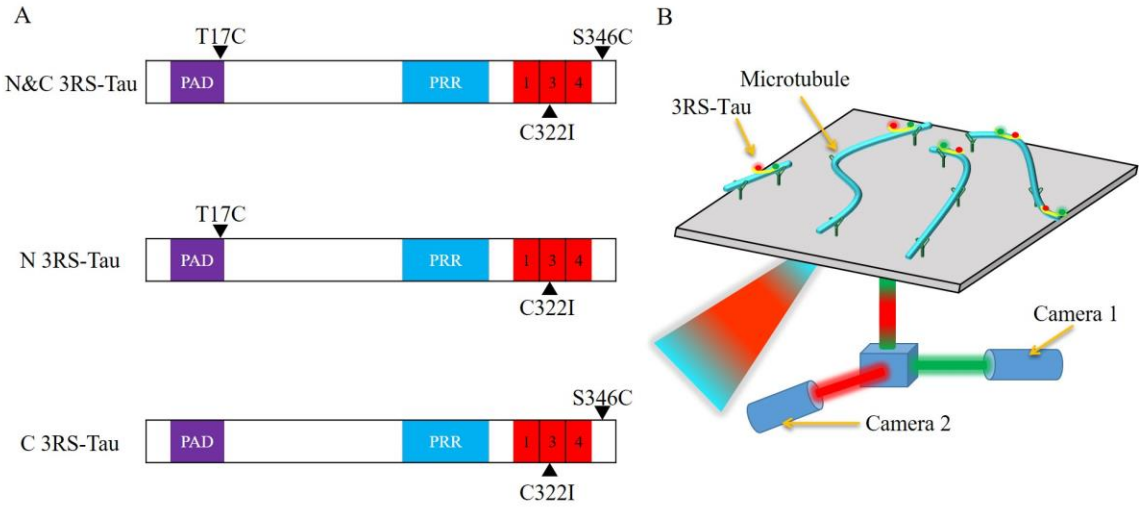

Figure 3.1: Tau constructs and imaging setup.

A) To create the 3RS-Tau constructs used in these experiments, site directed mutagenesis was used to change the naturally occurring cysteine to an isoleucine (C322I), which is the residue that occurs in other binding repeats at this position. Residues in the N- and C- termini (T17 and S346) were mutated to cysteines to create N&C 3RS-Tau. B) An inverted Eclipse Ti Microscope with two iXON Ultra EMCCD cameras was used to perform TIRF microscopy with ALEX. Labeled Tau was imaged by alternating exposure with 640 nm and 488 nm argon lasers. Alexa 405 labeled microtubules were imaged with a 405 nm laser.

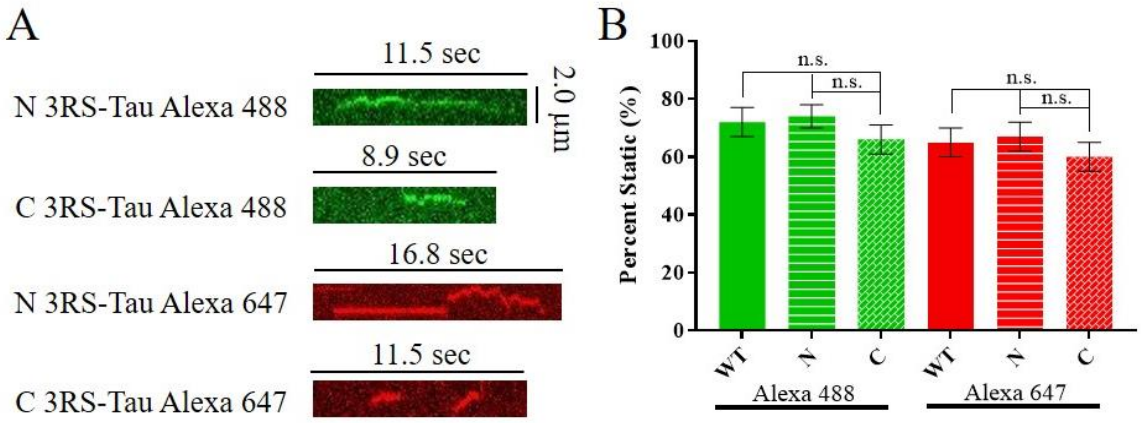

Figure 3.2: Comparison of Singly labeled N 3RS-Tau and C 3RS-Tau to WT 3RS-Tau.

To control for the effect of labeling 3RS-Tau at the N- or C-termini with either Alexa 488 or 647, single cysteine constructs (N 3RS-Tau and C 3RS-Tau) were labeled with either Alexa 488 or 647. TIRF microscopy was used to perform behavioral assays comparing Alexa 488 or 647 singly labeled WT, N and C 3RS-Tau. **A)** Kymographs of N 3RS-Tau and C 3RS-Tau labeled with either Alexa 488 or 647. All constructs demonstrated static (straight lines) and diffusive (jagged lines) binding. **B)** Histogram of percent static binding for WT, N and C 3RS-Tau labeled with Alexa 488 and 647. No significant difference was observed for either label or labeling position ($p > 0.05$). See Supplemental Table S2.1.

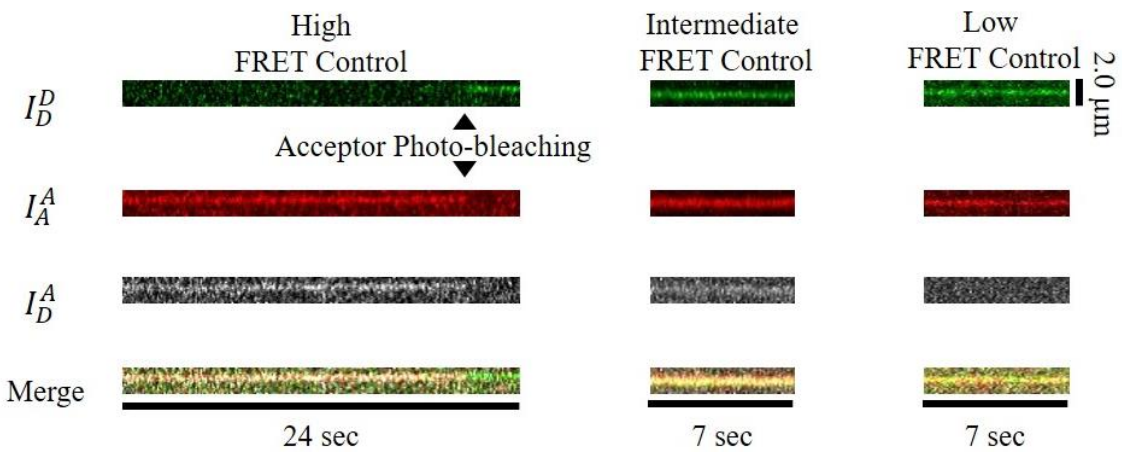

Figure 3.3: Kymographs for DNA oligomer smFRET controls of High, Intermediate and Low FRET.

The High FRET oligomer was designed by labeling the 5' and 3' end of a two turn oligomer with Alexa 488/647. The Intermediate FRET oligomer was designed by labeling both 5' ends of a one and a half turn oligomer with Alexa 488/647. To create the Low FRET oligomer, the same sequence used for the High FRET oligomer was dual labeled at the 5' ends with Alexa 488/647. Donor (I_D^D) and acceptor (I_A^A) labeled events were tracked and intensities were measured in donor, acceptor and energy transfer (I_D^A) channels. These intensities were background corrected and photo-bleaching events were used to calculate constants for donor bleed through into the acceptor channel (χ) and the difference in the system's sensitivity to detect donor vs. acceptor fluorophores (γ). These constants were then used to calculate both FRET efficiency and labeling stoichiometry.

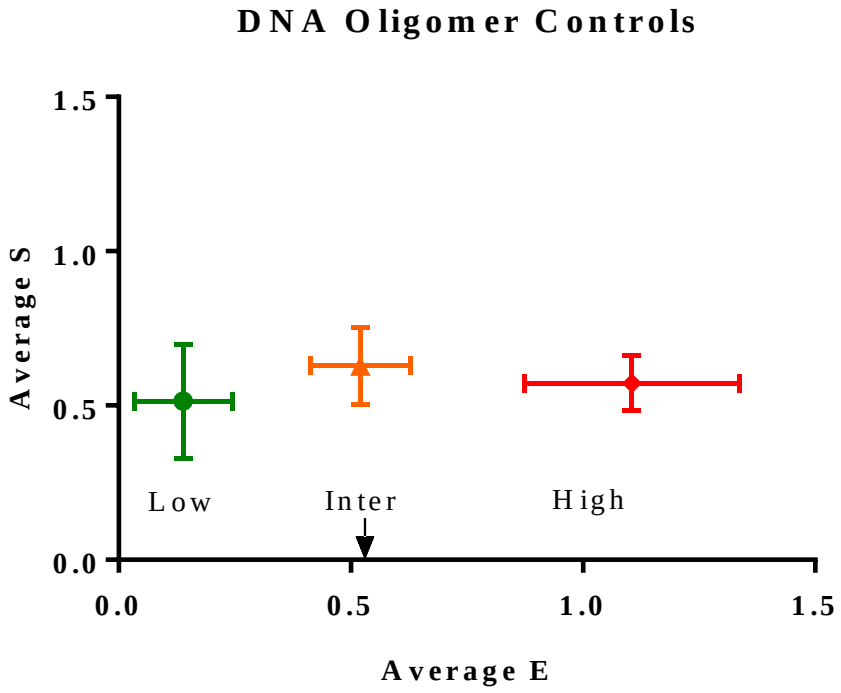

Figure 3.4: Stoichiometry (S) versus Average Efficiency (E) plots for DNA oligomer smFRET controls for High, Intermediate (Inter) and Low FRET states.

Dual labeled DNA oligomers of varying length and fluor position were used to test the imaging system's ability to detect changes in FRET efficiency based on the R_0 (arrow; 52.7Å) for Alexa488/647. We found that we were able to detect efficiency changes within the Low to High FRET range of 24 Å to 71 Å. Importantly, we were also able to distinguish intermediate FRET efficiencies from high FRET efficiencies (Intermediate: 0.52 ± 0.11). Furthermore, the average FRET efficiency for the Intermediate oligomer agrees with our calculated R_0 (52.7 Å).

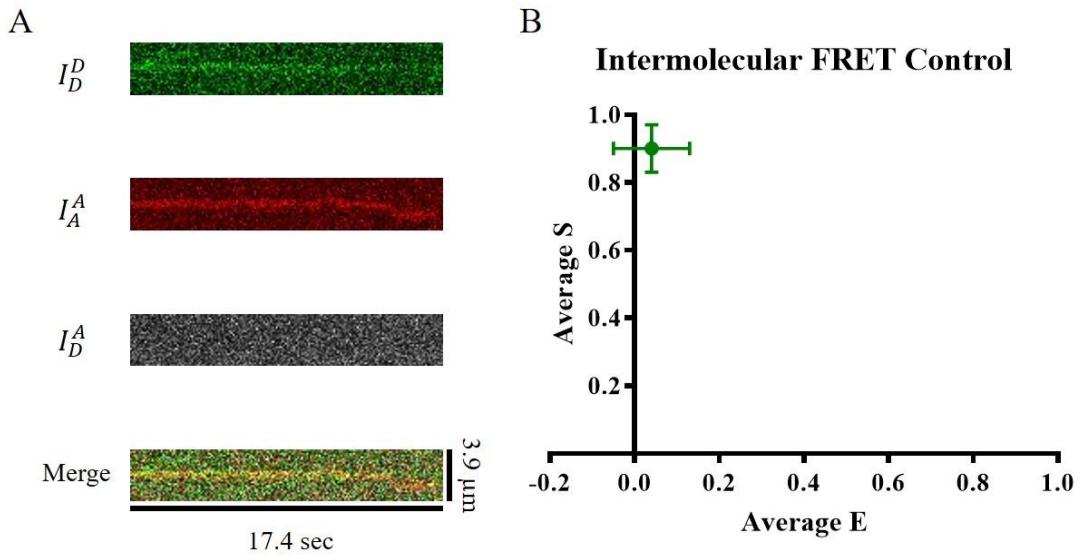

Figure 3.5: Intermolecular FRET was not observed under our smFRET imaging conditions.

A) To ensure that our smFRET events represent only dual labeled single molecule binding events and not intermolecular interactions between interacting molecules, we imaged singly labeled Alexa 488 and 647 WT, N and C 3RS-Tau both at 20X the concentration (1 nM). Kymographs above are representative of overlapping Alexa 488 (I_D^D) and 647 (I_A^A). No signal was observed in the energy transfer channel (I_D^A). B) Average ***S*** and ***E*** plot for Alexa 488 and 647 singly labeled static and diffusive events that overlap tracked in the donor channel (average ***S*** = 0.90 ± 0.10; average ***E*** = 0.04 ± 0.09; N = 9) and measured with MTrackJ in all channels. No significant difference was observed compared to the Low DNA oligomer (P > 0.05; T-test with Welch's correction).

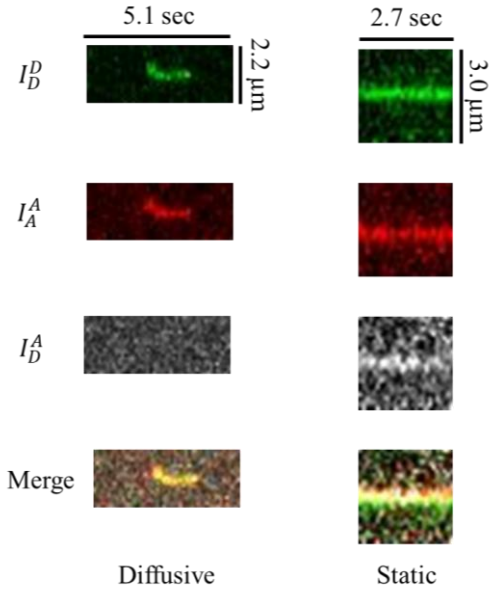

Figure 3.6: Kymographs of dual labeled N&C 3RS-Tau.

Static and diffusive events were tracked and measured in the donor, acceptor and energy transfer channels (I_D^D , I_A^A , I_D^A). Signal was observed in the I_D^A channel for static events on both paclitaxel and GMPCPP stabilized microtubules. No signal was observed in this channel for diffusive events on either lattice.

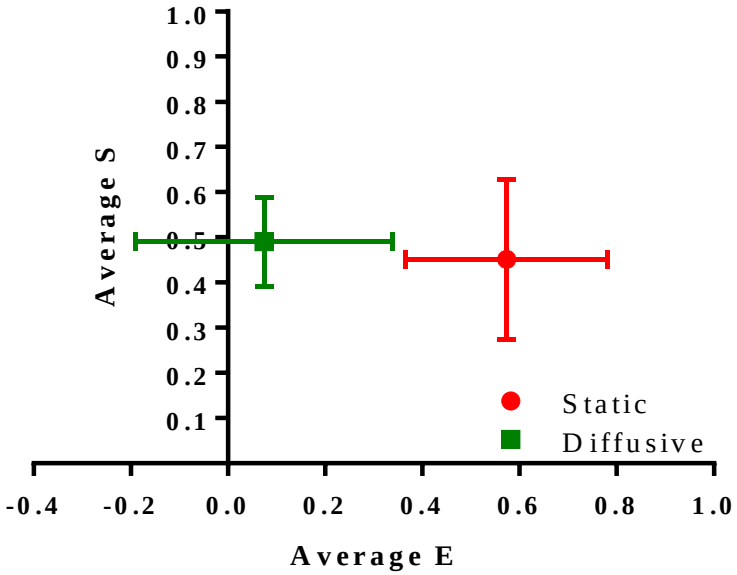

Figure 3.7: Average S and E plots for static and diffusive.

There was a significant difference ($P < 0.05$, T-test with Welch's correction) between static events ($E = 0.57 \pm 0.21$; $S = 0.45 \pm 0.12$; $N= 6$) and diffusive events ($E = 0.07 \pm 0.26$; $S = 0.49 \pm 0.10$; $N= 6$) on both lattice structures. The N- and C-termini of 3RS-Tau interacts more closely in the static state than the diffusive state. This indicates that Tau is more folded on the static state than the diffusive state on both paclitaxel and GMPCPP.

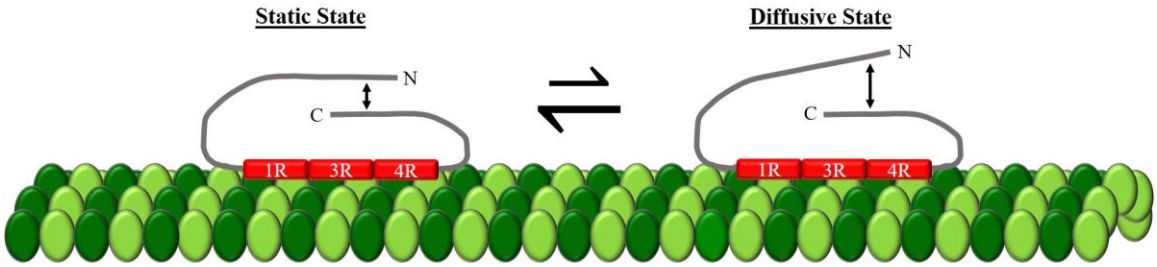

Figure 3.8: Model of N- and C-termini interactions while Tau (red and gray) is bound to the microtubule (green) in both the static and diffusive state.

Our results show that the N- and C-termini interact closely in the static state while the interaction is reduced in the diffusive state. Reduced interaction the diffusive state may allow for increased interaction between Tau's C-terminal residues and tubulin's C-terminal tail (CTT). This interaction has previously been shown to facilitate diffusive binding (Hinrichs *et al.* 2012). In the static state, increased N- and C-termini interaction may in turn reduce Tau-CTT interactions. These results represent the first *in vitro* single-molecule structural study of dynamic Tau binding on the microtubule surface.

Supplemental Table S3.1: Behavioral Data for Singly Labeled 3RS-Tau Control Constructs

	Tracks	Events	% Static (± SD)	Static Dwell Time (s)	Diffusive Dwell Time (s)	Diffusion Coefficient ($\mu m^2/s$)	Alpha (R^2)
Alexa 488							
WT	120	163	72 ± 5	1.16	0.52	0.18	1.05 ($R^2 = 0.97$)
N	106	160	74 ± 4	1.40	0.49	0.12	1.05 ($R^2 = 0.94$)
C	103	155	66 ± 5	1.02	0.49	0.16	0.70 ($R^2 = 0.98$)
Alexa 647							
WT	114	175	65 ± 5	1.44	0.49	0.11	1.10 ($R^2 = 0.98$)
N	161	327	67 ± 5	1.85	0.58	0.15	1.20 ($R^2 = 0.99$)
C	137	364	60 ± 5	1.86	0.51	0.14	0.84 ($R^2 = 0.90$)

Table showing behavioral data for WT, N and C 3RS-Tau labeled Alexa 488 or 647. All data was collected on Alexa 405 labeled paclitaxel stabilized microtubules. No significant difference was found in behavior for any construct with either label (Fisher's Exact Test; $p > 0.05$). Data was analyzed using a sliding window analysis to determine static or diffusive behavior. No differences were seen in static or diffusive dwell times and alpha values calculated for diffusive events from each construct and labeling condition did not differ greatly. Label type and position does not affect 3RS-Tau binding behavior.

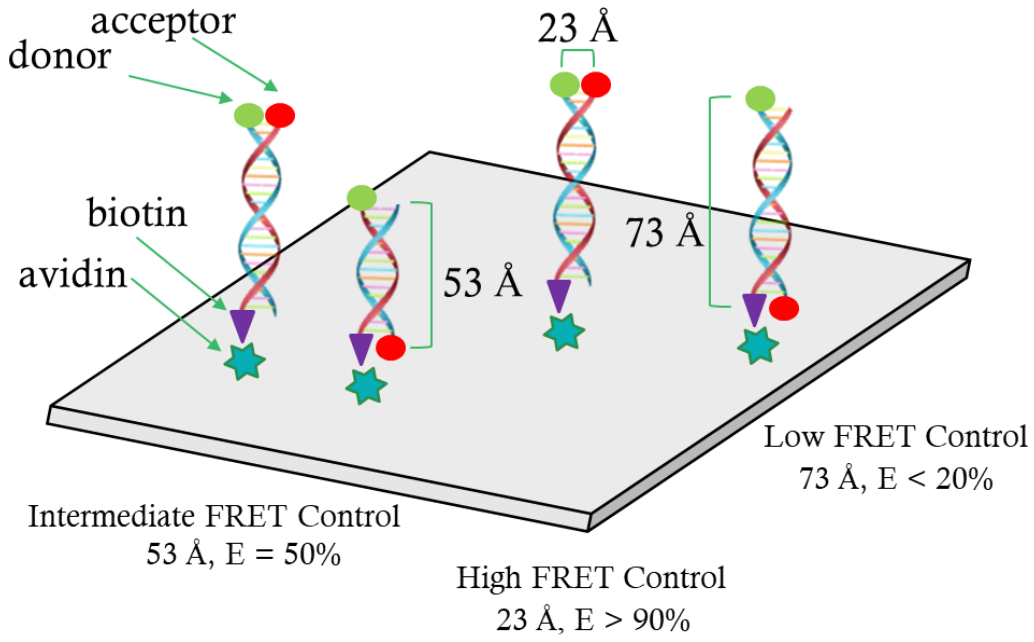

Figure S3.1: Biotinylated DNA oligomers dual labeled with Alexa 488/647.

Labels placed at fixed distances were used to control for high, intermediate and low FRET conditions based on the calculated R_0. Upon acceptor photo-bleaching, these oligomers were also used to calculate the constants χ (donor bleed through in the acceptor channel) and γ (sensitivity differences when detecting donor vs. acceptor fluorophores) needed to calculate ***E*** and ***S***:

$$\chi = {I_D^A}/{I_D^D} \quad \text{and} \quad \gamma = {\Delta I_A^A}/{\Delta I_D^D}$$

CHAPTER 4: CONCLUSIONS AND FUTURE DIRECTIONS

Tau performs many functions within axonal transport, which must be carefully regulated to ensure neuronal health. This work explores the link between regulation of Tau behavior and function while examining the structural changes that underlie this regulation. In chapter two we demonstrate that phosphorylation regulates Tau function on the microtubule surface, while in chapter three we provide the first evidence for structural change underlying static versus diffusive binding.

Work with tyrosine 18 (Y18) up to this point has focused on its participation in signaling cascades (LaPointe *et al.*, 2009; Kanaan *et al.*, 2012) and its potential role in stabilizing a dynamic folded conformation of Tau in solution (Jeganathan *et al.*, 2006). However, Y18 involvement in the regulation of Tau behavior and function on the microtubule surface has not been previously demonstrated. It has just recently been shown that Tau is able to bind the microtubule in a static-diffusive state equilibrium (Hinrichs *et al.*, 2012; McVicker *et al.*, 2014) and the purpose of this equilibrium has just begun to be understood (McVicker *et al.*, 2011; Stern *et al.*, 2017). While we work to understand Tau's dynamic bound equilibrium, other questions remain to be answered.

Within the field, the study of Tau post-translational modifications (PTMs) mostly relates to Tau phosphorylation and the studied phosphorylation is usually disease state associated (Martin *et al.*, 2013b). While our work with Y18 phosphorylation in chapter two represents the first evidence that non-disease state regulation of Tau modification can affect its behavior and function, it also serves to highlight a significant gap in our knowledge. As a field we have not focused on non-disease state Tau regulation by phosphorylation or other PTMs. Additionally, though we have demonstrated that Tau can

bind both statically and diffusively *ex vivo*, no work has not been done to address the cellular relevance of this behavior to motor motility modulation.

Experiments building on the work presented in chapter two should explore the relevance of Tau's static-diffusive state equilibrium on the movement of kinesin-1 within the cell. While we have shown that the Y18 phosphorylation mediated shift towards diffusive binding is maintained *ex vivo*, we have not examined *ex vivo* or *in vivo* motor motility in the presence of Tau. *In vivo* work could be done by co-expressing GFP labeled kinesin-1 with either WT or Y18E 3RS-Tau in a neuronal cell line such as CAD, which does not express Tau (Bisig *et al.*, 2009). Given the increase in ionic strength and crowding, it is important to establish that the *in vitro* effect we observed is maintained within the cell.

In addition to cargo binding and motor motility, Y18 has been implicated in the stabilization of a solution based dynamic folded conformation of Tau (Jeganathan *et al.*, 2006). The possible involvement of Y18 in the regulation of Tau structure led us to the question the role of structural change in Tau behavior and function on the microtubule surface. Phosphorylation of Tau microtubule binding regions has been shown to reduce its affinity for the microtubule surface. However, in chapter two we show that Y18 phospho-mimetics also exhibit reduced affinity for the microtubule surface. Y18 is found in Tau's projection domain, which does not bind the microtubule (Goode *et al.*, 2000). This raises the question of how Y18 phosphorylation in the N-terminal region affects the affinity of the protein for the microtubule. One possible explanation for this Y18 mediated drop in affinity is that Y18 phosphorylation affects long range structural changes while Tau is bound to the microtubule.

Though Tau structure has been studied both on and off the microtubule, no work has been done to understand how Tau's structure may change with static and diffusive binding. Cyro-EM creates snap shots of static binding and cannot be used to study Tau's dynamic binding behavior and the structural changes that may occur. Solution based bulk and single molecule FRET studies have been used to study Tau microtubule interactions, but like cryo-EM are not currently used to study dynamic behavioral changes on the microtubule surface. To address this gap in knowledge, we have used smFRET techniques detailed in chapter three to observe differences in Tau N- and C-termini interactions.

Our work on Tau's microtubule bound structure encompasses the development of the reagents, imaging and analysis methods needed to test the hypothesis that Tau binds the microtubule in distinct conformations which underlie static and diffusive binding. We have demonstrated the efficacy of our system using N&C 3RS-Tau to show that there is a difference in the average N- and C-termini interactions between the static and diffusive state. However, we have not completed testing other labeling positions within the protein (Figure 4.1). Preliminary work with N&3 3RS-Tau suggests that there is little to no interaction between the N-terminal and the 3rd microtubule binding repeat in both the static and diffusive state (Alisa Cario, personal communication). We have yet to test the interactions between the C-terminal and the 3rd microtubule binding repeat. The results from these three labeling positions (N&C 3RS-Tau, N&3 3RS-Tau and 3&C 3RS-Tau) based on previously published solution based FRET assays (Jeganathan *et al.*, 2006) should give us an overall structure for Tau bound in both the static and diffusive state (Figure 4.1). To validate our work or in the case that the chosen labeling sites are not

sufficient, other positions previously used for dual labeling such as sites in the 1st and 2nd microtubule binding repeats, acidic inserts and proline rich region can be used (Jeganathan *et al.*, 2006; Elbaum-Garfinkle and Rhoades, 2012).

In chapter three we report the average stoichiometry and efficiency of energy transfer for static and diffusive behavior based on averages for individual events. Therefore, we report average differences when Tau is bound in the static versus diffusive state. Since the focus of this work is on average conformational change during static and diffusive binding, it is highly likely that additional structural transitions occur that we have not observed. Further analysis of our data would allow us to determine how dynamic the interactions in the static and diffusive state are. Probability distribution analysis can be used to predict the shape of smFRET histograms for molecules interconverting between states (Santoso *et al.*, 2010). Fitting the expected probability distributions for different states to histograms of our frame-to-frame ***E*** data would allow us to determine if Tau has dynamic transitions in the static and diffusive state. Similarly, Hidden Markov Modeling can be used to detect transition states that have been obscured by the noise in a system (McKinney *et al.*, 2006). Using this approach a transition probability matrix and emission probability functions could be used to fit our experimental data and determine the points at which transitions were likely (McKinney *et al.*, 2006). Fluorescence cross-correlation spectroscopy (FCS) in combination with TIRF-based single-molecule FRET could be used to obtain information about the time-scale of dynamics for specific structural transitions in Tau in the presence of microtubules.

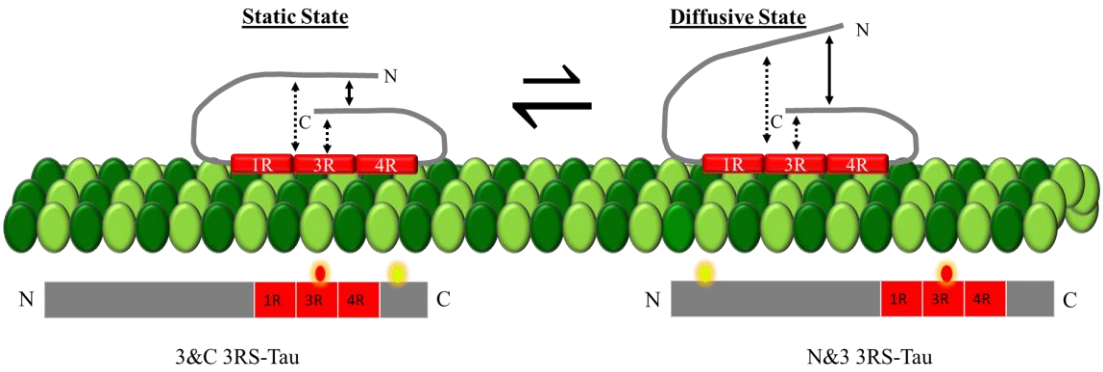

Figure 4.1: Tau's Overall Bound Structure

Work in chapter three shows that Tau's N- and C-termini on average, interact more closely in the static than the diffusive state (solid double-headed arrow). However, work must be done to understand the interactions between the N-terminal and the microtubule binding repeats (dashed double-headed arrow), and the C-terminal and the microtubule binding repeats (dashed double headed arrow). Dual labeled N&3 and 3&C 3RS-Tau constructs have been made and work has begun with N&3 3RS-Tau. Other labeling sites can be chosen in the 1st and 2nd microtubule binding repeats, acidic inserts and proline rich region to further define and validate Tau's microtubule bound structure.

Ultimately our work with single molecule fluorescence resonance energy transfer (smFRET) will allow us to correlate behavioral changes with FRET efficiency changes on the microtubule surface. As we have demonstrated, we have the means to perform frame-to-frame background correction and calculate average FRET efficiency and average stoichiometry of labeling. However, the methods used to determine static versus diffusive binding identify whole events as static or diffusive and do not allow us to identify state transitions that may occur during an event. The next step is implementing MATLAB code for a sliding window analysis to identify these transitions and calculate mean squared displacement and α values for diffusive events. We are currently working to complete this next phase of analysis which will allow us to better define the static and diffusive states and better correlate FRET efficiency changes with changes in behavior.

Over the years, cryo-EM studies of microtubule bound Tau have attempted to solve Tau structure on the microtubule surface. Together, these studies show that Tau binds the microtubule along protofilaments potentially close to α-tubulin (Hirokawa *et al.*, 1988; Al-Bassam *et al.*, 2002; Santarella *et al.*, 2004). The most recent cryo-EM study has been able to resolve microtubule binding repeats to a much higher resolution than any other (Kellogg *et al.*, 2018). This study shows that Tau microtubule binding repeats bind in tandem along tubulin dimers (Figure 4.2) (Kellogg *et al.*, 2018). Each binding repeat was found to be fully extended across three tubulin monomers (Figure 4.2) (Kellogg *et al.*, 2018). These results indicate that while on the microtubule surface, the microtubule binding repeats are extended but, as with the other cryo-EM studies, the regions of Tau that extended away from the microtubule were not resolved.

In conjunction with our work in chapter three, these results lead to the hypothesis that Tau's N- and C-termini interactions in the static state facilitate microtubule binding repeat extension while bound to the microtubule surface. Unfortunately, the recent cryo-EM work (Kellogg *et al.*, 2018) did not resolve portions of Tau that extend away from the microtubule surface and cannot be used to observe dynamic structural change. However, this work highlights new fluor placement positions for use in our smFRET assay. Our current dual labeling sites do not take into account changes in the interactions of the microtubule binding repeats. While a distance of 80 Å between repeats (Figure 4.2) is outside the $\boldsymbol{R_0}$ measured for Alexa 488/647, placement of probes at the end of one repeat and the center of another repeat should allow us to observe any changes that may occur to the extension of the repeats in the static and diffusive state. If we could replicate the results of the cryo-EM work where the microtubule binding repeats are fully extended and therefore should be in a low FRET state, we would not only validate our system but demonstrate that it can be used to compliment cryo-EM data. Using both approaches would allow us to make significant progress in our understanding of Tau's dynamic structure on the microtubule structure.

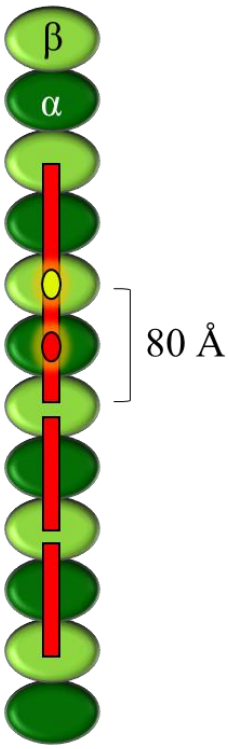

Figure 4.2: smFRET experiment to determine how microtubule binding repeats interact in the static and diffusive state.

New cryo-EM work shows that Tau microtubule binding repeats (red rectangles) interact with the microtubule (green) in tandem. While the dual labeled constructs we plan to use for ongoing smFRET assays do not cover interactions between microtubule binding repeats, this study highlights the need to include dual label sites within the binding repeats. Each repeat stretches 80 Å (Kellogg *et al.*, 2018), a distance which is outside the range of the Alexa488/647 FRET pair. However, placement of fluorophores (yellow/red oval) at the end of one repeat and the middle of another (~40-50 Å distance) would allow for observation of structural changes with static or diffusive binding and allow us to validate our smFRET assay.

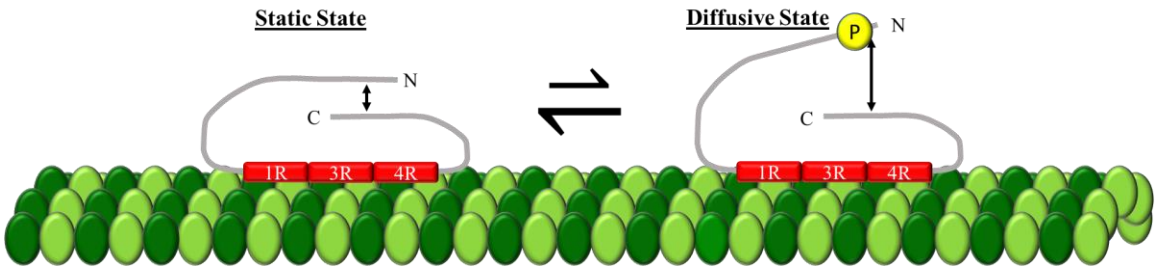

Figure 4.3: Effect of phosphorylation on Tau's microtubule bound structure.

In chapter two we demonstrate that phosphorylation at Y18 affects Tau behavior and function on the microtubule surface. Our work in chapter three shows that Tau's N- and C-termini interact more closely in the static than the diffusive state. Given that phospho-mimetics of Y18 shift Tau's binding equilibrium towards the diffusive state, we hypothesize that Y18 phosphorylation may disrupt N-C termini interactions thereby shifting the structural equilibrium to a more open conformation and the behavioral equilibrium towards diffusive binding. Currently, no work has been done to determine how phosphorylation affects Tau structure on the microtubule surface. Therefore to test this hypothesis we have generated Y18E 3RS-Tau smFRET constructs for all three positions (N&C, N&3, 3&C) for use in smFRET assays.

In chapter two, we demonstrate that phosphorylation regulates behavioral and functional change. However, it is not known how non-disease state phosphorylation events affect Tau's bound structure. In light of our work in chapter's two and three, we can hypothesize that Y18 phosphorylation disrupts N-C termini interactions thereby shifting the structural equilibrium to a more open conformation and the behavioral equilibrium towards diffusive binding. To test this hypothesis, we have generated Y18E 3RS-Tau smFRET constructs for all three positions (N&C, N&3, 3&C) for use in smFRET assays (Figure 4.3).

In addition to understanding how post-translational modifications affect Tau structure, we are also able to ask questions about other aspects of the Tau-microtubule interaction including patch formation, interactions with the microtubule in the static and diffusive state, and the physiological relevance of Tau structure. It has been shown that Tau binds the microtubule cooperatively and forms patches in the static state at high concentrations (Dixit *et al.*, 2008; McVicker *et al.*, 2014). However, the structural changes that underlie these patches and the Tau-Tau interactions that may occur are not well understood. It is hypothesized that N-termini intermolecular interactions, possibly through the acidic inserts, allow patch formation since 4RL-Tau (two acidic inserts) appears to form larger patches than 3RS-Tau (no acidic inserts) (Dixit *et al.*, 2008). To determine the structure of Tau within these patches, smFRET total internal reflection fluorescence (TIRF) microscopy experiments with alternating laser excitation (ALEX) could be performed on unlabeled microtubules with high concentrations of Alexa 405 labeled WT Tau (20-50 nM) spiked with a much lower concentration (500 pM) of Alexa

488/647 dual labeled Tau. This would allow for patch identification (Alexa 405) and imaging of Tau structure (Alexa488/647) within these patches.

The future integration of TIRF with fluorescence correlative spectroscopy (FCS) would allow us to identify potential Tau-Tau interactions within patches. Single donor and acceptor N-terminal labeled populations of WT Tau could be spiked into the same experimental setup described above. This technique would allow the resolution of Tau molecules within a patch and with the smFRET data would help us understand patch formation and composition and how that relates to observed Tau interactions within patches.

As explained in chapter three, tubulin C-terminal tails (CTT) have been shown to regulate Tau diffusive binding. In their absence, Tau has been shown to bind statically to the microtubule surface (Figure 4.4) (Hinrichs *et al.*, 2012). To further demonstrate the differences that underlie static versus diffusive binding and elucidate the involvement of the CTT in this process, smFRET assays can be performed on microtubules with and without CTT (Figure 4.4) (-/+ subtilisin treatment (Hinrichs *et al.*, 2012)). In addition to Tau structural changes with and without CTT, experiments can be performed to better understand the interactions that occur between Tau and the CTT. To carry out this experiment, the CTT would be acceptor labeled while Tau would be singly labeled with a donor probe (perhaps starting with the C-terminal since its truncation has been shown to reduce diffusive binding). Tubulin CTT could be tagged for labeling using a number of methods the most attractive being tubulin tyrosine ligase attachment of an unnatural amino acid (3-formyltyrosine) to the α-tubulin CTT and subsequent labeling with Alexa 647 hydrazide (Banerjee *et al.*, 2010). This would allow labeling of our existing bovine

brain tubulin stock with fluorophore without the need to express tubulin fused with a bulky protein tag or fluorescent marker. smFRET experiments could be performed using TIRF and ALEX. Though the preparation for these experiments would be challenging, they would allow us to better understand the interactions that dictate diffusive behavior.

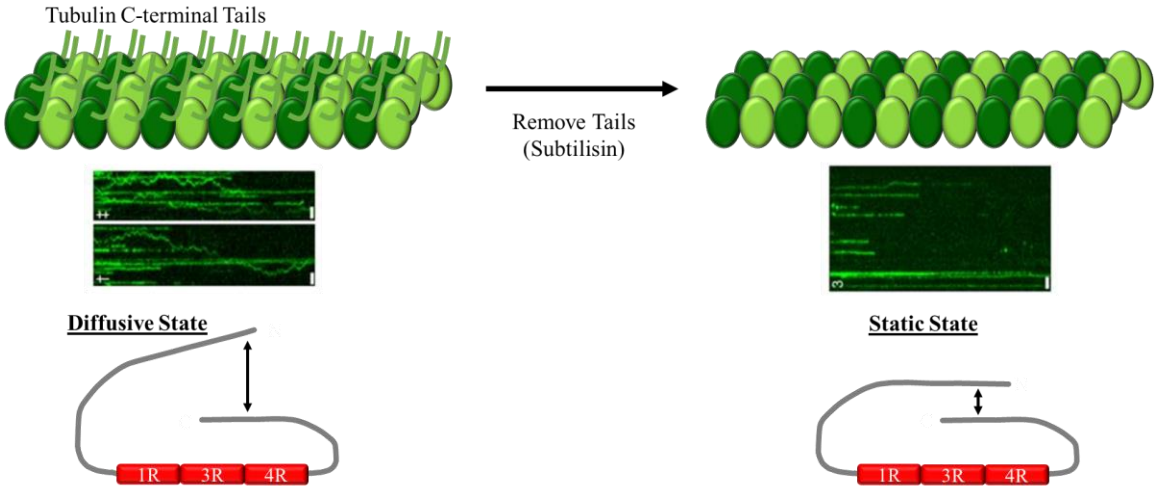

Figure 4.4: Tubulin C-terminal tails (CTT) allow Tau to bind diffusively.

Tubulin CTT have been shown to facilitate Tau diffusive binding on the microtubule surface. Treatment to remove CTTs leads to the loss of diffusive behavior as seen in the kymographs (Hinrichs *et al.*, 2012). Our results for N&C 3RS-Tau show that the N- and C-termini are farther apart in the diffusive state than the static state. This change in interaction may be due to Tau C-terminal interactions with tubulin CTT. The Tau C-terminal has been shown to interact with the CTT and truncation of the Tau C-terminal leads to loss of diffusive binding (Hinrichs *et al.*, 2012). smFRET assays of dual labeled Tau with and without the CTT would allow us to observe how the presence of the CTT affects Tau structure. Additionally, smFRET could also be performed between the Tau C-terminal and the CTT to increase our understanding of the interactions that take place between Tau and tubulin. Figure (kymographs) adapted from Hinrichs *et al.*, (2012) in accordance with the Creative Commons Attribution license.

Our ultimate goal is to adapt this smFRET assay for the identification of small molecules or other agents that may be efficacious in stabilizing non-disease state conformations under disease state conditions. One of the first steps to determining the feasibility of this idea is to establish that the structural changes we observed *in vitro* occur under physiological conditions. Increasing salt concentration and adding crowding agents to our existing smFRET assays would allow us to mimic some but not all of the conditions present in the cell. Carrying out smFRET experiments in squid axoplasm could be a means to recreate physiological conditions before moving to more challenging systems such as mammalian neuronal cell types. Squid axoplasm could be prepared as detailed in chapter two. Alexa 405 labeled Tau would be used to coat the axoplasmic microtubules and low concentrations of dual labeled Tau would be spiked in to observe structural changes of Tau on axoplasmic microtubules.

After confirming that the changes we observe *in vitro* occur under physiological conditions, we can test our smFRET assay's ability to detect structural changes in the presence of single molecules. Heparin is known to induce a disease state conformation of Tau and has been used to study Tau conformational change in solution (Elbaum-Garfinkle and Rhoades, 2012). We could image dual labeled Tau interacting with Alexa 405 microtubules in the presence and absence of heparin. This experiment would demonstrate our ability to observe structural changes caused an already studied small molecule and open the way for us to test other small molecules which may affect Tau structure. Comparing Tau structure with and without heparin would also allow us to determine which dual labeling position would be best for use in a high throughput screen. Ideally, interactions at these positions should only change in the presence of heparin.

Using these positions, we could simplify and automate our assay to test small molecule libraries for promising targets that restore wildtype interactions to populations of disease state Tau. Ultimately, these targets could have use in the treatment of Alzheimers disease and other Tauopathies.

Though the future experiments discussed above are challenging in their execution, they represent ways in which we can build on the work presented here to further our understanding of the role of Tau in axonal transport and the means by which it regulates motor motility and cargo delivery. The smFRET assay especially, lays the groundwork for an entirely new direction of thought and will allow us to answer questions, which were previously beyond reach.

COMPLETE BIBLIOGRAPHY

Ackmann, M., Wiech, H., and Mandelkow, E. (2000). Nonsaturable binding indicates clustering of tau on the microtubule surface in a paired helical filament-like conformation. J. Biol. Chem. *275*, 30335-30343.

Adler, C.E., Fetter, R.D., and Bargmann, C.I. (2006). UNC-6/Netrin induces neuronal asymmetry and defines the site of axon formation. Nat. Neurosci. *9*, 511-518.

Aiken, J., Buscaglia, G., Bates, E.A., and Moore, J.K. (2017). The α-Tubulin gene TUBA1A in Brain Development: A Key Ingredient in the Neuronal Isotype Blend. Journal of developmental biology *5*, 8.

Al-Bassam, J., Ozer, R.S., Safer, D., Halpain, S., and Milligan, R.A. (2002). MAP2 and tau bind longitudinally along the outer ridges of microtubule protofilaments. J. Cell Biol. *157*, 1187-1196.

Allen, R.D., Weiss, D.G., Hayden, J.H., Brown, D.T., Fujiwake, H., and Simpson, M. (1985). Gliding movement of and bidirectional transport along single native microtubules from squid axoplasm: evidence for an active role of microtubules in cytoplasmic transport. J. Cell Biol. *100*, 1736-1752.

Alushin, G.M., Lander, G.C., Kellogg, E.H., Zhang, R., Baker, D., and Nogales, E. (2014). High-resolution microtubule structures reveal the structural transitions in alphabeta-tubulin upon GTP hydrolysis. Cell *157*, 1117-1129.

Andreadis, A. (2005). Tau gene alternative splicing: expression patterns, regulation and modulation of function in normal brain and neurodegenerative diseases. Biochim. Biophys. Acta *1739*, 91-103.

Avila, J. (2010). Intracellular and Extracellular Tau. Front. Neurosci. *4*, 49.

Balabanian, L., Berger, C.L., and Hendricks, A.G. (2017). Acetylated Microtubules Are Preferentially Bundled Leading to Enhanced Kinesin-1 Motility. Biophys. J. *113*, 1551-1560.

Ballatore, C., Lee, V.M., and Trojanowski, J.Q. (2007). Tau-mediated neurodegeneration in Alzheimer's disease and related disorders. Nat. Rev. Neurosci. *8*, 663-672.

Banerjee, A., Panosian, T.D., Mukherjee, K., Ravindra, R., Gal, S., Sackett, D.L., and Bane, S. (2010). Site-Specific Orthogonal Labeling of the Carboxy Terminus of α-Tubulin. ACS Chem. Biol. *5*, 777-785.

Barlan, K., Lu, W., and Gelfand, V.I. (2013). The microtubule-binding protein ensconsin is an essential cofactor of kinesin-1. Curr. Biol. *23*, 317-322.

Barnes, A.P., and Polleux, F. (2009). Establishment of axon-dendrite polarity in developing neurons. Annu. Rev. Neurosci. *32*, 347-381.

Biernat, J., Gustke, N., Drewes, G., Mandelkow, E.M., and Mandelkow, E. (1993). Phosphorylation of Ser262 strongly reduces binding of tau to microtubules: distinction between PHF-like immunoreactivity and microtubule binding. Neuron *11*, 153-163.

Bisig, C.G., Chesta, M.E., Zampar, G.G., Purro, S.A., Santander, V.S., and Arce, C.A. (2009). Lack of stabilized microtubules as a result of the absence of major maps in CAD cells does not preclude neurite formation. The FEBS journal *276*, 7110-7123.

Black, M.M., Slaughter, T., and Fischer, I. (1994). Microtubule-associated protein 1b (MAP1b) is concentrated in the distal region of growing axons. J. Neurosci. *14*, 857-870.

Brady, S.T., Lasek, R.J., and Allen, R.D. (1982). Fast axonal transport in extruded axoplasm from squid giant axon. Science *218*, 1129-1131.

Brady, S.T., and Morfini, G.A. (2017). Regulation of motor proteins, axonal transport deficits and adult-onset neurodegenerative diseases. Neurobiol. Dis. *105*, 273-282.

Brady, S.T., Richards, B.W., and Leopold, P.L. (1993). Assay of vesicle motility in squid axoplasm. Methods Cell Biol. *39*, 191-202.

Britannica, E.o.E. (2018). Sciatic Nerve. In: Encyclopaedia Britannica, vol. 2018, ed. E.o.E. Britannica: Encyclopaedia Britannica, inc.

Bulinski, J.C., and Bossler, A. (1994). Purification and characterization of ensconsin, a novel microtubule stabilizing protein. J. Cell Sci. *107 (Pt 10)*, 2839-2849.

Bull, N.D., Guidi, A., Goedert, M., Martin, K.R., and Spillantini, M.G. (2012). Reduced Axonal Transport and Increased Excitotoxic Retinal Ganglion Cell Degeneration in Mice Transgenic for Human Mutant P301S Tau. PLoS One *7*, e34724.

Butner, K.A., and Kirschner, M.W. (1991). Tau protein binds to microtubules through a flexible array of distributed weak sites. J. Cell Biol. *115*, 717-730.

Carlomagno, Y., Chung, D.C., Yue, M., Castanedes-Casey, M., Madden, B.J., Dunmore, J., Tong, J., DeTure, M., Dickson, D.W., Petrucelli, L., and Cook, C. (2017). An acetylation-phosphorylation switch that regulates tau aggregation propensity and function. J. Biol. Chem. *292*, 15277-15286.

Chen, G., Sima, J., Jin, M., Wang, K.Y., Xue, X.J., Zheng, W., Ding, Y.Q., and Yuan, X.B. (2008). Semaphorin-3A guides radial migration of cortical neurons during development. Nat. Neurosci. *11*, 36-44.

Chen, J., Kanai, Y., Cowan, N.J., and Hirokawa, N. (1992). Projection domains of MAP2 and tau determine spacings between microtubules in dendrites and axons. Nature *360*, 674-677.

Choi, M.C., Chung, P.J., Song, C., Miller, H.P., Kiris, E., Li, Y., Wilson, L., Feinstein, S.C., and Safinya, C.R. (2017). Paclitaxel suppresses Tau-mediated microtubule bundling in a concentration-dependent manner. Biochim. Biophys. Acta *1861*, 3456-3463.

Chow, H.M., Guo, D., Zhou, J.C., Zhang, G.Y., Li, H.F., and Herrup, K. (2014). CDK5 activator protein p25 preferentially binds and activates GSK3beta *111*, E4887-4895.

Chua, J.J.E., Butkevich, E., Worseck, J.M., Kittelmann, M., Grønborg, M., Behrmann, E., Stelzl, U., Pavlos, N.J., Lalowski, M.M., Eimer, S., Wanker, E.E., Klopfenstein, D.R., and Jahn, R. (2012). Phosphorylation-regulated axonal dependent transport of syntaxin 1 is mediated by a Kinesin-1 adapter. Proceedings of the National Academy of Sciences *109*, 5862.

Cleveland, D.W., Hwo, S.-Y., and Kirschner, M.W. (1977). Physical and chemical properties of purified tau factor and the role of tau in microtubule assembly. J. Mol. Biol. *116*, 227-247.

Cohen, T.J., Guo, J.L., Hurtado, D.E., Kwong, L.K., Mills, I.P., Trojanowski, J.Q., and Lee, V.M. (2011). The acetylation of tau inhibits its function and promotes pathological tau aggregation. Nature communications *2*, 252.

Collins, S.P., Reoma, J.L., Gamm, D.M., and Uhler, M.D. (2000). LKB1, a novel serine/threonine protein kinase and potential tumour suppressor, is phosphorylated by cAMP-dependent protein kinase (PKA) and prenylated in vivo. Biochem. J. *345 Pt 3*, 673-680.

DeBerg, H.A., Blehm, B.H., Sheung, J., Thompson, A.R., Bookwalter, C.S., Torabi, S.F., Schroer, T.A., Berger, C.L., Lu, Y., Trybus, K.M., and Selvin, P.R. (2013). Motor Domain Phosphorylation Modulates Kinesin-1 Transport. The Journal of Biological Chemistry *288*, 32612-32621.

Dehmelt, L., and Halpain, S. (2005). The MAP2/Tau family of microtubule-associated proteins. Genome Biol. *6*, 204-204.

Desai, A., and Mitchison, T.J. (1997). Microtubule polymerization dynamics. Annu. Rev. Cell Dev. Biol. *13*, 83-117.

Di Maïo, I.L., Barbier, P., Allegro, D., Brault, C., and Peyrot, V. (2014). Quantitative Analysis of Tau-Microtubule Interaction Using FRET. Int. J. Mol. Sci. *15*, 14697-14714.

Dixit, R., Ross, J.L., Goldman, Y.E., and Holzbaur, E.L. (2008). Differential regulation of dynein and kinesin motor proteins by tau. Science *319*, 1086-1089.

Dorfman, J., and Macara, I.G. (2008). STRADalpha regulates LKB1 localization by blocking access to importin-alpha, and by association with Crm1 and exportin-7. Mol. Biol. Cell *19*, 1614-1626.

Dunn, S., Morrison, E.E., Liverpool, T.B., Molina-Paris, C., Cross, R.A., Alonso, M.C., and Peckham, M. (2008). Differential trafficking of Kif5c on tyrosinated and detyrosinated microtubules in live cells. J. Cell Sci. *121*, 1085-1095.

Ebneth, A., Godemann, R., Stamer, K., Illenberger, S., Trinczek, B., and Mandelkow, E. (1998). Overexpression of tau protein inhibits kinesin-dependent trafficking of vesicles, mitochondria, and endoplasmic reticulum: implications for Alzheimer's disease. J. Cell Biol. *143*, 777-794.

Elbaum-Garfinkle, S., and Rhoades, E. (2012). Identification of an aggregation-prone structure of tau. J. Am. Chem. Soc. *134*, 16607-16613.

Feinstein, H.E., Benbow, S.J., LaPointe, N.E., Patel, N., Ramachandran, S., Do, T.D., Gaylord, M.R., Huskey, N.E., Dressler, N., Korff, M., Quon, B., Cantrell, K.L., Bowers, M.T., Lal, R., and Feinstein, S.C. (2016). Oligomerization of the Microtubule Associated Protein Tau is Mediated by its N-Terminal Sequences: Implications for Normal and Pathological Tau Action. J. Neurochem.

Ferrer, I., Barrachina, M., and Puig, B. (2002). Glycogen synthase kinase-3 is associated with neuronal and glial hyperphosphorylated tau deposits in Alzheimer's disease, Pick's disease, progressive supranuclear palsy and corticobasal degeneration. Acta Neuropathol. *104*, 583-591.

Ferrer, I., Barrachina, M., Tolnay, M., Rey, M.J., Vidal, N., Carmona, M., Blanco, R., and Puig, B. (2003). Phosphorylated protein kinases associated with neuronal and glial tau deposits in argyrophilic grain disease. Brain Pathol. *13*, 62-78.

Fleming, T., Chien, S.-C., Vanderzalm, P.J., Dell, M., Gavin, M.K., Forrester, W.C., and Garriga, G. (2010). The role of C. elegans Ena/VASP homolog UNC-34 in neuronal polarity and motility. Dev. Biol. *344*, 94-106.

Funk, K.E., Thomas, S.N., Schafer, K.N., Cooper, G.L., Liao, Z., Clark, D.J., Yang, A.J., and Kuret, J. (2014). Lysine methylation is an endogenous post-translational modification of tau protein in human brain and a modulator of aggregation propensity. Biochem. J. *462*, 77-88.

Gerson, J.E., Sengupta, U., Lasagna-Reeves, C.A., Guerrero-Munoz, M.J., Troncoso, J., and Kayed, R. (2014). Characterization of tau oligomeric seeds in progressive supranuclear palsy. Acta neuropathologica communications *2*, 73.

Geyer, E.A., Burns, A., Lalonde, B.A., Ye, X., Piedra, F.-A., Huffaker, T.C., and Rice, L.M. (2015). A mutation uncouples the tubulin conformational and GTPase cycles, revealing allosteric control of microtubule dynamics. eLife *4*, e10113.

Gibbons, I.R., and Rowe, A.J. (1965). Dynein: A Protein with Adenosine Triphosphatase Activity from Cilia. Science *149*, 424-426.

Gibney, J., and Zheng, J.Q. (2003). Cytoskeletal dynamics underlying collateral membrane protrusions induced by neurotrophins in cultured Xenopus embryonic neurons. J. Neurobiol. *54*, 393-405.

Goedert, M., Jakes, R., and Vanmechelen, E. (1995). Monoclonal antibody AT8 recognises tau protein phosphorylated at both serine 202 and threonine 205. Neurosci. Lett. *189*, 167-169.

Golgi, C. (1906). The neuron doctrine - theory and facts. Nobel Lectures Physiology Or Medicine 1901-1921, 189-217.

Goode, B.L., Chau, M., Denis, P.E., and Feinstein, S.C. (2000). Structural and functional differences between 3-repeat and 4-repeat tau isoforms. Implications for normal tau function and the onset of neurodegenetative disease. J. Biol. Chem. *275*, 38182-38189.

Gu, J., Chen, F., Iqbal, K., Gong, C.X., Wang, X., and Liu, F. (2017). Transactive response DNA-binding protein 43 (TDP-43) regulates alternative splicing of tau exon 10: Implications for the pathogenesis of tauopathies. J. Biol. Chem. *292*, 10600-10612.

Halpain, S., and Dehmelt, L. (2006). The MAP1 family of microtubule-associated proteins. Genome Biol. *7*, 224.

Hanger, D.P., and Noble, W. (2011). Functional Implications of Glycogen Synthase Kinase-3-Mediated Tau Phosphorylation. Int. J. Alzheimers Dis. *2011*.

Hartman, M.A., and Spudich, J.A. (2012). The myosin superfamily at a glance. J. Cell Sci. *125*, 1627-1632.

Heins, S., Song, Y.H., Wille, H., Mandelkow, E., and Mandelkow, E.M. (1991). Effect of MAP2, MAP2c, and tau on kinesin-dependent microtubule motility. J. Cell Sci. Suppl. *14*, 121-124.

Hinrichs, M.H., Jalal, A., Brenner, B., Mandelkow, E., Kumar, S., and Scholz, T. (2012). Tau protein diffuses along the microtubule lattice. J. Biol. Chem. *287*, 38559-38568.

Hirokawa, N., Noda, Y., Tanaka, Y., and Niwa, S. (2009). Kinesin superfamily motor proteins and intracellular transport. Nat. Rev. Mol. Cell Biol. *10*, 682-696.

Hirokawa, N., Shiomura, Y., and Okabe, S. (1988). Tau proteins: the molecular structure and mode of binding on microtubules. J. Cell Biol. *107*, 1449-1459.

Hoeprich, G.J., Thompson, A.R., McVicker, D.P., Hancock, W.O., and Berger, C.L. (2014). Kinesin's neck-linker determines its ability to navigate obstacles on the microtubule surface. Biophys. J. *106*, 1691-1700.

Hutton, M., and Hardy, J. (1997). The Presenilins and Alzheimer's Disease. Hum. Mol. Genet. *6*, 1639-1646.

Hyman, A., Drechsel, D., Kellogg, D., Salser, S., Sawin, K., Steffen, P., Wordeman, L., and Mitchison, T. (1991). Preparation of modified tubulins. Methods Enzymol. *196*, 478-485.

Inomata, H., Nakamura, Y., Hayakawa, A., Takata, H., Suzuki, T., Miyazawa, K., and Kitamura, N. (2003). A scaffold protein JIP-1b enhances amyloid precursor protein phosphorylation by JNK and its association with kinesin light chain 1. J. Biol. Chem. *278*, 22946-22955.

Ishiguro, K., Shiratsuchi, A., Sato, S., Omori, A., Arioka, M., Kobayashi, S., Uchida, T., and Imahori, K. (1993). Glycogen synthase kinase 3 beta is identical to tau protein kinase I generating several epitopes of paired helical filaments. FEBS Lett. *325*, 167-172.

Ittner, L.M., Ke, Y.D., Delerue, F., Bi, M., Gladbach, A., van Eersel, J., Wolfing, H., Chieng, B.C., Christie, M.J., Napier, I.A., Eckert, A., Staufenbiel, M., Hardeman, E., and Gotz, J. (2010). Dendritic function of tau mediates amyloid-beta toxicity in Alzheimer's disease mouse models. Cell *142*, 387-397.

Janning, D., Igaev, M., Sundermann, F., Bruhmann, J., Beutel, O., Heinisch, J.J., Bakota, L., Piehler, J., Junge, W., and Brandt, R. (2014). Single-molecule tracking of tau reveals fast kiss-and-hop interaction with microtubules in living neurons. Mol. Biol. Cell *25*, 3541-3551.

Jeganathan, S., Hascher, A., Chinnathambi, S., Biernat, J., Mandelkow, E.M., and Mandelkow, E. (2008). Proline-directed pseudo-phosphorylation at AT8 and PHF1 epitopes induces a compaction of the paperclip folding of Tau and generates a pathological (MC-1) conformation. J. Biol. Chem. *283*, 32066-32076.

Jeganathan, S., von Bergen, M., Brutlach, H., Steinhoff, H.J., and Mandelkow, E. (2006). Global hairpin folding of tau in solution. Biochemistry *45*, 2283-2293.

Jin, N., Yin, X., Gu, J., Zhang, X., Shi, J., Qian, W., Ji, Y., Cao, M., Gu, X., Ding, F., Iqbal, K., Gong, C.X., and Liu, F. (2015). Truncation and Activation of Dual Specificity Tyrosine Phosphorylation-regulated Kinase 1A by Calpain I: A MOLECULAR MECHANISM LINKED TO TAU PATHOLOGY IN ALZHEIMER DISEASE. J. Biol. Chem. *290*, 15219-15237.

Johnson, I.D. (2010). The Molecular Probes Handbook: A Guide to Fluorescent Probes and Labeling Technologies, 11th Edition. Life Technologies Corporation.

Joo, C., and Ha, T. (2012a). Imaging and identifying impurities in single-molecule FRET studies. Cold Spring Harbor protocols *2012*, 1109-1112.

Joo, C., and Ha, T. (2012b). Preparing sample chambers for single-molecule FRET. Cold Spring Harbor protocols *2012*, 1104-1108.

Kadavath, H., Jaremko, M., Jaremko, L., Biernat, J., Mandelkow, E., and Zweckstetter, M. (2015). Folding of the Tau Protein on Microtubules. Angew. Chem. Int. Ed. Engl. *54*, 10347-10351.

Kalil, K., and Dent, E.W. (2014). Branch management: mechanisms of axon branching in the developing vertebrate CNS. Nature reviews. Neuroscience *15*, 7-18.

Kamah, A., Huvent, I., Cantrelle, F.X., Qi, H., Lippens, G., Landrieu, I., and Smet-Nocca, C. (2014). Nuclear magnetic resonance analysis of the acetylation pattern of the neuronal Tau protein. Biochemistry *53*, 3020-3032.

Kanaan, N.M., Morfini, G., Pigino, G., LaPointe, N.E., Andreadis, A., Song, Y., Leitman, E., Binder, L.I., and Brady, S.T. (2012). Phosphorylation in the amino terminus of tau prevents inhibition of anterograde axonal transport. Neurobiol. Aging *33*, 826 e815-830.

Kanaan, N.M., Morfini, G.A., LaPointe, N.E., Pigino, G.F., Patterson, K.R., Song, Y., Andreadis, A., Fu, Y., Brady, S.T., and Binder, L.I. (2011). Pathogenic forms of tau inhibit kinesin-dependent axonal transport through a mechanism involving activation of axonal phosphotransferases. J. Neurosci. *31*, 9858-9868.

Kanaan, N.M., Pigino, G.F., Brady, S.T., Lazarov, O., Binder, L.I., and Morfini, G.A. (2013). Axonal degeneration in Alzheimer's disease: when signaling abnormalities meet the axonal transport system. Exp. Neurol. *246*, 44-53.

Kapanidis, A.N., Laurence, T.A., Lee, N.K., Margeat, E., Kong, X., and Weiss, S. (2005). Alternating-laser excitation of single molecules. Acc. Chem. Res. *38*, 523-533.

Kaul, N., Soppina, V., and Verhey, Kristen J. (2014). Effects of α-Tubulin K40 Acetylation and Detyrosination on Kinesin-1 Motility in a Purified System. Biophys. J. *106*, 2636-2643.

Kellogg, E.H., Hejab, N.M., Poepsel, S., Downing, K.H., DiMaio, F., and Nogales, E. (2018). Atomic model of microtubule-bound tau, BioRxiv.

Kirouac, L., Rajic, A.J., Cribbs, D.H., and Padmanabhan, J. (2017). Activation of Ras-ERK Signaling and GSK-3 by Amyloid Precursor Protein and Amyloid Beta Facilitates Neurodegeneration in Alzheimer's Disease. eNeuro *4*.

Konishi, Y., and Setou, M. (2009). Tubulin tyrosination navigates the kinesin-1 motor domain to axons. Nat. Neurosci. *12*, 559-567.

Konzack, S., Thies, E., Marx, A., Mandelkow, E.M., and Mandelkow, E. (2007). Swimming against the tide: mobility of the microtubule-associated protein tau in neurons. J. Neurosci. *27*, 9916-9927.

Korn, E., Carlier, M., and Pantaloni, D. (1987). Actin polymerization and ATP hydrolysis. Science *238*, 638-644.

Kurbatskaya, K., Phillips, E.C., Croft, C.L., Dentoni, G., Hughes, M.M., Wade, M.A., Al-Sarraj, S., Troakes, C., O'Neill, M.J., Perez-Nievas, B.G., Hanger, D.P., and Noble, W. (2016). Upregulation of calpain activity precedes tau phosphorylation and loss of synaptic proteins in Alzheimer's disease brain. Acta neuropathologica communications *4*, 34.

LaPointe, N.E., Morfini, G., Pigino, G., Gaisina, I.N., Kozikowski, A.P., Binder, L.I., and Brady, S.T. (2009). The amino terminus of tau inhibits kinesin-dependent axonal transport: implications for filament toxicity. J. Neurosci. Res. *87*, 440-451.

Larson, M., Sherman, M.A., Amar, F., Nuvolone, M., Schneider, J.A., Bennett, D.A., Aguzzi, A., and Lesne, S.E. (2012). The complex PrP(c)-Fyn couples human oligomeric Abeta with pathological tau changes in Alzheimer's disease. J. Neurosci. *32*, 16857-16871a.

Leandro-Garcia, L.J., Leskela, S., Landa, I., Montero-Conde, C., Lopez-Jimenez, E., Leton, R., Cascon, A., Robledo, M., and Rodriguez-Antona, C. (2010). Tumoral and tissue-specific expression of the major human beta-tubulin isotypes. Cytoskeleton (Hoboken, N.J.) *67*, 214-223.

Lee, G., Newman, S.T., Gard, D.L., Band, H., and Panchamoorthy, G. (1998). Tau interacts with src-family non-receptor tyrosine kinases. J. Cell Sci. *111 (Pt 21)*, 3167-3177.

Lee, G., Thangavel, R., Sharma, V.M., Litersky, J.M., Bhaskar, K., Fang, S.M., Do, L.H., Andreadis, A., Van Hoesen, G., and Ksiezak-Reding, H. (2004). Phosphorylation of tau by fyn: implications for Alzheimer's disease. J. Neurosci. *24*, 2304-2312.

Lee, M.S., Kwon, Y.T., Li, M., Peng, J., Friedlander, R.M., and Tsai, L.H. (2000). Neurotoxicity induces cleavage of p35 to p25 by calpain. Nature *405*, 360-364.

Lee, T.J., Lee, J.W., Haynes, E.M., Eliceiri, K.W., and Halloran, M.C. (2017). The Kinesin Adaptor Calsyntenin-1 Organizes Microtubule Polarity and Regulates Dynamics during Sensory Axon Arbor Development. Front. Cell. Neurosci. *11*.

Lessard, D.V., and Berger, C.L. Novel Kinesin-3 Motor Behavior is Regulated by Tau. Biophys. J. *114*, 511a.

Levitan, I.B., and Kaczmarek, L.K. (2015). The Neuron: Cell and Molecular Biology. Oxford University Press.

Ling, C., Hendrickson, M.L., and Kalil, R.E. (2012). Resolving the detailed structure of cortical and thalamic neurons in the adult rat brain with refined biotinylated dextran amine labeling. PLoS One *7*, e45886.

Ling, H. (2018). Untangling the tauopathies: Current concepts of tau pathology and neurodegeneration. Parkinsonism Relat. Disord. *46 Suppl 1*, S34-s38.

Liu, S.-L., Wang, C., Jiang, T., Tan, L., Xing, A., and Yu, J.-T. (2016). The Role of Cdk5 in Alzheimer's Disease. Mol. Neurobiol. *53*, 4328-4342.

Liu, Y., Liu, F., Grundke-Iqbal, I., Iqbal, K., and Gong, C.-X. (2011). Deficient brain insulin signalling pathway in Alzheimer's disease and diabetes. The Journal of pathology *225*, 54-62.

Llorens-Martin, M., Jurado, J., Hernandez, F., and Avila, J. (2014). GSK-3beta, a pivotal kinase in Alzheimer disease. Front. Mol. Neurosci. *7*, 46.

Lovestone, S., Hartley, C.L., Pearce, J., and Anderton, B.H. (1996). Phosphorylation of tau by glycogen synthase kinase-3 beta in intact mammalian cells: the effects on the organization and stability of microtubules. Neuroscience *73*, 1145-1157.

Lowndes, M., and Nelson, W.J. (2013). Fabricating surfaces with distinct geometries and different combinations of cell adhesion proteins. Methods Mol. Biol. *1046*, 219-230.

Maday, S., Twelvetrees, A.E., Moughamian, A.J., and Holzbaur, E.L. (2014). Axonal transport: cargo-specific mechanisms of motility and regulation. Neuron *84*, 292-309.

Margeat, E., Kapanidis, A.N., Tinnefeld, P., Wang, Y., Mukhopadhyay, J., Ebright, R.H., and Weiss, S. (2006). Direct observation of abortive initiation and promoter escape within single immobilized transcription complexes. Biophys. J. *90*, 1419-1431.

Martin, L., Latypova, X., and Terro, F. (2011). Post-translational modifications of tau protein: Implications for Alzheimer's disease. Neurochem. Int. *58*, 458-471.

Martin, L., Latypova, X., Wilson, C.M., Magnaudeix, A., Perrin, M.-L., and Terro, F. (2013a). Tau protein phosphatases in Alzheimer's disease: The leading role of PP2A. Ageing Research Reviews *12*, 39-49.

Martin, L., Latypova, X., Wilson, C.M., Magnaudeix, A., Perrin, M.-L., Yardin, C., and Terro, F. (2013b). Tau protein kinases: Involvement in Alzheimer's disease. Ageing Research Reviews *12*, 289-309.

McKinney, S.A., Joo, C., and Ha, T. (2006). Analysis of Single-Molecule FRET Trajectories Using Hidden Markov Modeling. Biophys. J. *91*, 1941-1951.

McVicker, D.P., Chrin, L.R., and Berger, C.L. (2011). The nucleotide-binding state of microtubules modulates kinesin processivity and the ability of Tau to inhibit kinesin-mediated transport. J. Biol. Chem. *286*, 42873-42880.

McVicker, D.P., Hoeprich, G.J., Thompson, A.R., and Berger, C.L. (2014). Tau interconverts between diffusive and stable populations on the microtubule surface in an isoform and lattice specific manner. Cytoskeleton (Hoboken, N.J.) *71*, 184-194.

Monroy, B.Y., Sawyer, D.L., Ackermann, B.E., Borden, M.M., Tan, T.C., and Ori-McKenney, K.M. (2017). Competition between microtubule-associated proteins directs motor transport. bioRxiv.

Moore, S.W., Tessier-Lavigne, M., and Kennedy, T.E. (2007). Netrins and their receptors. Adv. Exp. Med. Biol. *621*, 17-31.

Morfini, G., Pigino, G., Mizuno, N., Kikkawa, M., and Brady, S.T. (2007). Tau binding to microtubules does not directly affect microtubule-based vesicle motility. J. Neurosci. Res. *85*, 2620-2630.

Morfini, G., Szebenyi, G., Elluru, R., Ratner, N., and Brady, S.T. (2002). Glycogen synthase kinase 3 phosphorylates kinesin light chains and negatively regulates kinesin-based motility. EMBO J. *21*, 281-293.

Mori, T., Wada, T., Suzuki, T., Kubota, Y., and Inagaki, N. (2007). Singar1, a novel RUN domain-containing protein, suppresses formation of surplus axons for neuronal polarity. J. Biol. Chem. *282*, 19884-19893.

Morris, M., Knudsen, G.M., Maeda, S., Trinidad, J.C., Ioanoviciu, A., Burlingame, A.L., and Mucke, L. (2015). Tau post-translational modifications in wild-type and human amyloid precursor protein transgenic mice. Nat. Neurosci. *18*, 1183-1189.

Moustafa, A.A., Hassan, M., Hewedi, D.H., Hewedi, I., Garami, J.K., Al Ashwal, H., Zaki, N., Seo, S.Y., Cutsuridis, V., Angulo, S.L., Natesh, J.Y., Herzallah, M.M., Frydecka, D., Misiak, B., Salama, M., Mohamed, W., El Haj, M., and Hornberger, M. (2018). Genetic underpinnings in Alzheimer's disease - a review. Rev. Neurosci. *29*, 21-38.

Multhaup, G., Huber, O., Buee, L., and Galas, M.C. (2015). Amyloid Precursor Protein (APP) Metabolites APP Intracellular Fragment (AICD), Abeta42, and Tau in Nuclear Roles. J. Biol. Chem. *290*, 23515-23522.

Murphy, D.B., Wallis, K.T., and Hiebsch, R.R. (1983). Identity and origin of the ATPase activity associated with neuronal microtubules. II. Identification of a 50,000-dalton polypeptide with ATPase activity similar to F-1 ATPase from mitochondria. J. Cell Biol. *96*, 1306-1315.

Panda, D., Samuel, J.C., Massie, M., Feinstein, S.C., and Wilson, L. (2003). Differential regulation of microtubule dynamics by three- and four-repeat tau: implications for the onset of neurodegenerative disease. Proc. Natl. Acad. Sci. U. S. A. *100*, 9548-9553.

Pasik, P., Pasik, P., Cajal, S.R., Pasik, T., and Pasik, T. (1999). Texture of the Nervous System of Man and the Vertebrates. Springer Vienna.

Perez, M., Santa-Maria, I., De Barreda, E.G., Zhu, X., Cuadros, R., Cabrero, J.R., Sanchez-Madrid, F., Dawson, H.N., Vitek, M.P., Perry, G., Smith, M.A., and Avila, J. (2009). Tau – an inhibitor of deacetylase HDAC6 function. J. Neurochem. *109*, 1756-1766.

Polleux, F., Giger, R.J., Ginty, D.D., Kolodkin, A.L., and Ghosh, A. (1998). Patterning of cortical efferent projections by semaphorin-neuropilin interactions. Science *282*, 1904-1906.

Polleux, F., and Snider, W. (2010). Initiating and growing an axon. Cold Spring Harb. Perspect. Biol. *2*, a001925.

Previs, M.J., Beck Previs, S., Gulick, J., Robbins, J., and Warshaw, D.M. (2012). Molecular mechanics of cardiac myosin-binding protein C in native thick filaments. Science *337*, 1215-1218.

Previs, M.J., Prosser, B.L., Mun, J.Y., Previs, S.B., Gulick, J., Lee, K., Robbins, J., Craig, R., Lederer, W.J., and Warshaw, D.M. (2015). Myosin-binding protein C corrects an intrinsic inhomogeneity in cardiac excitation-contraction coupling. Sci Adv *1*.

Prior, R., Van Helleputte, L., Benoy, V., and Van Den Bosch, L. (2017). Defective axonal transport: A common pathological mechanism in inherited and acquired peripheral neuropathies. Neurobiol. Dis. *105*, 300-320.

Qian, W., Jin, N., Shi, J., Yin, X., Jin, X., Wang, S., Cao, M., Iqbal, K., Gong, C.X., and Liu, F. (2013). Dual-specificity tyrosine phosphorylation-regulated kinase 1A (Dyrk1A) enhances tau expression. J. Alzheimers Dis. *37*, 529-538.

Ramón y Cajal, S. (1906). The structure and connexions of neurons. Nobel Lectures Physiology Or Medicine 1901-1921, 220-253.

Romaniello, R., Arrigoni, F., Bassi, M.T., and Borgatti, R. (2015). Mutations in α- and β-tubulin encoding genes: Implications in brain malformations. Brain Dev. *37*, 273-280.

Rosenberg, K.J., Ross, J.L., Feinstein, H.E., Feinstein, S.C., and Israelachvili, J. (2008). Complementary dimerization of microtubule-associated tau protein: Implications for microtubule bundling and tau-mediated pathogenesis. Proc. Natl. Acad. Sci. U. S. A. *105*, 7445-7450.

Roy, R., Hohng, S., and Ha, T. (2008). A practical guide to single-molecule FRET. Nature methods *5*, 507-516.

Santarella, R.A., Skiniotis, G., Goldie, K.N., Tittmann, P., Gross, H., Mandelkow, E.M., Mandelkow, E., and Hoenger, A. (2004). Surface-decoration of microtubules by human tau. J. Mol. Biol. *339*, 539-553.

Santoso, Y., Torella, J.P., and Kapanidis, A.N. (2010). Characterizing Single-Molecule FRET Dynamics with Probability Distribution Analysis. Chemphyschem *11*, 2209-2219.

Schindelin, J., Arganda-Carreras, I., Frise, E., Kaynig, V., Longair, M., Pietzsch, T., Preibisch, S., Rueden, C., Saalfeld, S., Schmid, B., Tinevez, J.Y., White, D.J., Hartenstein, V., Eliceiri, K., Tomancak, P., and Cardona, A. (2012). Fiji: an open-source platform for biological-image analysis. Nature methods *9*, 676-682.

Seitz, A., Kojima, H., Oiwa, K., Mandelkow, E.-M., Song, Y.-H., and Mandelkow, E. (2002). Single-molecule investigation of the interference between kinesin, tau and MAP2c. The EMBO Journal *21*, 4896-4905.

Shelly, M., Cancedda, L., Heilshorn, S., Sumbre, G., and Poo, M.M. (2007). LKB1/STRAD promotes axon initiation during neuronal polarization. Cell *129*, 565-577.

Shrestha, D., Jenei, A., Nagy, P., Vereb, G., and Szöllősi, J. (2015). Understanding FRET as a Research Tool for Cellular Studies. Int. J. Mol. Sci. *16*, 6718-6756.

Song, Y., and Brady, S.T. (2013). Analysis of microtubules in isolated axoplasm from the squid giant axon. Methods Cell Biol. *115*, 125-137.

Stenoien, D.L., and Brady, S.T. (1999). Discovery and Conceptual Development of Fast and Slow Axonal Transport. In: Basic Neurochemistry: Molecular, Cellular and Medical Aspects, eds. G.J. Siegel, B.W. Agranoff, R.W. Albers, and e. al., Philadelphia: Lippincott-Raven.

Stern, J.L., Lessard, D.V., Hoeprich, G.J., Morfini, G.A., and Berger, C.L. (2017). Phospho-regulation of tau modulates inhibition of kinesin-1 motility. Mol. Biol. Cell.

Stiles, J., and Jernigan, T.L. (2010). The Basics of Brain Development. Neuropsychol. Rev. *20*, 327-348.

Sultan, A., Nesslany, F., Violet, M., Begard, S., Loyens, A., Talahari, S., Mansuroglu, Z., Marzin, D., Sergeant, N., Humez, S., Colin, M., Bonnefoy, E., Buee, L., and Galas, M.C. (2011). Nuclear tau, a key player in neuronal DNA protection. J. Biol. Chem. *286*, 4566-4575.

Sun, L., Zhou, R., Yang, G., and Shi, Y. (2017). Analysis of 138 pathogenic mutations in presenilin-1 on the in vitro production of Aβ42 and Aβ40 peptides by γ-secretase. Proceedings of the National Academy of Sciences *114*, E476-E485.

Thompson, A.R., Hoeprich, G.J., and Berger, C.L. (2013). Single-molecule motility: statistical analysis and the effects of track length on quantification of processive motion. Biophys. J. *104*, 2651-2661.

Toda, H., Mochizuki, H., Flores, R., 3rd, Josowitz, R., Krasieva, T.B., Lamorte, V.J., Suzuki, E., Gindhart, J.G., Furukubo-Tokunaga, K., and Tomoda, T. (2008). UNC-51/ATG1 kinase regulates axonal transport by mediating motor-cargo assembly. Genes Dev. *22*, 3292-3307.

Toriyama, M., Shimada, T., Kim, K.B., Mitsuba, M., Nomura, E., Katsuta, K., Sakumura, Y., Roepstorff, P., and Inagaki, N. (2006). Shootin1: A protein involved in the organization of an asymmetric signal for neuronal polarization. J. Cell Biol. *175*, 147-157.

Trinczek, B., Ebneth, A., Mandelkow, E.M., and Mandelkow, E. (1999). Tau regulates the attachment/detachment but not the speed of motors in microtubule-dependent transport of single vesicles and organelles. J. Cell Sci. *112 (Pt 14)*, 2355-2367.

Tucker, R.P., Binder, L.I., Viereck, C., Hemmings, B.A., and Matus, A.I. (1988). The sequential appearance of low- and high-molecular-weight forms of MAP2 in the developing cerebellum. The Journal of Neuroscience *8*, 4503.

Vacaresse, N., Moller, B., Danielsen, E.M., Okada, M., and Sap, J. (2008). Activation of c-Src and Fyn kinases by protein-tyrosine phosphatase RPTPalpha is substrate-specific and compatible with lipid raft localization. J. Biol. Chem. *283*, 35815-35824.

Vagnoni, A., Rodriguez, L., Manser, C., De Vos, K.J., and Miller, C.C.J. (2011). Phosphorylation of kinesin light chain 1 at serine 460 modulates binding and trafficking of calsyntenin-1. J. Cell Sci. *124*, 1032.

Vale, R.D. (2003). The Molecular Motor Toolbox for Intracellular Transport. Cell *112*, 467-480.

Vale, R.D., Reese, T.S., and Sheetz, M.P. (1985). Identification of a novel force-generating protein, kinesin, involved in microtubule-based motility. Cell *42*, 39-50.

van de Willige, D., Hoogenraad, C.C., and Akhmanova, A. (2016). Microtubule plus-end tracking proteins in neuronal development. Cell. Mol. Life Sci. *73*, 2053-2077.

Verhey, K.J., and Hammond, J.W. (2009). Traffic control: regulation of kinesin motors. Nat. Rev. Mol. Cell Biol. *10*, 765-777.

Vershinin, M., Carter, B.C., Razafsky, D.S., King, S.J., and Gross, S.P. (2007). Multiple-motor based transport and its regulation by Tau. Proc. Natl. Acad. Sci. U. S. A. *104*, 87-92.

von Massow, A., Mandelkow, E.M., and Mandelkow, E. (1989). Interaction between kinesin, microtubules, and microtubule-associated protein 2. Cell Motil. Cytoskeleton *14*, 562-571.

Wada, Y., Ishiguro, K., Itoh, T.J., Uchida, T., Hotani, H., Saito, T., Kishimoto, T., and Hisanaga, S. (1998). Microtubule-stimulated phosphorylation of tau at Ser202 and Thr205 by cdk5 decreases its microtubule nucleation activity. J. Biochem. *124*, 738-746.

Wang, X., and Schwarz, T.L. (2009). The mechanism of Ca2+ -dependent regulation of kinesin-mediated mitochondrial motility. Cell *136*, 163-174.

Watanabe, A., Hasegawa, M., Suzuki, M., Takio, K., Morishima-Kawashima, M., Titani, K., Arai, T., Kosik, K.S., and Ihara, Y. (1993). In vivo phosphorylation sites in fetal and adult rat tau. J. Biol. Chem. *268*, 25712-25717.

Weingarten, M.D., Lockwood, A.H., Hwo, S.Y., and Kirschner, M.W. (1975). A protein factor essential for microtubule assembly. Proc. Natl. Acad. Sci. U. S. A. *72*, 1858-1862.

Weiss, P., and Hiscoe, H.B. (1948). Experiments on the mechanism of nerve growth. J. Exp. Zool. *107*, 315-395.

Wilson, L., Stewart, W., Dams-O'Connor, K., Diaz-Arrastia, R., Horton, L., Menon, D.K., and Polinder, S. (2017). The chronic and evolving neurological consequences of traumatic brain injury. The Lancet Neurology *16*, 813-825.

Wodarz, A., and Huttner, W.B. (2003). Asymmetric cell division during neurogenesis in Drosophila and vertebrates. Mech. Dev. *120*, 1297-1309.

Yen, S.-H., Hutton, M., DeTure, M., Ko, L.-W., and Nacharaju, P. (1999). Fibrillogenesis of Tau: Insights from Tau Missense Mutations in FTDP-17. Brain Pathol. *9*, 695-705.

Yin, X., Jin, N., Gu, J., Shi, J., Zhou, J., Gong, C.-X., Iqbal, K., Grundke-Iqbal, I., and Liu, F. (2012). Dual-specificity Tyrosine Phosphorylation-regulated Kinase 1A (Dyrk1A) Modulates Serine/Arginine-rich Protein 55 (SRp55)-promoted Tau Exon 10 Inclusion. The Journal of Biological Chemistry *287*, 30497-30506.

Yin, X., Jin, N., Shi, J., Zhang, Y., Wu, Y., Gong, C.X., Iqbal, K., and Liu, F. (2017). Dyrk1A overexpression leads to increase of 3R-tau expression and cognitive deficits in Ts65Dn Down syndrome mice. Sci. Rep. *7*, 619.

Yu, I., Garnham, C.P., and Roll-Mecak, A. (2015). Writing and Reading the Tubulin Code. J. Biol. Chem. *290*, 17163-17172.

Zhong, J. (2016). RAS and downstream RAF-MEK and PI3K-AKT signaling in neuronal development, function and dysfunction. Biol. Chem. *397*, 215-222.